Spring 2014

Characterization of an Impulse Radiating Antenna in the Near Field

Chandra Barjracharya
Old Dominion University

CHARACTERIZATION OF AN IMPULSE RADIATING ANTENNA IN THE

NEAR FIELD

by

Chandra Bajracharya
B. E. December 2002, Tribhuvan University, Nepal
M. S. June 2008, Norwegian University of Science and Technology, Norway
M. S. August 2013, Eastern Kentucky University

A Dissertation Submitted to the Faculty of
Old Dominion University in Partial Fulfillment of the
Requirements for the Degree of

DOCTOR OF PHILOSOPHY

ELECTRICAL AND COMPUTER ENGINEERING

OLD DOMINION UNIVERSITY
May 2014

Approved by:

—————————————————
Shu Xiao (Director)

—————————————————
Shirshak K. Dhali (Member)

—————————————————
Linda Vahala (Member)

—————————————————
Gene Hou (Member)

ABSTRACT

CHARACTERIZATION OF AN IMPULSE RADIATING ANTENNA IN THE NEAR FIELD

Chandra Bajracharya
Old Dominion University, 2014
Director: Dr. Shu Xiao

The biological effects of intense sub-nanosecond pulses on tissues or cells are in the dielectric domain and not based on thermal loading as in the conventional microwave radiation, which may lead to an entirely new approach of modifying cell functions. Moreover, the resulting cell functional change may be detected with higher resolution by broadband, sub-nanosecond pulses than conventional narrowband systems. The delivery of intense sub-nanosecond pulses to near-field biological tissues, however, has not been studied, not mentioning the focal depth and volume. In this dissertation, for the first time, an impulse radiating antenna with a balanced feed structure is studied for focusing electromagnetic fields in the near-field for the purpose of therapy and target detection. This antenna has the potential of radiating sub-nanosecond pulses up to 100 kV. It is a travelling wave antenna with the conical transmission lines as the wave launcher. The electric field distribution is studied both through experiment and simulation studies. Results show a close agreement between experimental and simulated results. The antenna focal spot is found to be 32cm wide in axial direction and 10cm wide in lateral direction near the focal point, which is 16cm from the aperture plane. Enhancement of focal spot size and increase of field at the focal point is studied with a dielectric lens. The use of a dielectric lens to match the waves to the target medium increases coupling between the antenna and the target medium, thereby increasing the field strength at focus and decreasing the focal spot size. Experimental study shows an increase in electric field at focus by a factor of 3 and an increase in resolution by a factor of 1.5. The delivery of sub-nanosecond pulses to tissues is studied with the antenna and the combination of the lens and antenna. While a lossless lens may enhance the coupling of the radiation to the tissue, the

trend of decreasing in intensity as the wave penetrates remains the same as the case where only an antenna is used. However, the trend can be reversed or modified by a lossy lens, which contains some resistive materials as part of its structure. With a lossy lens, a local maximum forms in the deep region (6cm in depth) of the tissue. The design of such lossy lens is novel and provides an extra means to control the electric field distribution in the target.

This dissertation is dedicated to my lovely daughter, Sneha.

ACKNOWLEDGEMENTS

First and foremost, I would like to express my deepest gratitude to my advisor, Dr. Shu Xiao, for providing me with invaluable guidance and encouragement throughout my graduate studies. I am grateful to Dr. Xiao for his confidence in my work, and for continuously motivating and supporting me during tough times to finish the thesis. His patience and encouragement have played a fundamental role in the completion of this doctoral work. For that, I am deeply indebted to Dr. Xiao.

I would also like to thank Dr. Shirshak Dhali, Dr. Linda Vahala and Dr. Gene Hou for their support, interest and time serving on the dissertation committee. I am thankful for their helpful comments and valuable feedback.

I gratefully acknowledge the funding sources that made my doctoral dissertation possible. I am also grateful to Dr. Ocsar Gonzalez, Graduate Program Director of the Electrical and Computer Engineering Department, for his advice and support. I would also like to thank my fellow graduate students, Mark Migliaccio and Thomas Camp, for their help.

Lastly, I would like to thank my family for all their unconditional love and support. For my mother, my husband and my daughter who have been a constant source of inspiration and encouragement, thank you!

TABLE OF CONTENTS

LIST OF TABLES

.

LIST OF FIGURES

CHAPTER I

INTRODUCTION

The subject of ultra-short electromagnetic pulses and their interaction with matter is attracting increasing interest due to their potential use in Electromagnetic Pulse (EMP) weapons, remote sensing, and biological applications, etc. The effect of electromagnetic radiation on biological media has been of great interest in the past century. Studies of electromagnetic field interactions with biological systems are broadly focused in two categories: therapeutic applications based on thermal effects like diathermy and hyperthermia cancer treatment, and informational applications like diagnostic imaging. Both therapeutic and diagnostic applications require deep penetration of electromagnetic power into high water content biological tissue.

In order to radiate a short pulse, the antenna must be capable of radiating over a broad bandwidth. Impulse-radiating antennas (IRAs) are a type of antenna used to transmit and receive short pulses. The IRA is an equi-phase aperture that is fed by a spherical transverse electromagnetic (TEM) wave. The focusing IRA was introduced by C. E. Baum and a closed-form time-domain model for predicting near field focusing characteristics of the IRA was developed [1]. Due to this focusing capability, there has been great interest in applying the IRA to the near-field applications like sensing, imaging and focusing electromagnetic fields into biological targets.

Focusing electromagnetic waves primarily aims at increasing the power deposited at a deep target. However, biological tissues, including muscle, fat, blood, or others have relatively high dielectric constant and conductivity. They absorb power and attenuate the waves in an exponentially decaying manner, preventing deep wave penetration. Hence, delivering electromagnetic energy to deep seated targets (e.g., tumors) is a difficult problem and a large amount of research has been devoted to the development of an external deep-tissue focusing

system. An ideal focusing system should be capable of focusing the radiation to a minimum spot size restricted by the diffraction limit. In diagnostic applications, a small spot size means a good spatial resolution. Whereas for therapeutic applications, a small spot size ensures that only the targeted tissue will be treated and the surrounding normal tissues will be spared. The effectiveness of a focusing system depends on the frequency of operation and the angular distribution of the power incidence. It requires careful selection of frequency which allows the balancing of desired spatial resolution with required penetration depth [2]. Hence, the application of electromagnetic radiation in radiofrequency and microwave range with an antenna or applicator has been studied extensively with various target accesses.

I.I ELECTROMAGNETIC RADIATION IN BIOLOGICAL MEDIA

Most of the early studies of electromagnetic wave delivery to biological media were focused on single narrowband antennas having no ability to focus energy. The types of antennas included waveguide and horn antennas [3-9], microstrip antennas [10-13] and coaxial TEM antennas [14-16]. The fundamental problem of planar layers of tissues (fat and muscle) exposed to plane waves was theoretically treated in early studies by Schwan [17]. In his paper, Schwan pointed out that the discontinuity at the fat-muscle interface sets up a severe standing wave in the fat region and calculated the relative heat development in fat-muscle layers due to an incident plane wave as a function of frequency. Schwan's results were experimentally verified in [18-19]. The EM energy was delivered to biological targets using antennas placed on their surfaces with a contacting medium (bolus), and the studies indicated the desirability of using low frequencies for a deeper penetration. However, as frequency was reduced, it was observed that it became more difficult to direct a plane wave field to a localized area. Different researchers have proposed different design improvements on the waveguide and horn antennas [3-9] to increase the depth of penetration, reduce the standing wave ratio, and produce a uniform heating of tissues. When using waveguide and horn antennas, in some cases, their dimensions made treatment of small

cross sections and curved surfaces difficult, especially at lower frequencies. In these circumstances, microstrip antennas offer the advantages of being small, lightweight and inexpensive alternatives [10-13]. In general, waveguide and horn antennas as well as microstrip antennas were able to deliver electromagnetic energy to the biological targets but the penetration depth was limited to only few centimeters (~3 to 4cm) from the surface of the target. In an effort to deliver electromagnetic energy deep into tissues, a coaxial TEM applicator was studied by researchers from Utrecht, Netherlands [14]. The coaxial TEM system produces a circumferential electrical field around the biological target. Similar calculations and experiments were carried out [15-16] and confirmed that central heating could be achieved with the TEM coupling technique. However, there was no ability to steer or control the energy. High power narrowband reflector antennas have also been studied for focusing electromagnetic radiation in the near field [20-23]. Ellipsoidal reflectors possess the geometrical property of focusing every ray originating from one focus to the other, and this property was utilized in focusing high frequency signals to biological targets through dielectric matching materials.

Studies on single narrowband antennas for delivering electromagnetic energy to biological tissues point out several important conclusions. Firstly, because of the impedance mismatch between two media, a large reflection occurs at air-tissue interface as well as the interfaces between different layers of tissue, setting up a severe standing wave and resulting in hot-spots. Hence, it is important to match the impedances to reduce reflections. Secondly, power is deposited more superficially at higher frequencies, whereas lower frequencies provide deeper penetration. As frequency is reduced, it becomes more difficult to direct a plane wave field to a localized area. So lower frequencies penetrate well but affect large regions of the body. Third, antenna elements that produce strong components of electric field perpendicular to tissue surface result in large hot-spots due to preferential heating at the fat-muscle interfaces [24]. So an incident electric field polarized in tissue plane penetrates more easily. Fourth, a plane wave

approximation cannot be used to predict spatial distribution of the field intensity in the tissue as it differs for different frequencies. Fifth, the permittivity seems to be more important than the conductivity in determining the field magnitude in the tissue [25-26]. Finally, the antennas have to operate in the near-field region so that focusing at the target can be used to increase the field strengths.

Since single antennas are insufficient in delivering high power and have little ability of focusing or steering energy, most of the recent research has been devoted to multi-element antenna arrays [27-36]. The use of a multi-element antenna array not only facilitates the treatment of large surface area involving complex body contours [27-29], but also offers the opportunity for transmitting signals that constructively interfere at a desired focal point [30-36]. Constructive interference is obtained with narrowband (single-frequency) focusing methods by adjusting the amplitude and phase of a sinusoidal signal in each antenna channel to compensate for the expected radial spreading and time delay incurred when the signal propagates from the antenna to the target focal point. The synchronization of antennas become critical in the coherent delivery. Major challenges still lie in the strong attenuation in the tissue. As a result, high power antennas are preferable. Additional information of tissue structures and electric properties will be instrumental for the success of the approach.

Meanwhile, it was pointed out that the multi-frequency technology offers some unique advantages like an enhanced capability to penetrate through obstacles and ultra-high precision ranging at the centimeter level, which are desirable for medical applications [37]. From a frequency-domain perspective, the main lobe for each frequency component of the transmitted ultra-wideband pulses attains a maximum at the focal location. Therefore, the total power at the focal location is the coherent summation of power across frequency, and hence it was considered that multi-frequency ultra-wideband focusing methods offer the potential for tighter focusing compared to narrowband methods [38]. Moreover, the formation of hot spots is highly frequency

dependent. So the use of a broadband multi-frequency system not only implies a potential for tighter focusing but also a greater reduction of hot-spots compared to narrowband methods.

I.II FOCUSING ELECTROMAGNETIC RADIATION USING UWB SYSTEMS

An Ultra-wideband (UWB) system refers to a system that is able to transfer multiple discrete frequencies or continuous broad-range frequencies. When represented in the time domain, in contrast to the narrowband sinusoidal waveforms of single frequency, an UWB system is associated with short duration pulses with fast rise or fall time in the order of nanoseconds and picoseconds.

Because portability and compactness are desired features of antennas to be used in medical applications, current research in UWB antennas for medical applications is primarily focused on small directional antennas. Focusing of ultra-wideband pulsed signals has been studied using beamforming techniques [39-48] and time reversal [49-53] techniques.

Analogous to the narrowband method, the UWB beamforming approach also uses a frequency dependent amplitude and phase adjustments in each channel. However, a UWB approach further exploits incoherent combining of power across frequency and space. UWB focusing may also be more robust to variability in tissue properties since the optimum frequency for focusing narrowband signals is dependent on the dielectric properties of the tissue. Early beamforming systems used simple delay and sum beamformers to spatially focus the signals, which has been studied for imaging of breast tumors [39-40]. However, this approach did not have the capacity to compensate for frequency dependent propagation effects and could not optimally discriminate against artifacts and noise.

$r_1[n]$

| Time Delay $n_1(\mathbf{r}_0)$ | Window 1 $g[n]$ | FIR $\mathbf{w}_1(\mathbf{r}_0)$ |

$r_2[n]$

| Time Delay $n_2(\mathbf{r}_0)$ | Window 1 $g[n]$ | FIR $\mathbf{w}_2(\mathbf{r}_0)$ |

$r_N[n]$

| Time Delay $n_N(\mathbf{r}_0)$ | Window 1 $g[n]$ | FIR $\mathbf{w}_N(\mathbf{r}_0)$ |

$z[n]$

| Window 2 $h[\mathbf{r}_0, n]$ |

| Energy Calc. | $p(\mathbf{r}_0)$
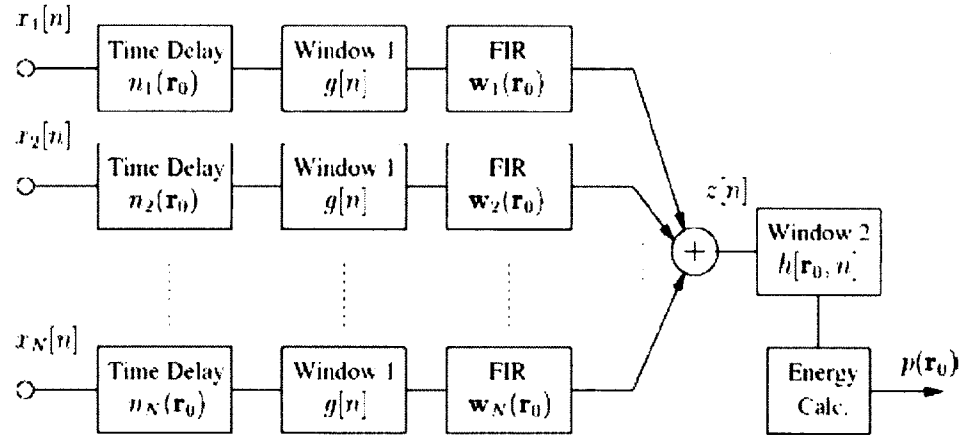
Fig. 1.1 Block diagram illustrating the MIST beamforming process for location r_0 in the breast: the beamformer passes components of backscattered signals originating from scan location r_0 with unit gain while attenuating signals from other locations. © 2003, IEEE. Reprinted, with permission, from [41].

The microwave imaging via space-time (MIST) beamforming [41] uses filters that compensate for dispersion and other limitations of the simple delay and sum algorithm. The MIST beamformer can be designed in the time domain, but frequency domain design is more computationally tractable, as it eliminates the need for large matrix inversions [42]. Based on the 2-D design [41-42], the experiments of 3-D MIST beamforming in multilayer breast phantoms was performed in [43]. Moreover, the feasibility of implementing the receiving beamformer of space–time microwave imaging [41-42] as transmitting beamformer was also studied in a noninvasive microwave hyperthermia treatment of breast cancer [44]. Many other image reconstruction algorithms have been proposed to modify the simple delay and sum beamforming technique. Delay, multiply and sum beamforming [46] improved delay and sum beamformer [47] and the filtered delay and sum beamformer [48] are some of the latest research.

In the time reversal method, the focusing is accomplished using a time reversal mirror (TRM) which is an array of transmit-receive transducers [49]. A source first sends a short pulse that propagates through the inhomogeneous medium from the array to the target. The target generates a backscattered signal that propagates through an inhomogeneous medium and is

distorted. This signal is recorded by the transducer array and is used to generate a time reversed field, which, when transmitted back by the TRM, focuses on the target.

(a)

(b)

(c)
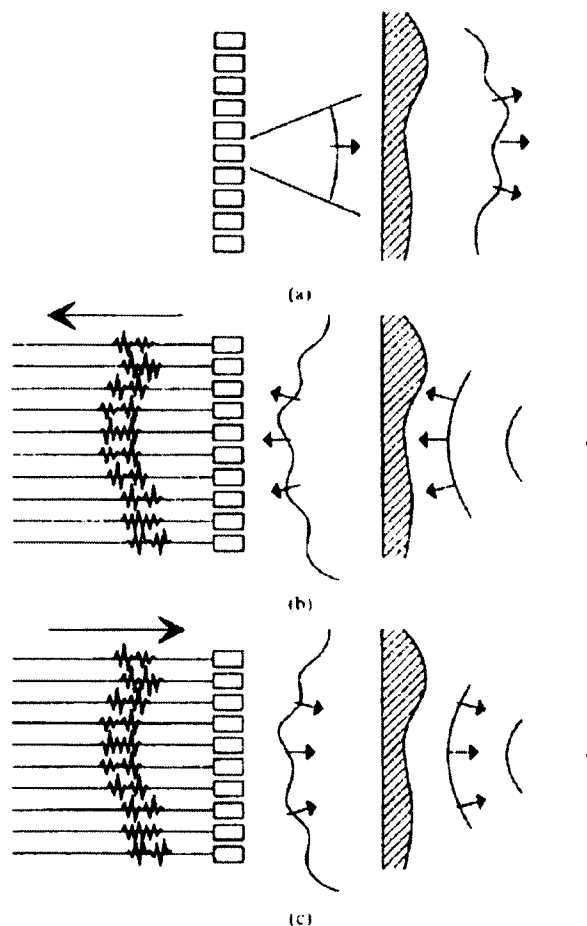
Fig.1.2. Basic process of TRM focusing: (a) transmitting, (b) recording, and (c) time reversing. © 1992, IEEE. Reprinted, with permission, from [49].

The time reversal technique has been studied for microwave breast cancer detection [50] and microwave hyperthermia treatment of breast cancer [51]. The two-dimensional numerical simulation [51] showed that a time reversal based ultra-wideband (UWB) microwave method for hyperthermia treatment has better electromagnetic energy focusing ability than the existing methods, and can provide the necessary temperature gradients required for effective hyperthermia. A time-reversal focusing method was also studied for the hyperthermia treatment

of head and neck tumors [52]. A wideband multi-channel amplifier system for time reversal microwave hyperthermia, operating in the frequency range 300MHz - 1GHz, was designed and developed in [53].

Both these techniques use a number of spatially separated antennas to transmit low-power ultra-wideband pulses into the biological target and to focus the electromagnetic radiation. Some of the UWB antenna designs used in these applications are presented in the following section.

I.III UWB ANTENNAS

The basic feature of UWB systems is that they occupy a wide operating bandwidth due to their use of impulse signals. UWB antennas should be effective in transmitting, free of dispersion, and have a good wide impedance bandwidth properties. There are a wide variety of UWB antenna designs available, but they can be categorized into two types. One integrates travelling wave structures in the radiating section and the other contains resonant structures for multiple frequencies. Some of the important classes of UWB antennas are discussed in the following subsections.

I.III.I Typical Broadband Antennas: Horn Antennas

A horn antenna is a TEM transmission line, tapered and truncated in such a way that allows it to convert guided electromagnetic energy into radiation and vice versa [54]. By choosing the flare angle of the tapering, it is possible to select the dominant mode that will propagate towards the aperture of the antenna [55]. Horn antennas tend to be relatively large and are directional with relatively high gains.

One of the applications of UWB horn antennas was in the treatment and detection of breast cancer. The group at the University of Wisconsin Madison proposed a UWB space-time beamforming technique employing an array of antennas, intended for medical imaging [41, 45] as well as for hyperthermia treatment [38, 44] of breast cancers. The UWB antenna designed for this

purpose was a miniaturized pyramidal horn with a single ridge and curved launching plane terminated with chip resistors [45]. The height of the pyramidal horn is 13mm and its aperture size is 25mm × 20mm. The antenna showed a VSWR less than 1.5 over the operating bandwidth of 1 - 11GHz.
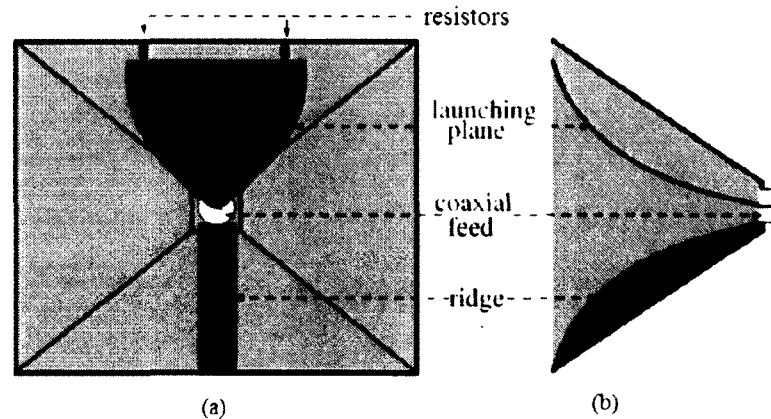
Fig. 1.3. The (a) end view and (b) side view of modified pyramid UWB horn antenna. © 2003, IEEE. Reprinted, with permission, from [45].

Another design of UWB TEM horn antenna was proposed by the research team at McMaster University [56] for microwave imaging of the breast. The TEM horn used a linearly tapered structure, fed by a coaxial line. A balun was placed between the coaxial line and TEM horn to remove the common mode radiation.

I.III.II Typical Broadband Antennas: Microstrip Antennas

Microstrip UWB antennas are usually constructed using printed circuit techniques, where a radiator of certain shape is etched onto dielectric substrate of a piece of the PCB and a partial ground plane onto the opposite side [57]. The radiation is generated around the edge of the conducting sheet, and is orthogonal to the conducting surface of the antenna. Taking into account the resonant frequency, directivity and antenna gain, microstrip UWB antennas with different types of patches like circular, elliptical, triangular, hexagonal etc. are currently being considered for UWB applications.

A compact patch antenna of the shape of an isosceles triangle was designed to be used for a 12-antenna array system for time reversal hyperthermia treatment [52]. A group of researchers at University of Queensland proposed using tapered slot UWB antenna of the compact size of 50mm × 50mm for imaging breast cancer, operating over a bandwidth 2.75 - 11GHz. The design was modified at the Queen Mary University of London with rounded arms, as shown in Fig. 1.4. The antenna was designed with the same size, but it resulted in wider bandwidth spanning 3.3 - 10.7 GHz [58]. Another type of UWB antenna, known as stacked-patch antenna was investigated by researchers at University of Bristol [59]. It had a microstrip line feed through a slot in the ground plane. The antenna had an operating bandwidth of 4 - 9.5GHz.
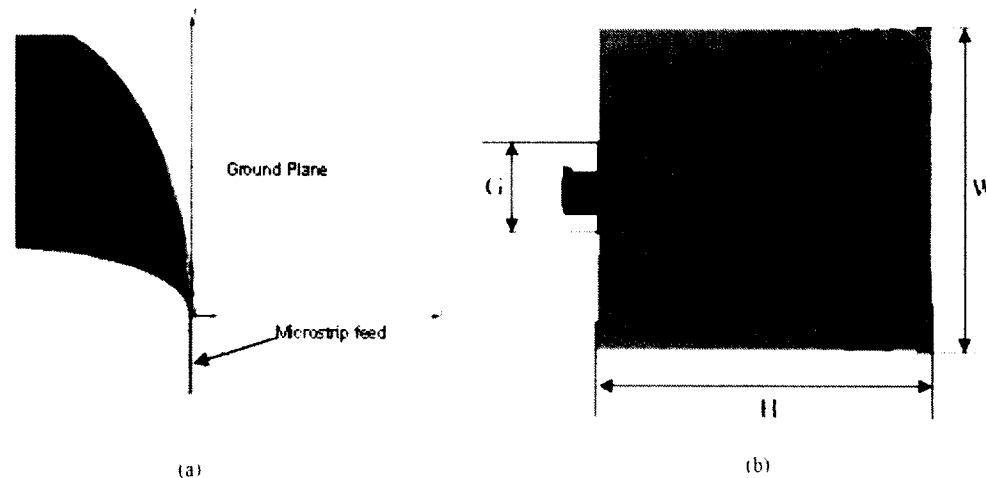
Fig. 1.4. Configurations of the (a) tapered slot antenna and (b) modified Vivaldi antenna. © 2008, IEEE. Reprinted, with permission, from [58].

I.III.III Typical Broadband Antennas: Impulse Radiating Antennas (IRA)

Another class of antennas suitable for UWB antennas are the reflector type impulse radiating antennas (IRA) [60]. IRAs are parabolic dish reflector antennas fed by travelling wave feed arms. These antennas exhibit high gain with an excellent impulse-like time domain response. Much work has been carried out on the fundamental design of this type of antenna by C. E. Baum

and E. G. Farr [61-64]. Various IRA designs have found applications such as target identification, detection of buried objects, landmines, and non-lethal weapons [65-66].

Fig. 1.5 shows a typical IRA with a parabolic reflector fed by a conical TEM wave launcher. Such a launcher supports a step-like TEM wave on the conical conductors leading from the apex to the edge of reflector. The feed arms of the antenna are a self-reciprocating structure that simplifies the calculation of the electromagnetic fields [64]. Launching as a fast-rising (step-like) TEM wave on the conical wave guide, the wave is reflected and approximately time differentiated for large distances in the focal direction [67]. A resistive termination is used at the reflector to minimize multiple reflections. For step function excitation, such an antenna gives a response as an impulse broadened by the aperture dimensions [60]. The resulting far-field strength is proportional to the time derivative of the pulse [68]. IRAs approximate constant aperture antennas, so their gain increases with frequency. Hence such antennas can deliver high-power electric fields when an ultra-high pulsed power source is used.
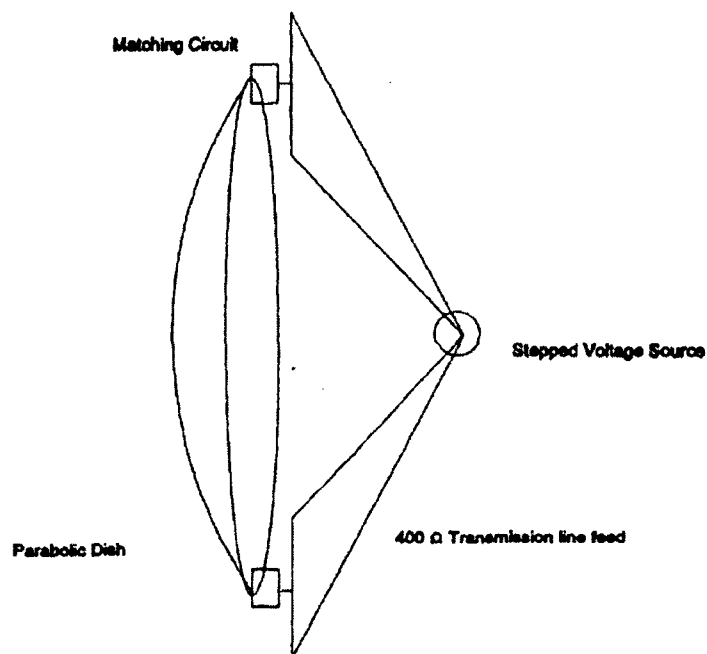
Fig. 1.5. Generic construction of the Impulse Radiating Antenna. Reprinted, with permission, from [62].

I.IV MOTIVATION

There has recently been a large interest in using ultra-wideband electromagnetic pulses for applications including medical diagnostics and imaging. Apart from that, studies on the effect of high power sub-nanosecond pulses on biological cells show that large electric fields, in combination with heating, can affect biological systems, either directly or indirectly [69-71]. It was pointed out [71] that pulses in sub-nanosecond range can be delivered by wideband antennas into tissues, and its electrical size is in the centimeter range. The spatial resolution can therefore be expected in the same range. Moreover, if the field is sufficiently large, it can cause tumor shrinkage or even complete elimination of melanoma tumors.

As discussed in previous section, many different UWB antenna designs have been proposed to deliver electromagnetic energy to biological targets. Each has its own merits and drawbacks. Most of the antennas have low-gain and/or low-radiation efficiency, and much of the current research is focused on using low power small antennas in an array. Although the performance of an antenna array increases with the number of antenna elements in the array, the drawback is the increased cost, size, and complexity.

Similar to an array is the use of a reflector antenna, which allows power synthesis occurring at its focal point, but only one source is used. An ellipsoidal reflector was investigated for focusing narrowband signal for microwave hyperthermia [20], but the possibility of using reflector antennas for focusing high power UWB signals in the near field had not been explored. Previously, the studies on high-power ultra-wideband radiation in the time domain were mostly focused on long-range, far-field impulse radiating antennas (IRAs), in which a paraboloid dish was used to focus the input pulses into infinity [72]. These antennas are suited for far-fields with a distance of hundred meters to kilometers from the antenna aperture, but are not suitable for near-field applications. However, a design modification to long-range IRAs was recently proposed [1] by replacing the parabolic reflector with a prolate spheroidal reflector, and yet

retaining the typical conical feed arms. A radiated impulse could be focused in the near field with such modification.
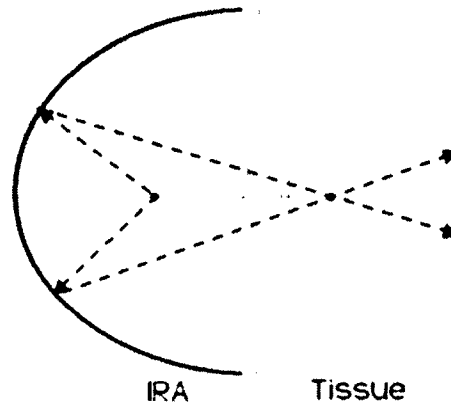
Fig. 1.6. A prolate spheroidal reflector antenna can be used to focus electromagnetic energy in the near field.

In a prolate spheroidal reflector, as shown in Fig. 1.6, when a TEM wave is fed at the first focal point of the parabola, the spherical TEM waves get reflected from all points on the reflector surface and travel towards the second focus. The geometry of the reflector is such that the reflected waves arrive at the second focal point at the same time, resulting in an energy concentration. But this is correct only when the feed signal has a very high frequency at which ray optic theory applies. At a lower frequency, there is a power spread near the focal point.

Like any other antenna, the size of the reflector and wavelength determines the radiated field distribution, which also related to the distance from the antenna. In the far field, electric and magnetic fields are essentially planar and are perpendicular to each other and to the direction of propagation, and the angular field distribution does not depend on the distance from the antenna. The fields are uniquely related to each other via free-space impedance and decay as the inverse of the distance from antenna. In the near field, the field components have different angular and radial dependence, and the fields decay more rapidly than inverse of the distance from antenna. For a focal distance in the near field, the distance R_0 is given by,

$$R_0 < \frac{2D^2}{\lambda} \tag{1.1}$$

Where D is the aperture diameter of the antenna and λ is the wavelength. When the antenna is focused at a distance shorter than D^2/λ, the spot size of the focus is reduced and the spot width, W is approximately proportional to focal distance R_0.

$$W = \frac{\lambda}{D} R_0 \tag{1.2}$$

This shows that large antennas at short wavelengths can result in a small focal spot size to deliver high power densities [73]. In the time domain, pulses with fast rise and fall times are preferable for a small spot size. Given this ability to focus in the near field with a tightly focused wavebeam spot, the prolate spheroidal impulse radiating antenna offers the possibility to focus electromagnetic energy in the near-field.

I.V OBJECTIVE OF THE DISSERTATION

Whereas the previously reported pulse radiating antenna was primarily studied for the proof of concept [1], the antenna characterized in this dissertation is designed a step closer to the actual applications, which require the antenna to be compact and portable. To our knowledge, this is the first IRA with a balanced feed configuration, which focuses the impulse in the near field.

The focus of this dissertation is to study the propagation and electric field distribution of sub-nanosecond pulsed radiation in the near field regions, which include free space, dielectrics and biological targets. This study aims to shed light on the following questions: How deep can the sub-nanosecond pulses penetrate in the tissue and still achieve a reasonable confinement of the electric field distribution? Can only one antenna be used to focus pulsed radiation into tissue? What spatial resolution can such antenna provide?

For target detection, the concept of confocal imaging using a fixed-focus antenna was discussed [39], but the actual implementation was not attempted, primarily because the interest was focused on the antenna array, which has the ability to vary the focus in using the digital beamforming. In this dissertation, the use of a fixed-focus impulse radiating antenna for the confocal target detection is implemented. Target detection using this system is limited to targets in free space. Another possible use would be to detect a target embedded in a weakly scattering object so the focal point can be predetermined as in free space. A lens in conjunction with the antenna is used to decrease the focal spot size and to increase the resolving ability. This lens-antenna system applies in the case when a target is in the subsurface region of a medium with known dielectric properties. The dielectric lens, in conjunction with the antenna, can be used to match the impedance from free space to the medium and to achieve the focus inside the medium. One scenario would be detecting or monitoring cancers in the skin with a lateral scanning at a fixed depth. A future system would be equipped with both detection and treatment capabilities.

Specifically, the research effort is mainly focused in the following five areas:

- focusing of sub-nanosecond pulsed electric fields in the near field using prolate-spheroid reflector antennas,

- increase of spatial resolution by using a dielectric lens in conjunction to the reflector antenna,

- confocal use of the reflector antenna for target detection,

- delivery of sub-nanosecond pulses to biological tissues with the reflector antenna, and

- delivery of sub-nanosecond pulses to biological tissues with the reflector antenna in conjunction with a dielectric lens.

I.VI OUTLINE

In Chapter 2, the basics of impulse radiating antenna will be discussed. Radiation from antenna apertures and formulation of the near field focusing characteristics will be presented. Some concise scaling formulae for focal spot size and pulse width will be shown.

In Chapter 3, the experimental results of measured radiated fields from the antenna will be presented. The measured fields will be compared to analytical results and will be used to evaluate the focusing characteristics of the antenna. The numerical model developed by using CST Microwave Studio will be validated by comparison with the experimental results.

In Chapter 4, basic considerations for the design of a dielectric lens for concentrating electric fields on a target will be discussed. Electric field measurements carried out with the reflector antenna in conjunction with a dielectric lens will be discussed.

In Chapter 5, the capability of the antenna to detect a target will be investigated. Target detection in the near field will be discussed in free space as well as in a medium through dielectric lens. Target detection in the far-field beyond focal distance will be demonstrated by detecting human movements in through wall imaging.

Chapters 6 and 7 will study the delivery of electromagnetic energy to biological targets using the reflector antenna. The 3-D electromagnetic simulation software, CST Microwave Studio® will be used as a simulation tool. Chapter 6 will focus on the delivery of sub-nanosecond pulses to a simple homogeneous biological tissue target. Chapter 7 will extend the study to a realistic biological target by including a human head model as a target.

Chapter 8 will include discussions of the results, and Chapter 9 will conclude this dissertation.

CHAPTER II

BACKGROUND

II.I FEATURES OF ULTRA-WIDEBAND PULSE RADIATION

Traditionally antennas were studied from the frequency domain point of view, where the physical processes are represented in terms of harmonic functions like $sin\omega t$ and $cos\omega t$. In this case, the frequency domain treatment assumes a steady state or time averaging process. In contrast with the narrowband sinusoidal waveforms of single frequency, a UWB system is associated with multiple frequencies or short duration pulses with fast rise times in the order of nanoseconds and picoseconds [74]. The frequency domain treatment is still useful in analyzing a UWB system, but a convolution over a broadband spectrum needs to be conducted to convert the parameters of interest into time domain. Antennas can alternatively be studied from the time domain point of view, where physical processes are treated as transients with definite beginnings and endings. The time domain treatment is preferred for studying propagation delay and generally results in responses that are easier to understand.

Conventional narrowband signals are usually carried by higher carrier frequencies, but a finite number of discrete frequencies are used. As the frequencies of these signals increase, the propagation losses that they experience become greater. On the other hand, UWB signals with wider and continuous bandwidth can achieve high data rates. It follows that UWB signals have the potential for greater penetration of obstacles such as walls than do conventional signals while achieving the same data rate.

Because the UWB pulse can be extremely short, it has a strong temporal and space resolving capability. UWB pulse waveforms, when scattered from objects and surfaces near the path between transmitter and receiver, tend not to overlap in time, making it possible to resolve multipath receptions through time gating.

The radiation of UWB pulses can be understood by a linear antenna such as a Hertzian electric dipole [74] where the electric and magnetic field strengths, E and H, radiated to the far field are directly proportional to the first time-derivative of the excitation current $i(t)$.

$$(E, H)_{far-field} \propto \frac{di(t)}{dt} \tag{2.1}$$

For narrowband system, where a signal has a sinusoidal waveform, the derivative will appear as a cosine waveform. So the input -output transfer function will be linear with just an addition of phase shift term. But if we consider an exciting current pulse having the Gaussian form, this pulse creates the far-field doublet determined by its derivative as shown in Fig. 2.1.
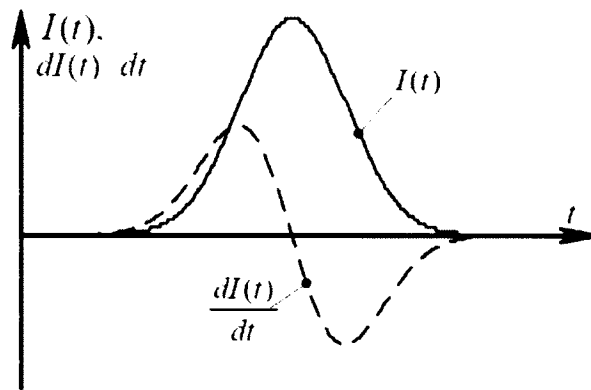
Fig. 2.1. A Gaussian current pulse as an excitation and the transmitted derivative waveform.

II.II RADIATION FROM APERTURES

While linear antennas like dipoles and loops can be analyzed from the change of current in time, i. e. the acceleration of charges, in antennas where the radiation occurs from an aperture, the current distribution is often not obvious, and needs to be determined from the concept of equivalent current, such as magnetic current. Such antennas include reflectors and horn antennas.

Aperture antennas are analyzed using aperture theory, which is based upon the fact that an electromagnetic field in a source-free closed region is completely determined by the values of a tangential electric (magnetic current) or magnetic field (magnetic dipole) on the surface of the closed region. Huygen's principle, or the field equivalence principle [75-76], forms the basis of aperture theory. In essence, field equivalence is a principle by which an actual source can be replaced by a set of equivalent sources (either magnetic current or magnetic dipole) spread over a specified closed surface S, as shown in Fig. 2.2.
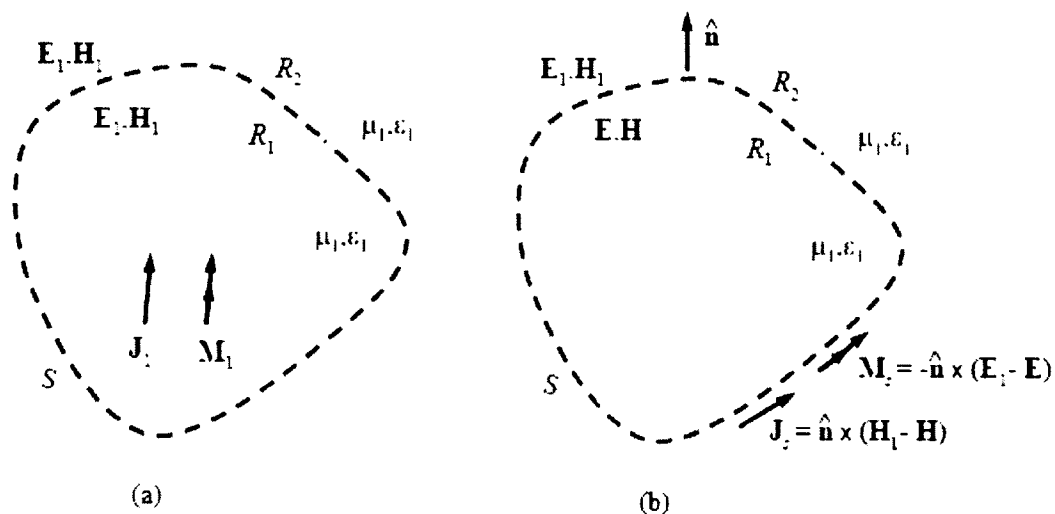
Fig. 2.2. Field equivalence theorem: (a) an original problem, and (b) an equivalent problem.

II.III ELECTROMAGNETIC FIELDS FROM ARBITRARY APERTURE FIELDS

For the aperture system shown in Fig. 2.3, the basic problem is to find the field pattern for all z' when the field distribution for $z' = 0$ is known. The assumed tangential field distribution on surface S' is $E_t' = (E_x', E_y', 0)$. The mathematical procedure starts from the concept of field equivalence, where irradiating sources are replaced by a set of equivalent sources spread over a specified closed surface S' at $r'(x', y', 0)$. For the fields to satisfy Maxwell's equations and the boundary conditions, the equivalent sources are either a magnetic surface current or an electric surface current, which generate a field outside the surface S', as shown in Fig. 2.3.
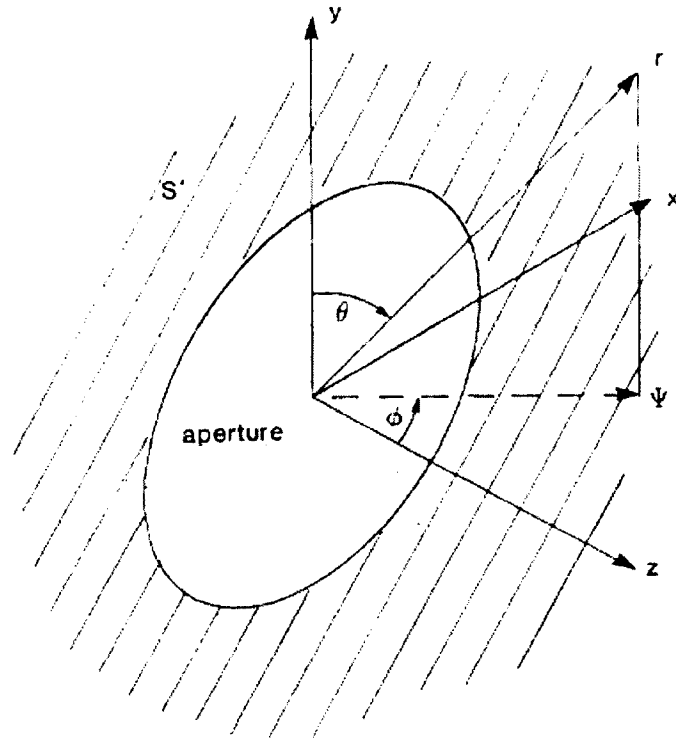
S' is defined

by $\bar{r}'=(x',y',0)$.

Fig. 2.3. Electromagnetic fields from a source plane S'. Reprinted, with permission, from [77].

One of the equivalent current density formulations over the surface is to assume magnetic equivalent currents plus a perfect electric conductor boundary by knowing the tangential electric fields. In this case, the whole $z' = 0$ plane, except the aperture, is replaced with a perfect electric conductor and the radiated fields are found using the magnetic current, J_m. In order to account for a perfect conductor, the effect of the current source plus its image is accounted for by using a magnetic current source of twice the magnitude radiating into free space. Now, to compute the electric fields at an observer position r(x, y, z), we define the distance from the surface element to an observer, R, as

$$R = |r - r'| = \sqrt{(x-x')^2 + (y-y')^2 + z^2}$$

(2.2)

And, the unit normal to the surface as,

$$\bar{T}_R = \frac{x-x'}{R}\bar{T}_x + \frac{y-y'}{R}\bar{T}_y + \frac{z}{R}\bar{T}_z \qquad (2.3)$$

Then the magnetic current is given by,

$$2\bar{J}_m = -2\bar{T}_z \times \bar{E}_t \qquad (2.4)$$

Now, if $s=j\omega$ gives the complex frequency and c is the velocity of light, the propagation constant in complex frequency domain is given by, $\gamma=s/c$. Then the equivalent set of magnetic current sources on S' give a vector potential as follows [77, 78],

$$\tilde{A}(\bar{r},s) = \frac{-1}{2\pi s}\int_{S'}\frac{1+\gamma R}{R^2}((\bar{T}_z \times \tilde{E}_t) \times \bar{T}_R)e^{-\gamma R}dS' \qquad (2.5)$$

Next we have,

$$\bar{B} = \nabla \times \bar{A} \qquad \text{and} \qquad \nabla \times \bar{E} = -\partial \bar{B}/\partial t \qquad (2.6)$$

Combining two equations of Eqn. 2.6, we have,

$$\nabla \times \bar{E} = -\nabla \times \partial \bar{A}/\partial t \qquad (2.7)$$

Because the scalar potential of a magnetic current distribution is zero, this yields,

$$\bar{E} = -\partial \bar{A}/\partial t \qquad \Rightarrow \qquad \tilde{E} = -s\tilde{A} \qquad (2.8)$$

Hence the electric field distribution at a point **r** can be written as,

$$\tilde{E}(\bar{r},s) = \frac{1}{2\pi}\int_{S'}\frac{1+\gamma R}{R^2}((\bar{T}_z \times \tilde{E}_t') \times \bar{T}_R)e^{-\gamma R}dS' \qquad (2.9)$$

where,

$$(\vec{T}_z \times \widetilde{E}_t') \times \vec{T}_R = \left(E_x' \frac{z}{R} \right) \vec{T}_x + \left(E_y' \frac{z}{R} \right) \vec{T}_y - \left(\frac{x-x'}{R} E_x' + \frac{y-y'}{R} E_y' \right) \vec{T}_z \quad (2.10)$$

Thus, by assuming a distribution of tangential electric field E_t' on the aperture, we arrive at Eqn. 2.9, which can be used to calculate electric fields throughout the space in terms of the integrals over the aperture. We can see that the electric field has a dependence on R^{-1} and R^{-2} terms. The electric field equations in component forms are then written as,

$$\widetilde{E}_x(\vec{r}_0, s) = \frac{1}{2\pi} \int_{S'} \frac{1+\gamma R}{R^2} \frac{z}{R} e^{-\gamma R} \widetilde{E}_x' dS'$$

$$\widetilde{E}_y(\vec{r}_0, s) = \frac{1}{2\pi} \int_{S'} \frac{1+\gamma R}{R^2} \frac{z}{R} e^{-\gamma R} \widetilde{E}_y' dS' \quad (2.11)$$

$$\widetilde{E}_z(\vec{r}_0, s) = \frac{1}{2\pi} \int_{S'} \frac{1+\gamma R}{R^2} e^{-\gamma R} \left[\frac{x-x'}{R} \widetilde{E}_x' + \frac{y-y'}{R} \widetilde{E}_y' \right] dS'$$

II.IV FOCUSING ELECTROMAGNETIC FIELDS FROM AN APERTURE

If the phase of the tangential electric field source on S' is such that a fixed observer at $r = r_0$ receives signals from each elementary position from S' at the same phase, then the field at r_0 is a focused field. Then at distance r_0,

$$R = |r_0 - r| \quad \text{and} \quad R_0 = |r_0| = r_0 \quad (2.12)$$

For focusing at r_0, the signals arriving at r_0 from all elementary sources at a given time t have a same waveform, $f(t)$, but may have different amplitudes. Hence a constraint is applied as,

$$e^{-\gamma R} \widetilde{E}_t' = e^{-\gamma R_0} \widetilde{F}(s) E_0 \bar{g}(x', y') \quad (2.13)$$

Substituting into the electric field equations of Eqn. 2.11, gives the electric field at the focus. Hence, in terms of components, the electric field at focus is,

$$\widetilde{E}_x(\vec{r}_0,s) = \frac{e^{-\gamma R_0}}{2\pi} E_0 \widetilde{F}(s) \int_{S'} \frac{1+\gamma R}{R^2} \frac{z_0}{R} g_x(x',y')dS'$$

$$\widetilde{E}_y(\vec{r}_0,s) = \frac{e^{-\gamma R_0}}{2\pi} E_0 \widetilde{F}(s) \int_{S'} \frac{1+\gamma R}{R^2} \frac{z_0}{R} g_y(x',y')dS' \qquad (2.14)$$

$$\widetilde{E}_z(\vec{r}_0,s) = \frac{e^{-\gamma R_0}}{2\pi} E_0 \widetilde{F}(s) \int_{S'} \frac{1+\gamma R}{R^2} \left[\frac{x_0-x'}{R} g_x(x',y') + \frac{y_0-y'}{R} g_y(x',y') \right] dS'$$

After allowing for the delay term and source waveform, the electric field expressions can be reduced by consolidating frequency independent terms and dimensionless terms into coefficient α as follows.

$$\widetilde{E}_x(\vec{r}_0,s) = E_0 e^{-\gamma R_0} \widetilde{F}(s) \left(\alpha_x^{(1)} \frac{1}{R_0} \frac{s}{c} + \alpha_x^{(2)} \frac{1}{R_0^2} \right)$$

$$\widetilde{E}_y(\vec{r}_0,s) = E_0 e^{-\gamma R_0} \widetilde{F}(s) \left(\alpha_y^{(1)} \frac{1}{R_0} \frac{s}{c} + \alpha_y^{(2)} \frac{1}{R_0^2} \right) \qquad (2.15)$$

$$\widetilde{E}_z(\vec{r}_0,s) = E_0 e^{-\gamma R_0} \widetilde{F}(s) \left((\alpha_{zx}^{(1)} + \alpha_{zy}^{(1)}) \frac{1}{R_0} \frac{s}{c} + (\alpha_{zx}^{(2)} + \alpha_{zy}^{(2)}) \frac{1}{R_0^2} \right)$$

where, the coefficients depend on $\mathbf{r}_0$ and the spatial distribution on the source, and are given by,

$$\alpha_x^{(1)} = \frac{R_0 z_0}{2\pi} \int_{S'} [(x_0-x')^2 + (y_0-y')^2 + z_0^2]^{-1} g_x(x',y')dS'$$

$$\alpha_y^{(1)} = \frac{R_0 z_0}{2\pi} \int_{S'} [(x_0-x')^2 + (y_0-y')^2 + z_0^2]^{-1} g_y(x',y')dS'$$

$$\qquad (2.16a)$$

$$\alpha_{zx}^{(1)} = \frac{R_0}{2\pi} \int_{S'} [(x_0-x')^2 + (y_0-y')^2 + z_0^2]^{-1} (x_0-x')g_x(x',y')dS'$$

$$\alpha_{zy}^{(1)} = \frac{R_0}{2\pi} \int_{S'} [(x_0-x')^2 + (y_0-y')^2 + z_0^2]^{-1} (y_0-y')g_y(x',y')dS'$$

$$\alpha_x^{(2)} = \frac{R_0^2 z_0}{2\pi} \int_{S'} [(x_0 - x')^2 + (y_0 - y')^2 + z_0^2]^{-3/2} g_x(x', y') dS'$$

$$\alpha_y^{(2)} = \frac{R_0^2 z_0}{2\pi} \int_{S'} [(x_0 - x')^2 + (y_0 - y')^2 + z_0^2]^{-3/2} g_y(x', y') dS'$$

$$\alpha_{zx}^{(2)} = \frac{R_0^2}{2\pi} \int_{S'} [(x_0 - x')^2 + (y_0 - y')^2 + z_0^2]^{-3/2} (x_0 - x') g_x(x', y') dS'$$ (2.16b)

$$\alpha_{zy}^{(2)} = \frac{R_0^2}{2\pi} \int_{S'} [(x_0 - x')^2 + (y_0 - y')^2 + z_0^2]^{-3/2} (y_0 - y') g_y(x', y') dS$$

According to Eqn. 2.15, the electric field has terms free of s and proportional to s. Since multiplication by s in a Laplace domain is equivalent to the derivative in time domain, and the phase shift $e^{-\gamma R_0}$ is equivalent to the time delay t-R_0/c, the above Laplace domain results can be directly converted into the time domain as follows:

$$E_x(\vec{r}_0, t) = E_0 \left(\alpha_x^{(1)} \frac{1}{R_0 c} \frac{\partial f(t - R_0/c)}{\partial t} + \alpha_x^{(2)} \frac{1}{R_0^2} f(t - R_0/c) \right)$$

$$E_y(\vec{r}_0, t) = E_0 \left(\alpha_y^{(1)} \frac{1}{R_0 c} \frac{\partial f(t - R_0/c)}{\partial t} + \alpha_y^{(2)} \frac{1}{R_0^2} f(t - R_0/c) \right)$$ (2.17)

$$E_z(\vec{r}_0, t) = E_0 \left((\alpha_{zx}^{(1)} + \alpha_{zy}^{(1)}) \frac{1}{R_0 c} \frac{\partial f(t - R_0/c)}{\partial t} + (\alpha_{zx}^{(2)} + \alpha_{zy}^{(2)}) \frac{1}{R_0^2} f(t - R_0/c) \right)$$

Eqn. 2.17 gives the time domain form of the electric field at the focus of the antenna which consists of two terms: a derivative waveform and the replicate of the waveform itself.

II.V RADIATION FROM A PROLATE SPHEROIDAL REFLECTOR ANTENNA

A prolate spheroidal reflector antenna is a specific case of focusing aperture antennas discussed in previous section. This is based on the two foci of an ellipse, whose major axis is given by a, whose minor axis is given by b and the focal distance is z_0. The schematics of the antenna is shown in Fig. 2.4.
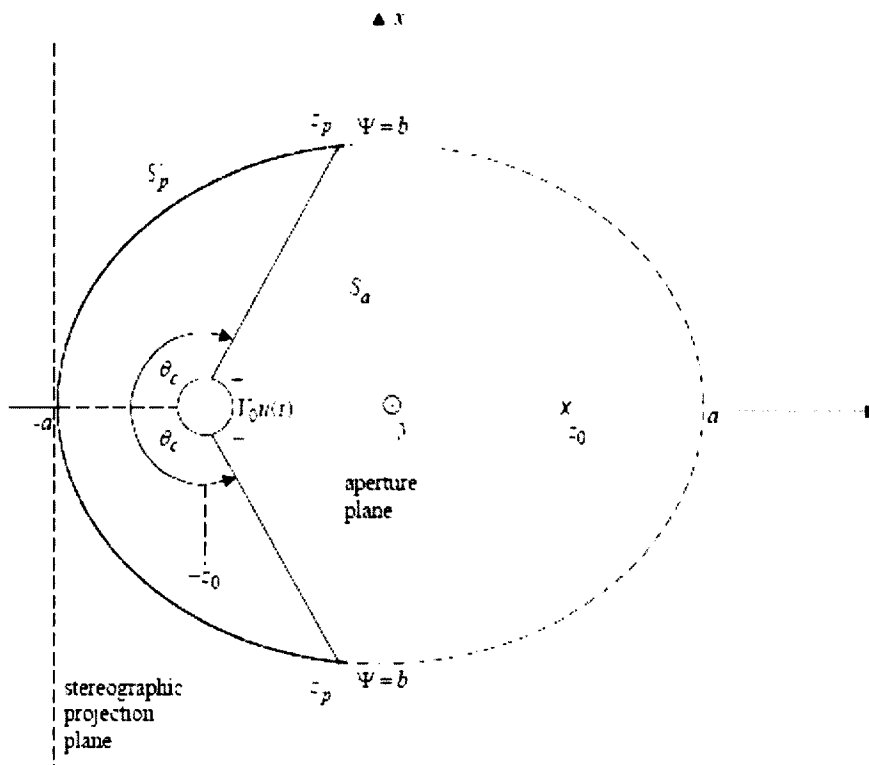
Fig. 2.4. Schematic diagram of a prolate spheroidal reflector. Reprinted, with permission, from [1].

If (ψ, ϕ, z) denotes the cylindrical coordinate system and (x, y, z) denotes the Cartesian coordinates, the prolate sphere in cylindrical coordinates is defined by the equation,

$$\left[\frac{\psi}{b}\right]^2 + \left[\frac{z}{a}\right]^2 = 1 \quad , \quad a > b$$

where, $\quad x = \psi \cos\phi, \qquad y = \psi \sin\phi, \qquad \psi^2 = x^2 + y^2$ \hfill (2.18)

and, $\quad z_0^2 = a^2 - b^2$

which has two foci placed at $(0, \phi, \pm z_0) = \pm r_0$.

When a TEM spherical wave is launched at the first focal point, a portion of the wave travels towards the second focal point directly, while the remaining portion travels towards the reflecting surface, guided by the conical conductors. These waves are reflected by the surface S'_p

towards the second focal point. The distance traveled by a ray from $-\mathbf{r_0}$ to $\mathbf{r_0}$ is always the same, given by $2a$.

II.V.I Tangential Electric Field at Aperture

As shown in Fig. 2.4, the prolate spheroidal reflector is truncated at the $z = z_p = 0$ plane. Following the analysis done in the previous section, the truncation plane gives the aperture plane S_a, which is a disk of radius b. With the knowledge of the tangential electric field, the equivalent surface magnetic current can be integrated over the surface to find the fields at the second focus, $\mathbf{r_0}$.

The analysis in [79] shows that an inhomogeneous spherical TEM wave launched on guiding conical conductors from one focus is converted by a double stereographic projection to a second (reflected) inhomogeneous spherical TEM wave propagating towards second focus. Hence for the first launched wave, in spherical coordinates $(r_1,\ \theta_1,\ \phi_1)$ centered on $-\mathbf{r_0}$, with $\theta_1=0$, an outward propagating inhomogeneous TEM wave is given by,

$$\vec{E}_1 = -\frac{1}{r_1}\nabla_{\theta_1,\phi_1}V_1(\theta_1,\phi_1)f\left(t - \frac{r_1}{c}\right)$$ (2.19)

Now if $(\psi_0,\ \phi_0)$ are the cylindrical coordinates at the stereographic projection plane $z = -a$,

$$\psi_0 = 2[a - z_0]\tan\left(\frac{\theta_1}{2}\right) \qquad \text{and} \qquad \phi_0 = \phi_1 = -\phi$$ (2.20)

Similarly for second reflected wave, a spherical coordinates $(r_2,\ \theta_2,\ \phi_2)$ centered on $\mathbf{r_0}$, an inward propagating inhomogeneous TEM wave is given by,

$$\vec{E}_2 = -\frac{1}{r_2}\nabla_{\theta_2,\phi_2}V_2(\theta_2,\phi_2)f\left(t + \frac{r_2}{c} - \frac{2a}{c}\right)$$ (2.21)

Now if (ψ_0, ϕ_0) is the cylindrical coordinates at the stereographic projection plane $z = -a$,

$$\psi_0 = 2[a + z_0]\tan\left(\frac{\theta_2}{2}\right) \qquad \text{and} \qquad \phi_0 = -\phi_2 = -\phi \qquad (2.22)$$

The reflected wave is related to the first wave in such a way that they are equal and travel in opposite directions at the stereographic projection plane. Hence,

$$V_2(\psi_0, \phi_0) = -V_1(\psi_0, \phi_0) \qquad (2.23)$$

This stereographic projection is used to determine the tangential electric field on S_a for the aperture integral.

II.V.II Focal Waveform of a Prolate Spheroidal IRA

Analytic calculations of the waveform at the second focus has been performed [1] when the first focus is excited using the time-domain waveform as a step function $V_0 u(t)$. The part of the waves that arrive from the first focus directly to the second focal point without any reflection is known as prepulse and is given by,

$$\vec{E}_1 = -E_p u\left(t - \frac{2z_0}{c}\right)\hat{x} \qquad (2.24)$$

Eqn. 2.24 gives the prepulse orientation and magnitude for a step excitation. The direct wave arrives at the second focus at a time $2z_0/c$, while the reflected wave arrives at $2a/c$. Hence, the length of prepulse is given by,

$$\Delta t_p = \frac{2[a - z_0]}{c} \qquad (2.25)$$

For the part of the wave that is reflected from the prolate spheroidal reflector, the tangential electric field is calculated using stereographic projection as,

$$E_{2x} = E'_{2x} u\left(t + \frac{r_2}{c} - \frac{2a}{c}\right)$$

(2.26)

Then according to Eqn. 2.17, the field at focus is given by,

$$E_{fx} = E_\delta \delta\left(t - \frac{2a}{c}\right) + E_s u\left(t - \frac{2a}{c}\right)$$

where, $\quad E_\delta = \frac{1}{2\pi c} \int_{S_a} \frac{z_0 - z_p}{r_2} E'_{2x}\, ds \quad$ and $\quad E_s = \frac{1}{2\pi} \int_{S_a} \frac{z_0 - z_p}{r_2^3} E'_{2x}\, ds$

(2.27)

E_δ and E_S are the impulsive and step terms from the reflection on the prolate spheroidal reflector, and E_p is the magnitude of the prepulse wave from the first focus. The values of these terms are given as follows:

$$E_\delta = \frac{E_0}{c}\frac{b^2}{a} \approx \frac{V_0}{\pi f_g c}\frac{b}{a}$$

$$E_s = \frac{E_0}{2}\frac{a+z_0}{z_0}\frac{b^2}{a^2} \approx \frac{V_0}{2\pi f_g}\frac{a+z_0}{z_0}\frac{b}{a^2}$$

(2.28)

$$E_p = \frac{E_0}{2}\frac{a+z_0}{z_0} \approx \frac{V_0}{2\pi f_g}\frac{a+z_0}{bz_0}$$

Here, f_g is the ratio of the characteristic impedance to the wave impedance of medium.

Although mathematically the first term of Eqn. 2.27 shows an impulsive function, in reality, the input step function will have a finite rise time and hence, the impulse term will have a finite amplitude and finite width. If the rise time of the input unit step is t_δ, then the corresponding impulse function will have a width of t_δ and amplitude of $1/t_\delta$. So the impulsive part of the field has an amplitude of E_δ/t_δ.

$$\delta(t) \rightarrow \frac{1}{t_\delta}\left[u(t) - u(t - t_\delta)\right]$$

(2.29)

With all these factors considered, the analytic waveform for an excitation of 1V step function with a rise time t_δ of 100ps is shown in Fig. 2.5 [80].

E-Field (V/m)

$$\frac{E_\delta}{t_\delta} - E_{p2} + E_s$$

$$\frac{E_\delta}{t_\delta} - E_p$$

$t_\delta = 100\,ps$

$E_s - E_{p2}$

4.2

3.6

0.2

2.5 ns

4.2 ns

Time (ns)

-0.4

$-E_p$
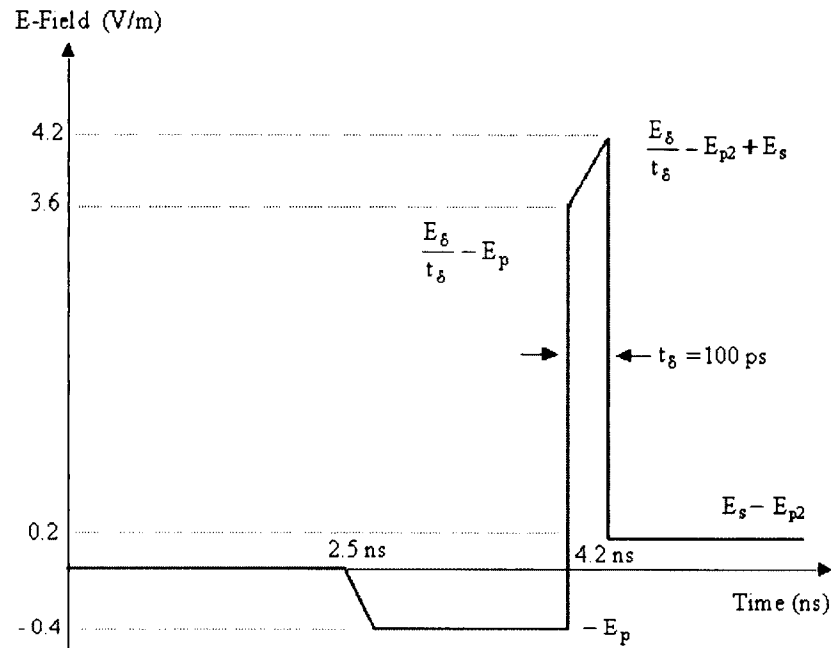
Fig. 2.5. Analytic waveform at the second focus for a step excitation. Reprinted, with permission, from [80].

As it is clear from Fig. 2.5, the field radiated from an impulse radiating antenna driven by a step-function source consists of three distinct parts. First, there is a prepulse, radiated directly from the conical transmission line. Following this comes the impulse, which is the reflected signal from a spheroidal reflector, and which arrives at the second focus coherently. It is proportional to the time derivative of the feed pulse. Finally, there is a tail with a lower magnitude, known as postpulse, due to multiple reflections at antenna discontinuities.

Because the amplitude of impulsive part of the field is proportional to the inverse of rise time, t_δ, it implies that an input step with a faster rise time allows for higher impulse with narrow width. Also, if we compare the impulse and prepulse amplitudes,

$$\frac{E_\delta}{E_p} = \frac{2}{c}\frac{b^2}{a}\frac{z_0}{a+z_0} = \frac{z_0}{a}\frac{b^2}{c}\frac{2[a-z_0]}{a^2-z_0^2} = \frac{z_0}{a}\Delta t_p \qquad (2.30)$$

A large value of the ratio z_0/a gives a large impulse.

II.V.III Focal Spot Size of a Prolate Spheroidal IRA

As discussed in the previous sub-section, due to finite rise time of input step function, the resulting impulse at the focus has a width of t_δ. It follows that the maximum field exists in a small region around the second focal point, $\mathbf{r_0}$. Now, for an observer displaced Δz from the second focal point, the pulse width seen with respect to z-axis is the difference of arrival time of a wave from the center of the reflector to that from the edge of the reflector, given by,

$$t_z = \left[1 - \frac{z_0}{a}\right]\frac{|\Delta z|}{c} \qquad (2.31)$$

Similarly, for an observer radially displaced $\Delta\psi$ from the second focal point, the pulse width seen with respect to ψ-axis is the difference of the arrival time of a wave from the far edge to that from the near edge of the reflector, and is given by,

$$t_\psi = 2\frac{b}{a}\frac{\Delta\psi}{c} \qquad (2.32)$$

Both in z- and ψ- directions, a large z_0/a and correspondingly a small b/a ratio is required to reduce the pulse width as indicated by Eqn. 2.31 and 2.32.

Moreover, if the pulse width, t_δ is comparable to the pulse width at the second focal point, it can be noted that the pulse width in z-direction will be $t_\delta+t_z$ and that in the ψ- direction will be $t_\delta+t_\psi$. Hence the effective physical focal spot size is given by $2t_\delta$.

In conclusion, an input with fast rise time results in a high amplitude of impulse at the focus and a small focal spot size.

CHAPTER III

ANTENNA CHARACTERIZATION

An impulse radiating antenna (IRA) has a reflector that is fed by a spherical TEM wave at its first focal point. The TEM feed arms guide the outwardly propagating spherical TEM wave, which is launched at the apex of the TEM feed arms. The reflector converts the spherical wave into an equi-phase field at the aperture. For a given field in an aperture, the time domain analysis can be performed to evaluate the field at the focal point [77]. When the first focal point of an impulse radiating antenna is excited using a step function, the focal waveform at the second focus consists of a prepulse, and impulse and a postpulse. The impulse part of the focal waveform, which is the reflected signal from the reflector, arrives at the focus coherently and is proportional to the time derivative of the feed.

This chapter presents the experimental studies carried out to measure the fields at different distances from the antenna. The measured fields are compared with the focusing characteristics of the antenna predicted from analytical results. Moreover, the simulations results using CST Microwave Studio® are presented and a comparison of simulated and experimental results is made.

III.I DESCRIPTION OF ANTENNA

The antenna under consideration is the prolate spheroidal impulse radiating antenna designed by Carl E. Baum [1] at the University of New Mexico (UNM) and constructed by Farr Research. The antenna acquired by Frank Reidy Research Center for Bioelectrics at Old Dominion University (ODU) is a smaller version of the impulse radiating antennas at UNM. It has an aperture diameter of 0.5m and uses a balanced feed configuration, whereas the one at UNM has a 1m aperture and half of the reflector. The feed arm can be directly connected with the coaxial cable, removing the need of a balun.

The antenna at ODU, as shown in Fig. 3.1, consists of a prolate spheroidal reflector, a symmetrical conical feed structure, and a balun. The major axis, a, and the minor axis, b, are 29.8cm and 25cm respectively. The focal point, z_0, is at 16.3cm from the antenna aperture.
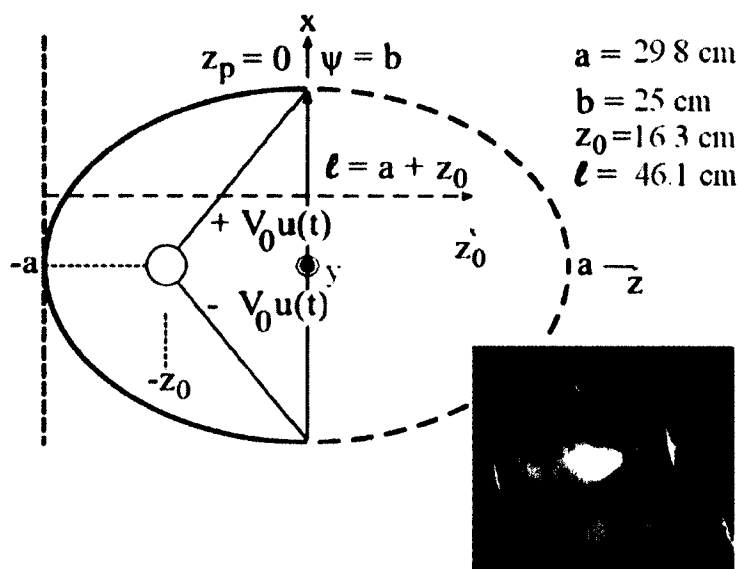
Fig. 3.1. The impulse radiating antenna geometry and the actual antenna.

The feed arm geometry is shown in Fig. 3.2. The conical feed arms are symmetric about the y-axis, and consist of two pairs of parallel conical plates. They extend from the first focal point toward the reflector, each arranged at an angle (Φ_0) of 60° with respect to the y-axis.
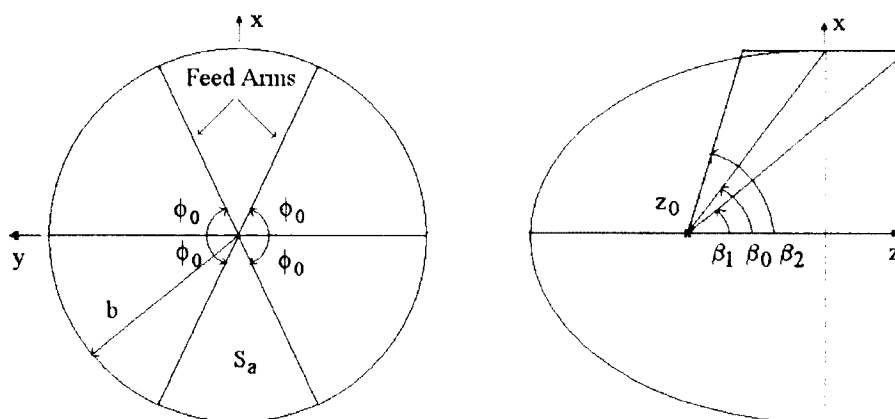
Fig. 3.2. Feed arm geometry: the four feed arms are arranged at $\Phi_0 = 60°$ with respect to the y-axis, whereas the angles with respect to z-axis are $\beta_0 = 53.1°$, $\beta_1 = 47°$ and $\beta_2 = 59.6°$. Reprinted, with permission, from [80].

The TEM feed arms are connected to the reflector through a number of resistors for matching the low frequency components of the feed signal. The total resistance is $Z_0/2$ so that the TEM feed arms with a characteristic impedance of Z_0 are matched in impedance. The feed arms are designed to have an impedance of 200Ω. Normally, a pulse input has an impedance of 50Ω from the pulse source, which is transformed to match the conical transmission line (200Ω) through a balun made of two 100Ω cables connected in parallel on one side and in series on the other side.

Because of the resistive termination matched to the feed line, which in turn is matched to the pulse source, the antenna behaves as a matched load during transmission. There is no resonance in the transmission line, so the radiated wave is a travelling wave.
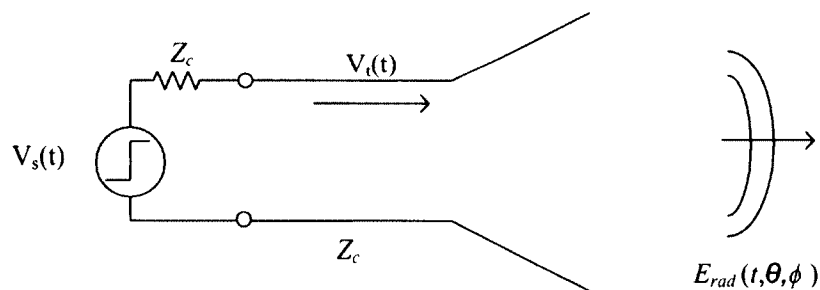
Fig. 3.3 A transient antenna in transmit mode acts like a matched load to the pulse source.

III.II EXPERIMENTAL SETUP

In order to investigate the focusing of pulsed electromagnetic radiation in the near field region by the prolate spheroidal reflector antenna, experiments are setup to measure the electric field distribution in free space [81].

III.II.I Antenna Excitation

The antenna is fed with pulses having a rise time of 200ps from the pulse generator FPG5-10PM manufactured by FID Technology. The pulse generator and the pulse waveform are shown in Fig. 3.4. The pulse width (60% maximum) is approximately 200ps. A prepulse and a postpulse broadens the entire pulse width but can be identified with respect to the main pulse. The shown figure is normalized to its maximum (approximately 5kV, measured by a resistive attenuator, Barth High Voltage Pulse Attenuator, Model 142-NMFP-26B).
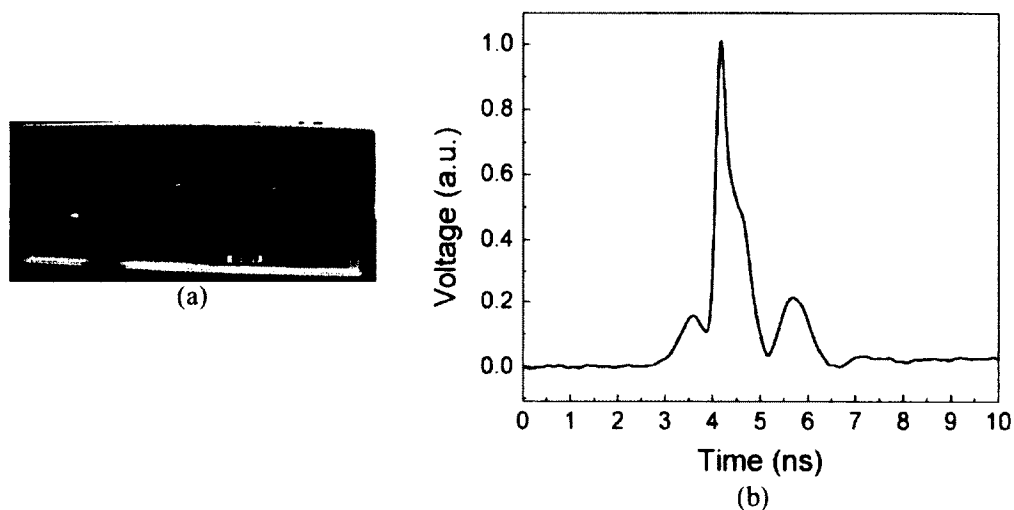
Fig. 3.4. (a) The pulse generator FPG5-10PM manufactured by FID Technology and (b) the pulse having a rise time of 200ps.

III.II.II Receiver Antenna

The receiver antenna used in the experiments is a 2-conductor TEM horn with an aperture of 3.5cm × 4cm as shown in Fig. 3.5. It consists of two conical transmission lines, bending in a smooth profile and forming a TEM horn. One line is grounded and the other is connected with two 100Ω SMA resistors before connecting to the ground. The antenna has the same polarization as the transmitting prolate spheroidal antenna and measures the time rate change of electric displacement field [82]. Hence, the measured signal needs to be integrated in time to obtain the actual electric field at a given point of measurement. The radiated electric field of the antenna is

measured at different distances from the antenna and integrated and recorded using a TDS7404 (Tektronix) oscilloscope. The calibration of this receiver is mainly done by comparing the received signal in the time domain with the prepulse of the antenna, which is the replicate of the input pulse from the pulse generator (shown in Fig.3.4).

Fig. 3.5. TEM horn antenna used as a receiver.

III.III 3D SIMULATION SETUP

Electromagnetic simulation has become mature for analyzing the characteristics of given UWB antenna and the codes are commercially available. Time domain computation packages, such as CST Microwave Studio Suite, provide a suitable platform for emulating the performance of a radiating element when excited by pulsed UWB signals [83].

III.III.I Modeling Software: CST Microwave Studio

Computer Simulation Technology (CST) Microwave Studio (MWS) is a 3D EM simulation software. CST MWS enables the fast and accurate analysis of high frequency (HF) devices such as antennas, filters, couplers, planar and multi-layer structures. There are several solvers available within the CST STUDIO SUITE, like time domain and frequency domain solvers, and each of the solvers is specialized for a certain application. The frequency domain solver is based on the Finite Element Method (FEM), whereas the transient solver of CST MWS

is a general purpose 3D EM simulator based on Finite Integration Technique. The Finite Integration Technique (FIT) provides a discrete reformulation of Maxwell's equations in their integral form and allows the simulation of real-world electromagnetic field problems with complex geometries [84]. In order to simulate and visualize the propagation of electromagnetic fields like those from antennas, the transient solver is used.

The modeling in general starts firstly by defining the model geometry and electrical properties of the objects in the user-defined configuration. In Finite Integration Technique, a hexahedral based grid is used to mesh the structure. Secondly, unique solver methods such as the Perfect Boundary Approximation (PBA) for curvature allows the user to refine the boundary and reduce the computational effort needed by the simulation. PBA [85] is a conformal method, which allows arbitrarily shaped objects to be sampled rather coarsely on the mesh. This reduces the mesh and thus also the required memory size and solution time without compromising accuracy. Moreover, CST MWS also implements the Multilevel Subgridding Scheme [86]. It allows mesh lines to start and stop anywhere in the simulation area. CST MWS fits the shape of the individual objects with nested, conformal layers of increasingly finer mesh. So the time domain solver is a suitable solver for studying ultra-wideband antennas with complex geometry, like prolate-spheroidal antenna.

The geometry of the simulated antenna is based on the existing reflector antenna of Fig. 3.1, where the antenna has a prolate spheroidal reflector fed by a transverse electromagnetic conical transmission line starting from first focus as a wave launcher. The matching resistors, however, are not included. Such a treatment will not affect the field distributions of the prepulse and impulse, but the postpulse will be distorted. Since examining the prepulse and impulse is of main interest here, omitting the resistors does not have significant impact in the results of the simulation.

III.III.II Feed Signal in the Modeling

Once the geometry is generated, a signal can be fed to first focal point of the modeled antenna through a V-port. In experimental characterization of the antenna, the pulser used to evaluate the antenna is a FID G2039 pulse generator, which delivers a pulse with a maximum of 5 kilovolts of amplitude, a 250 nanosecond pulse width, and a rise time of 200 picoseconds. In order to model that pulse waveform, a Gaussian pulse signal with pulse width of 200ps, as shown in Fig. 3.6, is used as an input. The frequency range is set to 0-5GHz.
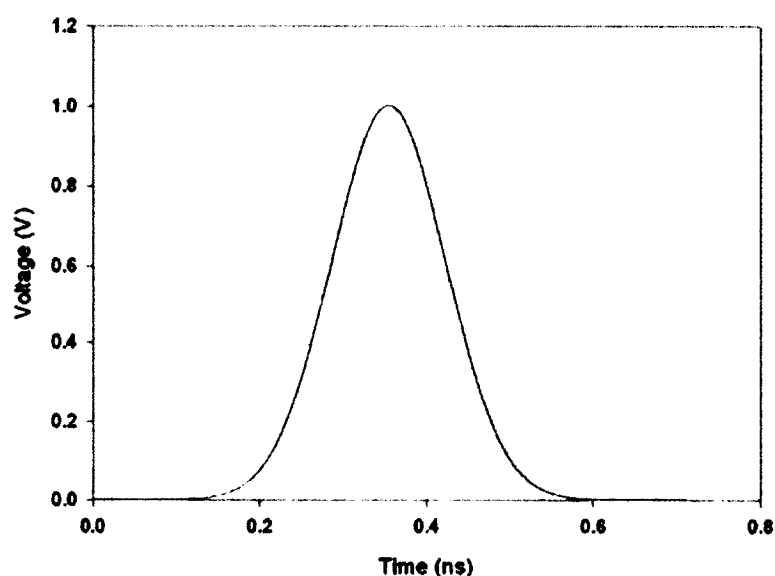
Fig. 3.6 Input Gaussian pulse with 200ps rise time.

III.IV EXPERIMENTAL AND SIMULATION RESULTS

III.IV.I Field at Focus

Using the 2-conductor TEM horn with an aperture of 3.5cm × 4cm as a receiver, the radiated electric field of the antenna at the focal distance $z = 16$cm is measured and recorded using a TDS7404 (Tektronix) oscilloscope. The oscilloscope has a bandwidth of 4GHz and a sampling rate of 20GHz/s. The electric field at the second focal point is shown in Fig. 3.7 and it is the result of the integrated waveform from the oscilloscope.
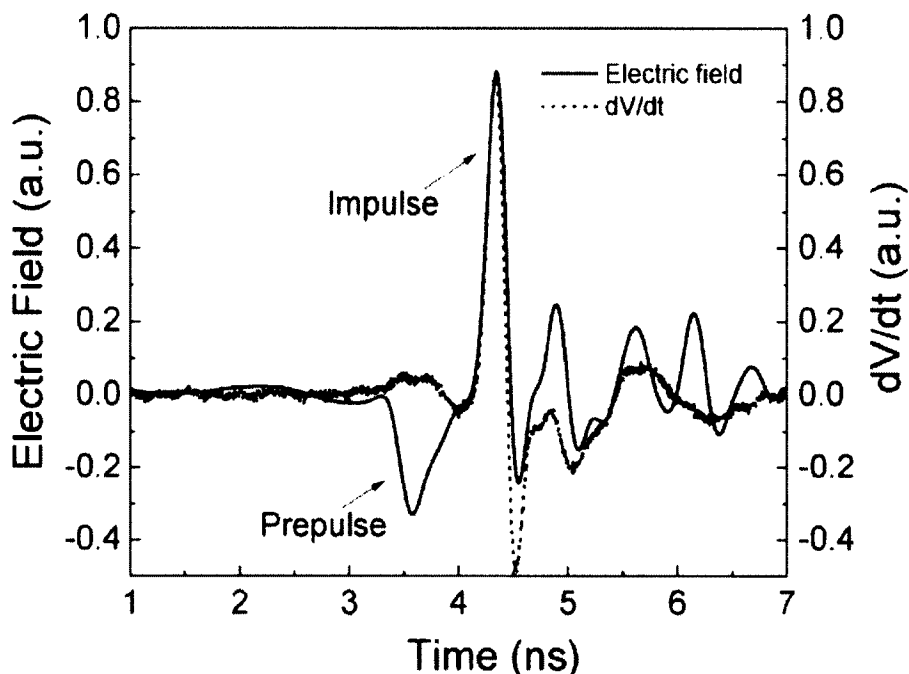
Fig. 3.7. Measured electric field at the focus of the impulse radiating antenna, and the dashed line shows the differentiation of input pulse normalized to the impulse amplitude.

As indicated by the analytic expressions in the previous chapter, the waveform at the focal point comprises of prepulse, impulse and postpulse in the time domain. The prepulse is caused by the diffraction at the conical feed arm. The impulse is the reflected signal from the reflector, which is focused at the second focal point, and the postpulse is largely due to the multiple reflections at the impedance discontinuities.

In Fig. 3.7, the prepulse is wider than the impulse, since the prepulse is just the replica of the input pulse and the impulse is proportional to the time derivative of the feed pulse shown in Fig. 3.4b. The feed pulse, which was directly measured from the pulse generator, was differentiated to obtain dV/dt (dashed line in Fig. 3.7). Apparently, the impulse part of the electric field is overlapped with dV/dt. The difference of frequency components of prepulse and impulse allows us to use a high-pass filter to suppress the prepulse and enhance the impulse in future applications, such as in a near-field radar. The separation in time between these two pulses,

defined as cleartime, is approximately 1ns. The postpulse after t = 4.5ns may contain both diffractions from various parts of the antenna (reflector rim, edge of the conical plate, etc.) and the resonance signal of the sensor itself.

III.IV.II Electric Field Distribution in Free Space

The field measurements are extended to measure electric fields at different points along the axial direction from the antenna aperture as well as at different points along the radial distance on the focal plane. The electric field distribution of this antenna is also modeled by CST Microwave Studio, a 3-D electromagnetic simulation software. A Gaussian waveform with a half-width of 200ps is used as an input excitation. Measurements of electric fields are done by placing probes along different distances in lateral and axial directions to match the experimental case.

The measured amplitudes of both prepulse and impulses are plotted in both lateral (y) and axial (z) directions. The resulting plot is as shown in Fig. 3.8. The modeled distributions of the impulse in the axial direction and the lateral direction are also plotted in Fig. 3.8(a) and (b), respectively, and it is observed that the modeled results agree very well with the experimental results.
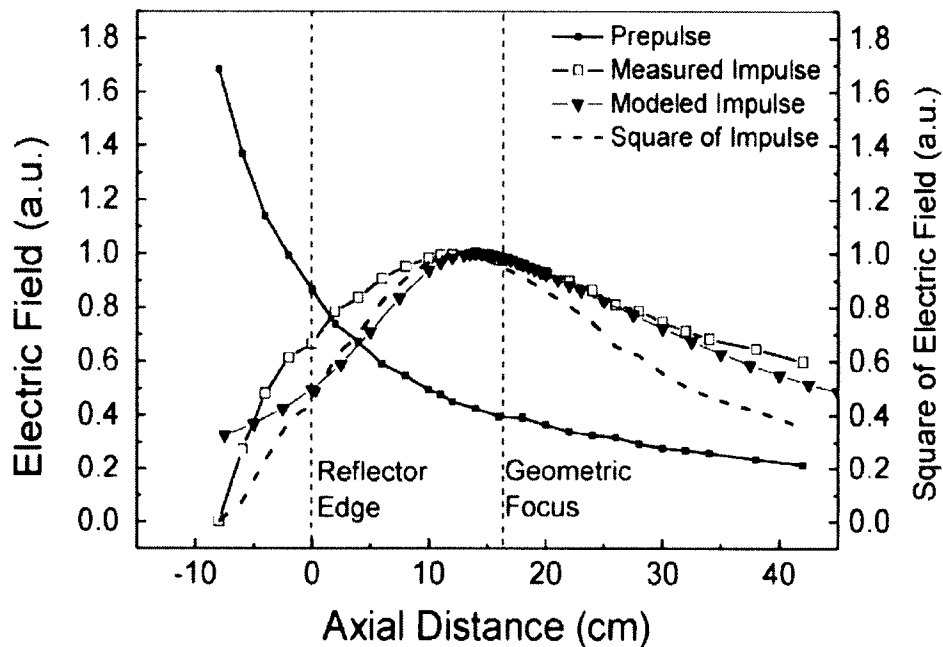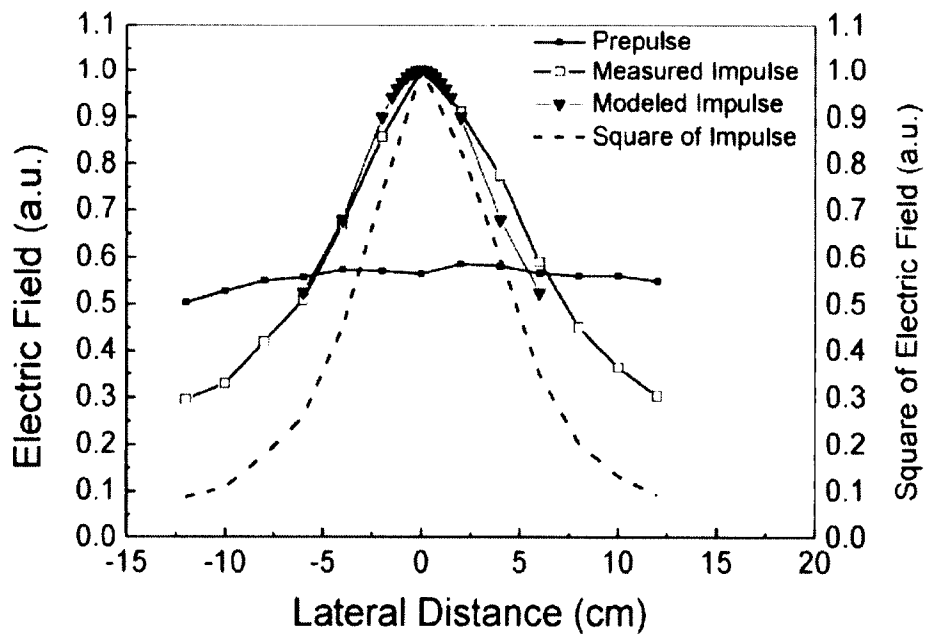
Fig. 3.8. (a) The distribution of electric field at different points along the axial direction and (b) the distribution of electric field at different points along radial direction at the focal plane (z = 16cm). In both plots, the impulse, prepulse and the square of impulse is shown.

It can be observed from Fig. 3.8 that the prepulse decays in axial z- direction and remains nearly constant in the lateral y-direction, whereas the impulse is focused in both directions. The power density of the impulse, which is proportional to the square of the electric field, is focused in both lateral and axial directions.

From Eqn. 2.31 and 2.32, with $t_z = t_\psi = t_\delta$, the focal spot size for given antenna geometry for a input pulse of 200ps rise time can be calculated analytically as,

$$|\Delta z| = 2\left[1 - \frac{z_0}{a}\right]^{-1} ct_\delta \approx 22cm$$

$$\Delta\psi = \frac{a}{b} ct_\delta \approx 7cm$$

The antenna focal spot calculated on the basis of FWHM of power density distribution has a 32cm width in axial direction and 10cm in lateral direction at the focal plane. The results show a close approximation to the analytic values calculated above.

CHAPTER IV

ANTENNA CHARACTERIZATION WITH A DIELECTRIC LENS

One problem with using antennas to deliver electromagnetic fields to the target placed at focal point concerns the dielectric properties of the target medium and its surroundings. If the wave incident on the target is in air, but the target medium has a large relative permittivity, there will be a significant reflection of the pulse, leading to a smaller field in the target medium. For practical applications, the field at the focus should be high and the focal spot size should be small. Studies [87-89] have shown that addition of a lens to better match the wave to the target helps reducing spot size, thereby increasing the field on the target.

This chapter discusses basic considerations for the design of a dielectric lens for concentrating the fields on a target, thereby increasing the fields and lowering the spot size. A dielectric lens designed with 5 layers with increasing dielectric constants from 1 to 9 is used in conjunction with the antenna to obtain better focusing and smaller spot size.

IV.I ADDITION OF A LENS TO THE PROLATE-SPHEROIDAL REFLECTOR

IV.I.I Analytic Calculations

The basic idea of adding a lens to a prolate-spheroidal IRA is illustrated in Fig. 4.1. The prolate spheroidal antenna has its focal points located at $\pm r_0$. When a high voltage pulse is launched at the first focal point at $-r_0$, it is guided by conical conductors to the prolate sphere. The irradiated wave ultimately focuses at the second focal point at r_0. For a fast rising pulse input, the field at focus consists of a delta function like impulse, which is proportional to the derivative of the input. If a lens of hemispherical shape of radius r_l centered on the second focal point r_0 is added before the second focal point as shown in Fig. 4.1, the impulse field at the focus can be maximized by an appropriate choice of its permittivity profile [87].

The basic design considerations of a dielectric lens concentrating the field on a target have been discussed in [87, 90-92]. The design is based on an exponentially tapered dielectric constant. The lens consists of different layers of dielectric materials, the dielectric constants of which are designed to give a constant wavelength to cross-section ratio with the variation of dielectric constants. Thus, the choice of the number of layers and their thickness is optimized to permit maximal transmission through these layers [91].
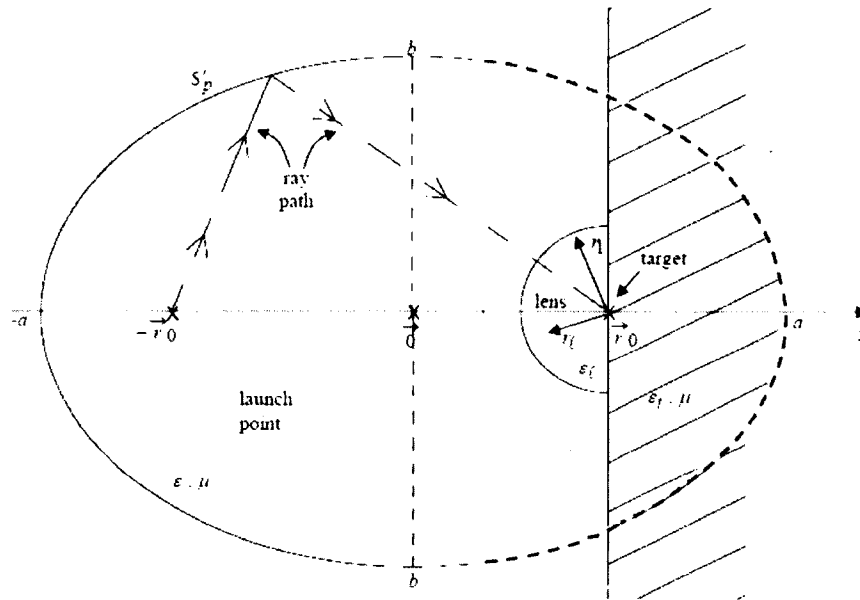
Fig. 4.1. Addition of a lens before the second focal point of a prolate spheroidal reflector. Reprinted, with permission, from [87].

For a wave travelling from one medium to another, e.g. free space to target medium, the transmission coefficient is given by,

$$T = 2\left[1 + \frac{Z_0}{Z_t}\right]^{-1} = 2\left[1 + \varepsilon_{rt}^{1/2}\right]^{-1} \tag{4.1}$$

where Z_0 and Z_t are the wave impedances of free space and the target medium, respectively, and ε_{rt} is the relative permittivity of target medium. Now, if a lens is put in front of the target medium with a graded permittivity, ε_{rl}, the permittivity progressively increases from

free space to target such that for distance $r_1 \geq r_i \geq r_2$, $\varepsilon_{rl}(r_1) = 1$ and $\varepsilon_{rl}(r_2) = \varepsilon_{rt}$. Then the wave propagating through this combination takes the same form as in a transmission line transformer, with a transmission coefficient given by,

$$T = \left[\frac{Z_0}{Z_t} \right]^{1/2} = \varepsilon_{rt}^{-1/4} \tag{4.2}$$

For a wave propagating in free space, the velocity is same as the speed of light, c. By the analysis done in the previous chapter, the impulse field at the focus, Eqn. 2.28, is inversely proportional to the velocity in the medium. But the propagation speed slows as the wave propagates into higher-permittivity media. The speed of a wave in a lens medium with a relative permittivity ε_{rl} is given by $c\varepsilon_{rl}^{-1/2}$, and hence there is an enhancement of the electric field impulse by a factor,

$$F_0 = \varepsilon_{rl}^{1/2} = \varepsilon_{rt}^{1/2} \tag{4.3}$$

Hence, the total transmission enhancement due to the addition of the lens is given by,

$$F_0 T = \varepsilon_{rt}^{1/2} \varepsilon_{rt}^{-1/4} = \varepsilon_{rt}^{1/4} \tag{4.4}$$

Moreover, the pulse width with respect to the z and ψ axes, as derived in the previous chapter (Eqn. 2.31 and 2.32), are also inversely proportional to the speed in the medium. So the focal spot size will also be enhanced by the factor of,

$$S_0 = \varepsilon_{rl}^{1/2} = \varepsilon_{rt}^{1/2} \tag{4.5}$$

IV.I.II Lens Design

The five-layer hemispherical focusing lens, as shown in Fig. 4.2, was made to specifications by TPL Inc., Albuquerque, New Mexico. The nano-composite dielectric material developed by TPL Inc. was used for the fabrication of the multilayer lens since desired dielectric

constants can be achieved [91]. The lens is a hemisphere of 30cm diameter and consists of five layers of different dielectric materials with dielectric constants varying in an exponential profile from air to the innermost layer, ε_{rmax}.

(a)

(b)
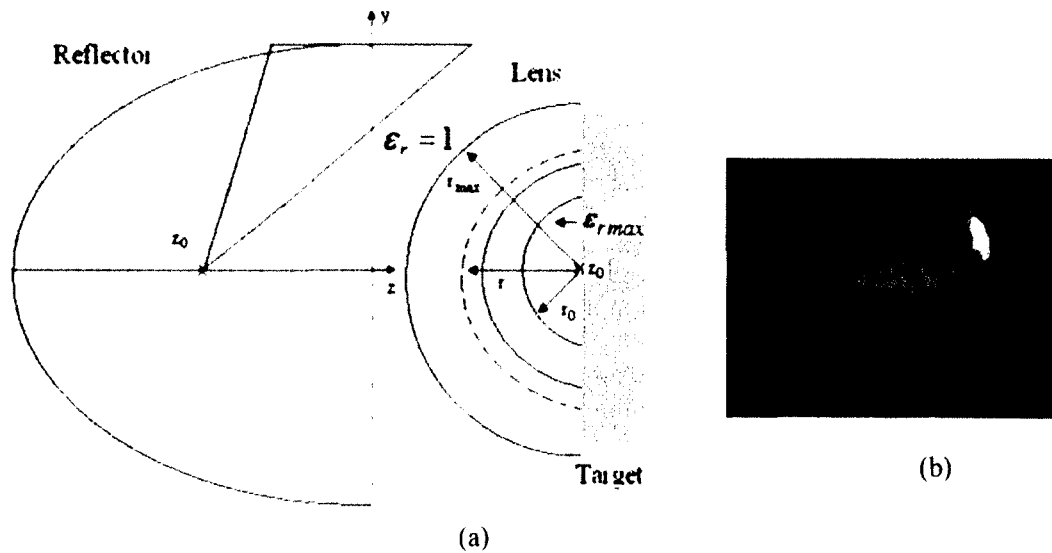
Fig. 4.2. (a) Reflector antenna in conjunction with dielectric lens showing different layers of the lens and (b) the real fabricated lens.

The table below summarizes the values of radius r of different layers and the corresponding values of ε_r of subsequent layers, where ε_{rmax} is 9 and r_{max} is 0.15m. Since ε_{rmax} is 9 and we have five layers, each layer is designed for the ratio of ε_r to be $9^{1/5} = 1.55$. As seen from the table, the ratio of dielectric constants of adjacent layers remains the same for all cases.

Layer (n)	Radius (in meters)	ε_r (n)	ε_r (n+1) /ε_r (n)
1	0.02	1.6	1.5
2	0.03	2.4	1.54
3	0.05	3.7	1.56
4	0.1	5.8	1.55
5	0.15	9.0	-

Table 4.1 ε_r values for subsequent layers of the dielectric lens [80].

The innermost layer is generally made of the same material as the medium to be targeted. So, for the lens to be matched to the target medium, $\varepsilon_{rmax} = \varepsilon_{rt}$. Due to the increase of the dielectric constant, the focal spot size can be reduced by a factor of $\varepsilon_{rmax}^{-1/2}$ at the innermost layer, and the electric field can be enhanced by a factor of $\varepsilon_{rmax}^{1/4}$ as discussed above.

IV.II EXPERIMENTAL ANALYSIS OF ANTENNA WITH DIELECTRIC LENS

IV.II.I Experimental Setup

In order to analyze the enhancement of spot size and the increase of the field at the focus due to the dielectric lens, the reflector antenna is used in conjunction with the dielectric lens, as shown in Fig. 4.3. The focal point of the dielectric lens lies at the center of the hemisphere and is at the same position as that of the reflector antenna. A metallic object of dimension (2.5cm × 1.5cm × 4.5cm) is used as a target at the focal point.
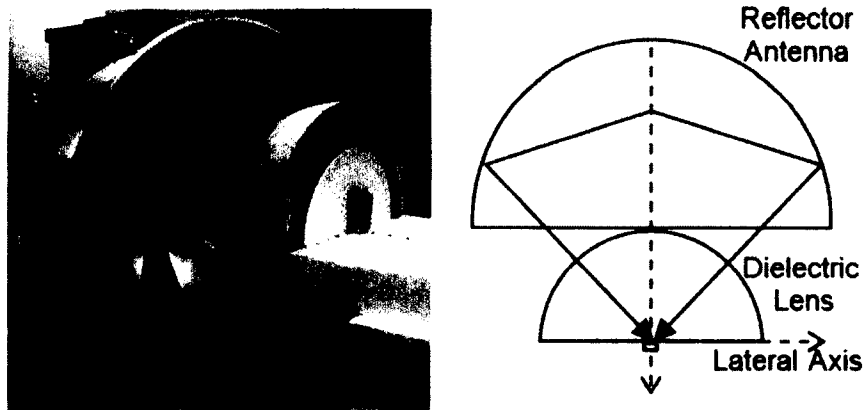
Fig. 4.3. Experimental setup with reflector antenna, dielectric lens and metal target at focal plane.

When the antenna is fed with input pulse of 200ps rise time, the electromagnetic waves travel through the conical wave launchers onto the lens and consequently to the target. The electromagnetic waves are scattered by the target and the back-scattered waves are received by the same antenna, and are recorded by an oscilloscope.

IV.II.II Results and Discussion

The received signals, when no target is present at the focal point, are the background signals, which include the reflections from other objects present in the room, like walls, tables, etc. They remain unchanged. When a target is present at the focal point, the received signals constitute a constant background signal as well as a backscattered signal from the target. The background signal is subtracted from the received signal to get the backscattered signal from target. Fig. 4.4 shows a difference of backscattered signals from the target with and without the lens.
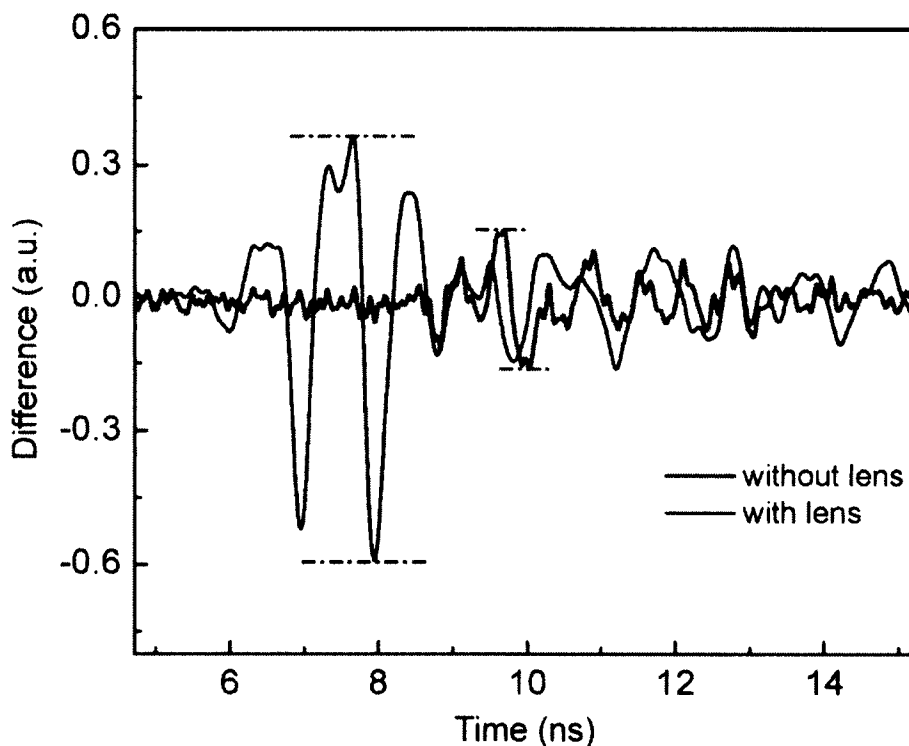
Fig. 4.4 Comparison of backscattered signal differences with and without the lens. The dashed, horizontal lines indicate the peak value of the difference.

As shown in Fig. 4.4, the lens significantly increases the difference of the scattered signal. The maximum difference (peak to peak) for the case with lens is 0.95, approximately three times greater than without the lens (0.3), which is an indication of improved sensitivity.

With the antenna and lens combination being static at a position, the target is then moved along the lateral axis, and the peak difference of backscattered signals are measured for each position. The experiment is carried out with and without the lens, and the difference of the backscattered signals with and without the lens are compared to see whether the use of a lens has improved the focusing. The resulting maximum differences for the cases with and without the lens along different lateral distances are plotted in Fig. 4.5.
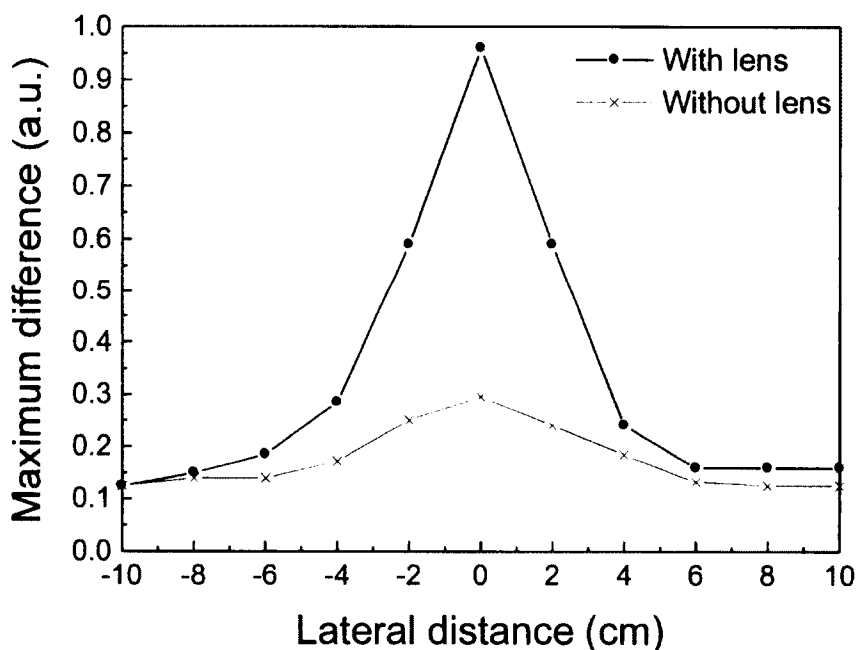
Fig. 4.5. Maximum differences of backscattered signals with and without the lens along lateral distance. A lateral distance of zero indicates the focal point.

As calculated in Chapter 3, the focal spot size along the lateral direction of the prolate spheroidal antenna is about 10-11cm. So with the application of lens, theoretically, the focal spot size at the surface of the lens should be reduced by a factor of 1/3 ($\varepsilon_{rmax}^{-1/2}$), that is, 3-4cm. As shown in Fig. 4.5, the lens significantly increases the amplitude of the scattered signal, which was about 3 times higher than that without the lens. Moreover, the FWHM (Full Width at Half Maximum) for the lens case is approximately 4cm, whereas the FWHM is approximate 6cm for

the case without the lens. Since the FWHM of the scattering difference determines the image resolution, the resolution is therefore increased by a factor of 1.5. It is noticed that although the focal spot size is reduced by a factor of 3, the resolution, i.e., the FWHM of maximum difference, is not increased accordingly by the same factor. This result suggests that the focal spot size may not be the only factor that determines the imaging resolution.

The same experiment is performed in the axial direction as well. With the antenna and lens combination being static at a position, the target is then moved along the longitudinal axis. The resulting maximum differences of backscattered signals for the cases with and without the lens along different longitudinal distances are plotted in Fig. 4.6.
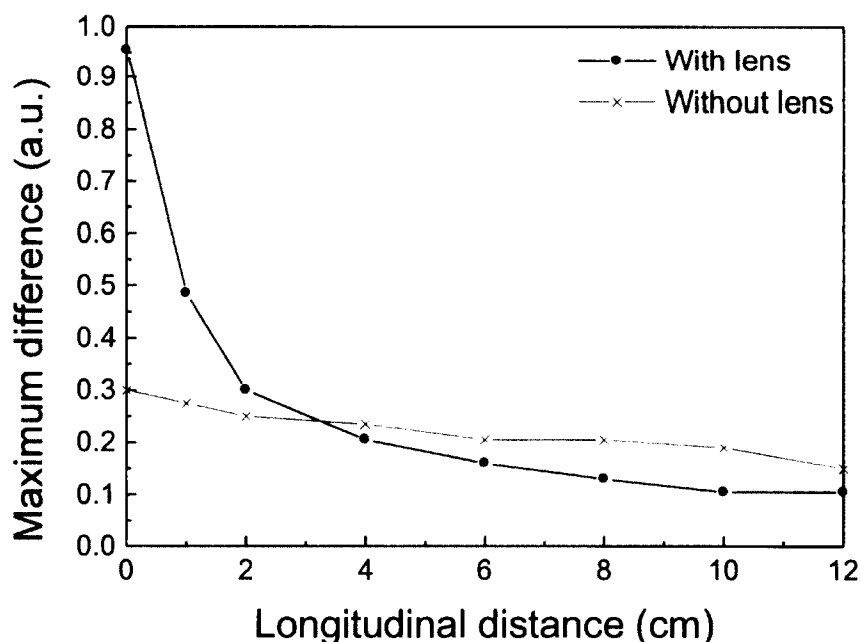
Fig. 4.6. Maximum differences of backscattered signals with and without the lens along axial/longitudinal distance. The focus is at zero distance from the planar lens surface.

Along the longitudinal distance, the difference is greatest at the focal point and is about three times higher than without the lens. The target backscattered signal is large only when the

target situates within a distance of 2cm from the focus. Beyond that, the difference decreases faster with the lens than without, as the wave exiting the lens is an evanescent wave and decreases exponentially in free space. This suggests the antenna-lens combination is good for detecting targets on the surface, which will be discussed in the next chapter.

CHAPTER V

TARGET DETECTION AND IMAGING

Microwave imaging, either with narrowband or wideband pulses, can detect the presence of abnormalities in a dielectric medium or retrieve the dielectric properties of a target through an inverse scattering technique. Wideband pulses in imaging systems have been used in subsurface probing, medical imaging and seeing through walls [93-95] because of the high resolution (centimeters in free space) and the ability to penetrate obstacles over a broad spectrum of electromagnetic radiation. Scanning a region of interest can be performed by one antenna with synthetic aperture methods [96] or by an antenna array through digital beam forming [97].

In this chapter, the capability of the antenna to detect a target in the near field as well as far field is investigated. In the first section, targets are placed at the focal point of the reflector antenna, and the sensitivity of the antenna in finding the existence of the target is explored using a small receiver. The target in this case is in free space. In the second section, the confocal setup of the antenna is explored to detect a target in the near field and to image the target. The target in this case is located at the focal point of the antenna with a lens medium. In the third case, the capability of the antenna to detect movements in the far field are explored using two identical antennas in a radar approach for through wall imaging.

V.I TARGET DETECTION IN FREE SPACE

V.I.I Experimental Setup

In order to explore whether the antenna is capable of detecting a target placed at its focal point and to explore its sensitivity, an experiment is conducted where metal targets of various sizes are placed at the antenna focal point [98]. The experimental setup used to detect the existence of a target and to explore the sensitivity is shown in Fig 5.1. Targets of different sizes are placed at the second focal point of the antenna (10cm from the antenna reflector edge). The

targets are strong scatterers: metal slabs of various sizes. The TEM horn, discussed in the previous chapter, is used as the sensor or receiver. The sensor has the same polarization as the transmitting antenna and is placed behind the target (32cm from the antenna edge) to detect the forward scattered signal. Sub-nanosecond pulses with a rise-time of 200ps generated by the pulse generator FPG5-10PM are fed to the reflector antenna. The antenna illuminates the metal targets placed at the focus, and the input pulse is scattered by the targets. The receiver collects the forward scattered signals and displays the signals to the connected oscilloscope, TDS7404 (Tektronix).
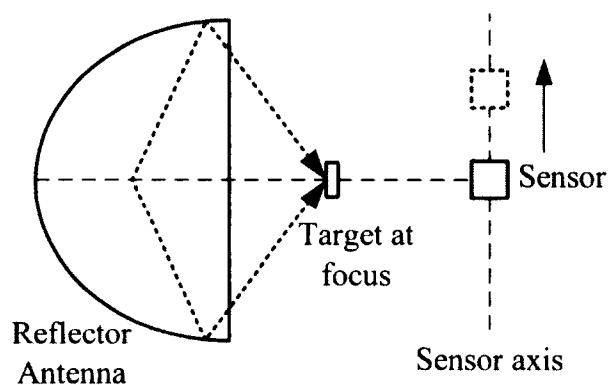
Fig. 5.1. Experimental setup for target detection in free space: the reflector antenna illuminates the target at focal point and the sensor collects the forward scattered signals. The sensor location can be varied along the sensor axis, as shown by the dotted line.

V.I.II Experimental Results

The received signal when no target is present constitutes a reference signal. When metal targets are placed at the focus, the scattered signal differs from the reference. Four different metal targets (one sphere and three slabs) in various sizes are used as targets at the focal point. The corresponding sensor signals are shown in Fig. 5.2.
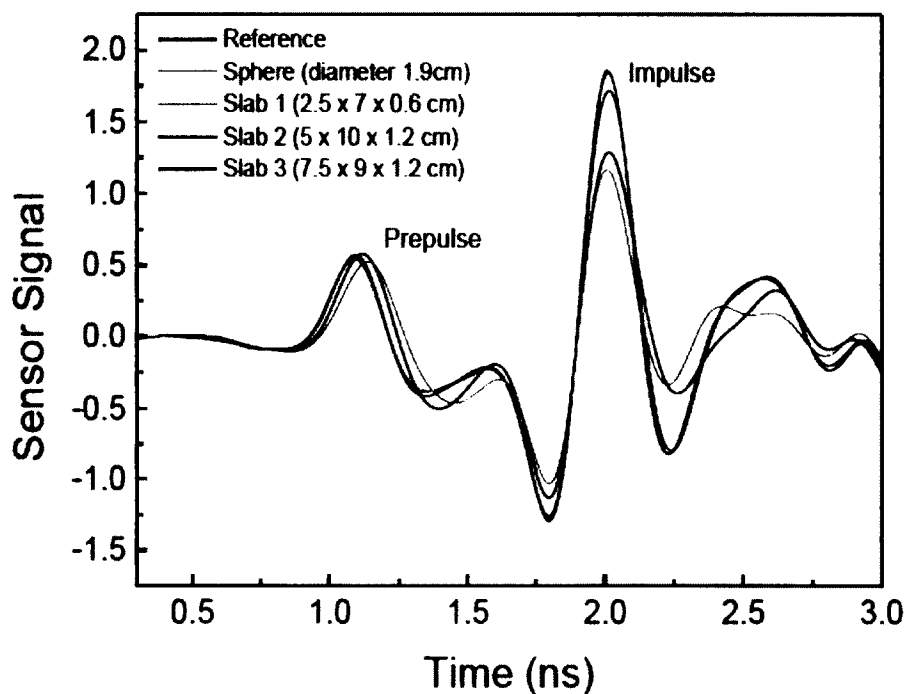
Fig. 5.2. The receiver signals for the reference (no target) and four different targets of various sizes.

From Fig. 5.2, it is seen that the signal contrast is significant for the impulse part, but negligible in the prepulse part. For impulse signals, the signals are divided into two groups. The first group contains two signals: the reference signal and the signal scattered from a sphere (diameter 1.9cm), the smallest target. These two signals are entirely overlapped and not separable, indicating the antenna-sensor system cannot resolve the sphere. The second group consists of the three signals obtained for the three slabs (2.5cm × 7cm × 0.6cm, 5cm × 10cm × 1.2cm and 7.5cm × 9cm × 1.2cm). These signals differ significantly from the reference and can be easily identified. The curve for the smallest slab has a close proximity to the first group, which indicates the limit of our system: a target with a dimension less than 7cm may not be resolvable.

Because the input pulse rise time is 200ps, the electric length of the pulse, i.e. the product of the pulse duration and the speed of light, is about 6cm. Hence, the minimum dimensions of a

target that can be detected is nearly 6cm according to the diffraction limit, and the experimental results agree with the expected value.

A focusing antenna can be used in conjunction with multiple sensors, and the signals from these sensors can be processed in the digital beamforming manner for imaging. To demonstrate the concept of multiple sensors, the same experiment is carried out with sensor locations varied along the sensor axis. The largest metallic target (5cm × 10cm × 1.2cm) is placed at the focal point of the reflector antenna and the transmitter and the target are fixed. The sensor position is varied along the sensor axis at a step of 5cm. Fig. 5.3 shows the sensor signal at different sensing location.
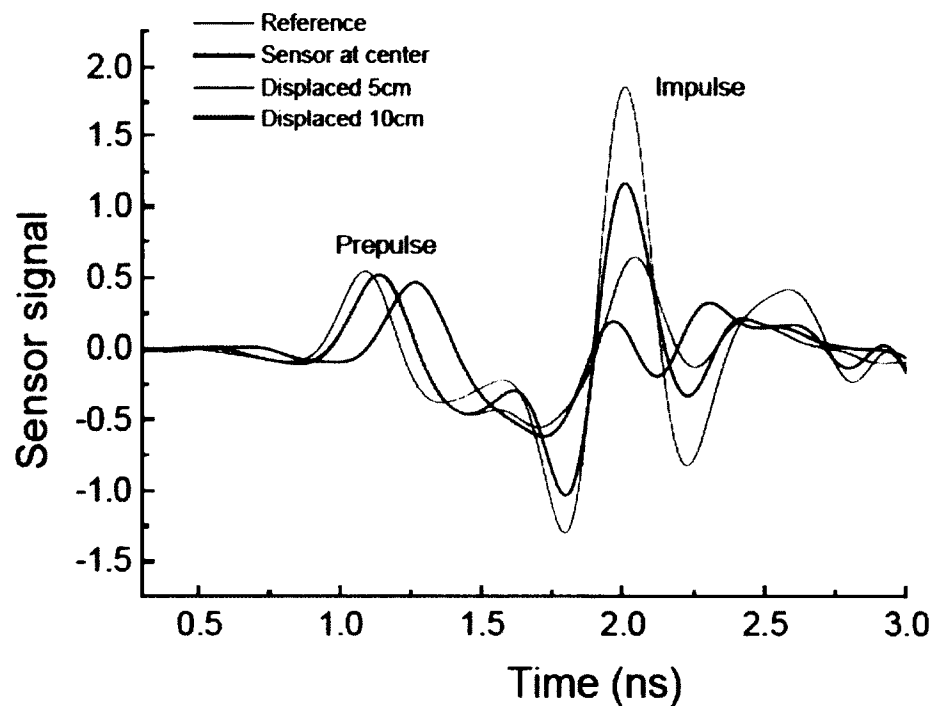
Fig. 5.3. The changes in sensor signal amplitude as the sensor is placed at different locations.

As the sensor is moved away from antenna axis, the impulse part of the signal decreases in amplitude, showing that the impulse part is sensitive to sensor's location as well. At 10cm away, the impulse part magnitude decreases to the extent that it becomes even less than the

prepulse. This is consistent with the result of Fig. 3.8b, in which the prepulse stays relatively flat while the impulse drops quickly from the axis due to the focusing nature. Although only one transmitter and one receiver is used in this experiment, this preliminary data shows the feasibility of the imaging configuration consisting of a large aperture focusing illuminator and multiple sensors. An improvement of sensitivity is seen compared to the case of "non-focusing" illuminator.

V.II CONFOCAL TARGET DETECTION IN THE NEAR FIELD

V.II.I Confocal Imaging System

When antenna radiation is focused and the target at the focus is scanned, coherent back-scattered signals, the signals with the largest amplitude, will be recorded by the same antenna. The incoherent backscattered signals from the out-of-focus background clutter, on the other hand, are shifted in time and can be separated from the target signals. This technique is referred to as confocal imaging [99]. A confocal imaging provides higher signal-to-noise ratio and signal-to-clutter ratio, and therefore stronger target detection capability than non-confocal imaging. The experimental setup for the confocal imaging system is as shown in Fig. 5.4, which consists of a pulse generator (FPG-5P, manufactured by FID GmbH, Germany), an oscilloscope (Tektronix TDS7404) and a reflector antenna. In the confocal configuration, the antenna works as both transmitter and receiver. Usually, the operation of a single antenna as transmitter and receiver requires an ultrafast transmit-receive switch to provide adequate isolation between transmit and receive ports. Here, a T-connector is used instead, which allows the pulses to be fed to the antenna and also allows the returned signal to be sent to an oscilloscope. A high power attenuator (NMFP-26B, Bath Electronics) is used to reduce the intensity of the signal, followed by two additional wideband attenuators (PE7045-20, Pasternack) on the scope.
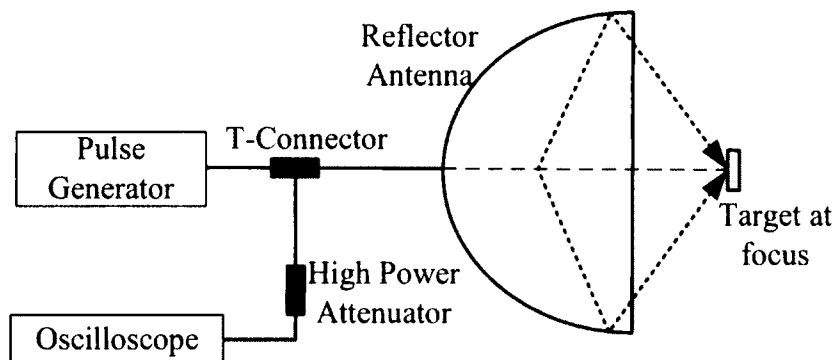
Fig. 5.4 The confocal imaging system with a near-field, impulse focusing antenna. The pulse generator delivers pulses with a rise time of approximately 200ps to the antenna, which focuses the radiation in a focal plane 16cm away from the aperture plane. The signals scattered by the target in free space are collected by the same antenna and sent to the oscilloscope for analysis.

V.II.II Experimental Results

To demonstrate the antenna's operation as a confocal transmitter and receiver, an aluminum rod (diameter: 2.54cm, length: 15.5cm) is placed at the focus and the back-scattered signals from the target are recorded. Fig. 5.5 shows the signals stored by the oscilloscope with and without the presence of the target. The signal consists of four major parts: the input pulse directly from the pulse generator, the reflections from the pulse generator, the reflected signal from the antenna balun and the backscattered signals from the target. The first three signals should be invariant and independent of the target scattering. This is confirmed by overlapping the first three signals for both cases with and without the target. The fourth part of the signal varies as a result of the introduction of the target and contains backscattered signals from the target. A more detailed analysis of the signals is not necessary since we are only interested in examining the changes of the signals in the presence of the target versus without the target. The appearance of the signal changes indicates the presence of a target at the focal point. Once the time window of this change is identified, the oscilloscope is set in a delayed mode so that this particular time window is enlarged by setting a lower voltage scale and shorter time scale. The inserted figure in

Fig. 5.5 shows a significant difference between the signals with and without the presence of the target.
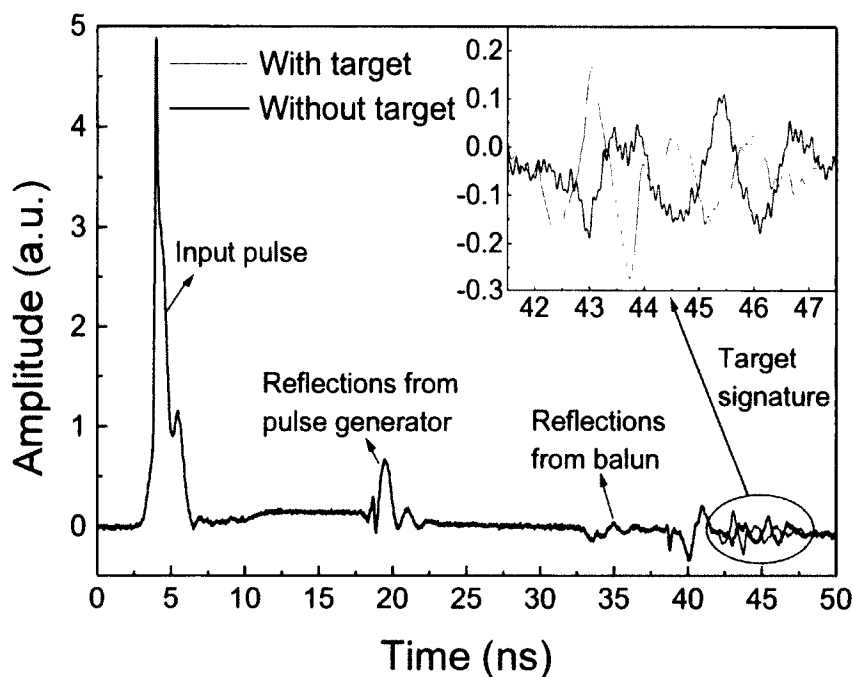
Fig. 5.5 The recorded signal on the real-time oscilloscope. The signals consist of four parts: 1) the input pulse from the pulse generator (14%-92% risetime, 200ps, FWHM: ~600ps) , 2) the reflection from the pulse generator because of the T-connector, 3) the reflected signal from the antenna balun and 4) the back-scattered signals from the target at the focus.

V.II.III Antenna Polarization

In addition to being spatially confined near the focus, the wave is linearly polarized and can be adjusted either in the vertical or horizontal direction by rotating the antenna. For linear targets, e.g., a metallic rod (diameter: 2.54cm, length: 15.5cm), the back-scattered signal is at its maximum when the target is co-polarized (Fig. 5.6a). For linear targets that are cross-polarized, the antenna rejects the backscattered signals (Fig. 5.6b), so the target is undetectable to the imaging system. This property allows us to selectively scan the targets by examining the intensity of the target return. The orientation of the antenna can be varied until a maximum backscattered signal is observed as the antenna polarization is aligned with the target orientation.
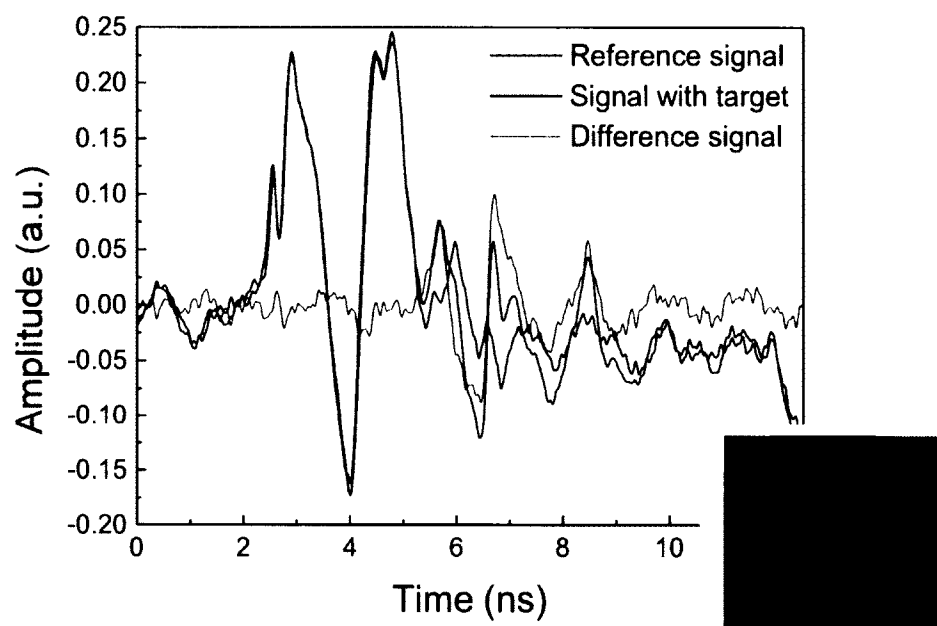
(a)
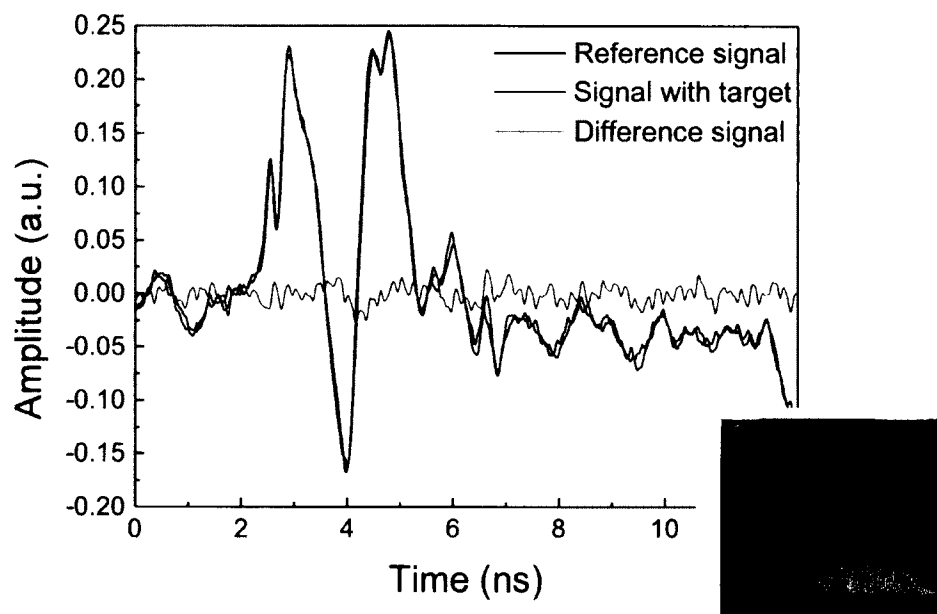
(b)

Fig. 5.6 Received signal for different orientations of a target when the antenna is vertically polarized: (a) the rod is placed at the focus vertically (co-polarized), and (b) the rod is placed at the focus horizontally (cross-polarized).

V.II.IV Confocal Imaging in the Near Field with Dielectric Lens

For the imaging in near field, the antenna in conjunction with the lens is used as shown in Fig. 4.3. Two targets of equal dimensions (2.5cm × 1.5cm × 4.5cm) are placed at the focus. The two objects are scanned by the antenna-with-lens system horizontally for different spacing, and the backscattered signals are recorded for each position and spacing used. The signals are used to construct a 2-D image by assigning pixel values according to the magnitude of received signals. Fig. 5.7 shows the image constructed with two objects with a spacing of 3.5cm and 5.5cm. The two targets are irresolvable in the lateral direction when the spacing is shorter than 3.5cm. However, the imaging system is able to distinguish targets for a spacing of 5.5cm, so the resolution can be estimated as 4cm. This resolution is determined by the maximum difference shown in Fig. 4.5 and the color scale used in Fig. 5.7. The color scale is -0.6 to 0.6 corresponding to a FWHM in Fig. 4.5 which is approximately 4cm.

(a)   (b)
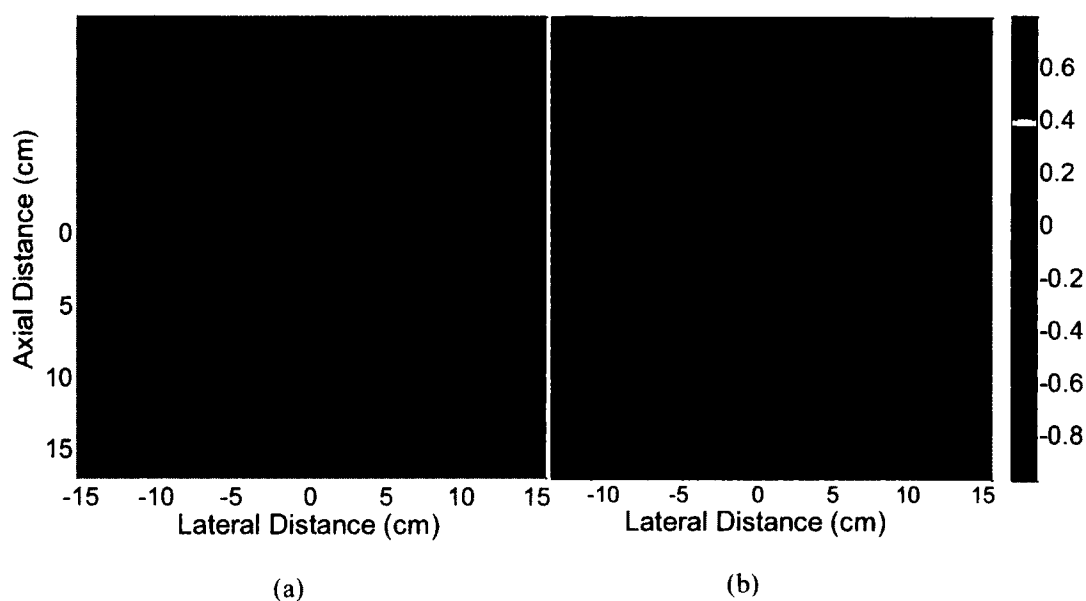
Fig. 5.7. Images of two identical metallic objects (2.5cm × 1.5cm × 4.5cm) that are separated by (a) 3.5cm and (b) 5.5cm. The two objects can be resolved at a lateral spacing of 5.5cm but are irresolvable for 3.5cm.

V.III DETECTION OF A MOVING TARGET WITH TWO ANTENNAS

V.III.I Experimental Setup

To further analyze the capability of the antenna in target detection and imaging, the antennas are investigated for target detection in the far-field in a radar configuration. Two identical impulse radiating antennas are used as a transmitter-receiver pair to detect human movements behind a wall. In this case, the focusing ability of the antenna is not as useful as in the near field, but may be utilized to suppress the wall clutter provided that the focal point is in the wall. More radiation can go through the wall at the Brewster angle, which allows the detection of targets in the wider area behind wall. The experimental setup is shown in Fig. 5.8, where both the transmitter and the receiver are stationary facing a wall. The transmitting antenna is fed by the sub-nanosecond pulse with a rise time of 200ps. The pulse is generated by a sub-nanosecond generator, FPG5-10PM, manufactured by FID. The oscilloscope (4GHz bandwidth, Tektronix TDS7404) and computer communicate through a General Purpose Interface Bus (Agilent 82357B USB/GPIB Interface).
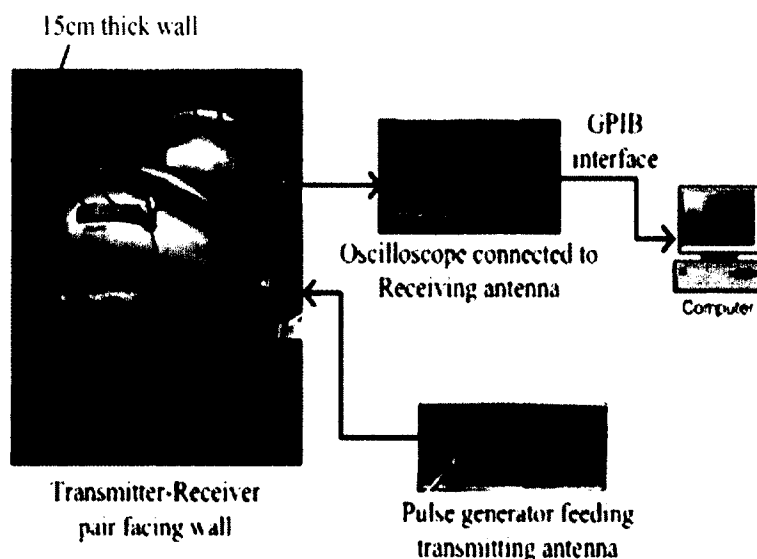
Fig. 5.8 Experimental Setup for moving target detection.

V.III.II Experimental Results

A moving target is detected by using the Doppler Effect. The backscattered signals are recorded, which include the signal from the moving target as well as the unwanted signals (clutters) due to the reflection on the wall, antenna coupling, and background objects. Fig. 5.9 shows the back-scattered signal at a particular moment from a human movement. Fig. 5.9a shows the unprocessed signal where the feature of the target is not visible. The target signature is masked by the presence of heavy clutters due to the reflections from wall, sidewalls, furniture, other objects in the room and the coupling between the transmitter and the receiver. Because the clutters are time-invariant, they are discarded by subtracting two successive signals in the recording. The target signature then becomes observable in this case. Fig. 5.9b shows the signal after subtraction of the background scattering using a Difference Filter [100].
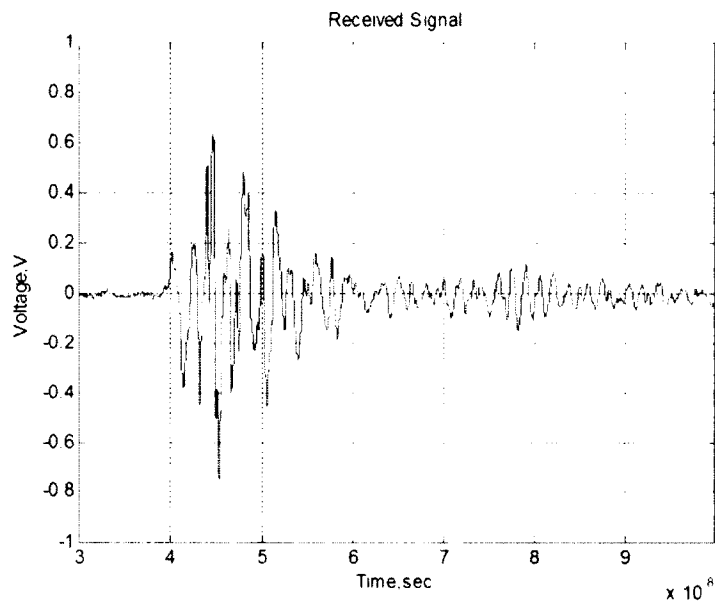
(a)
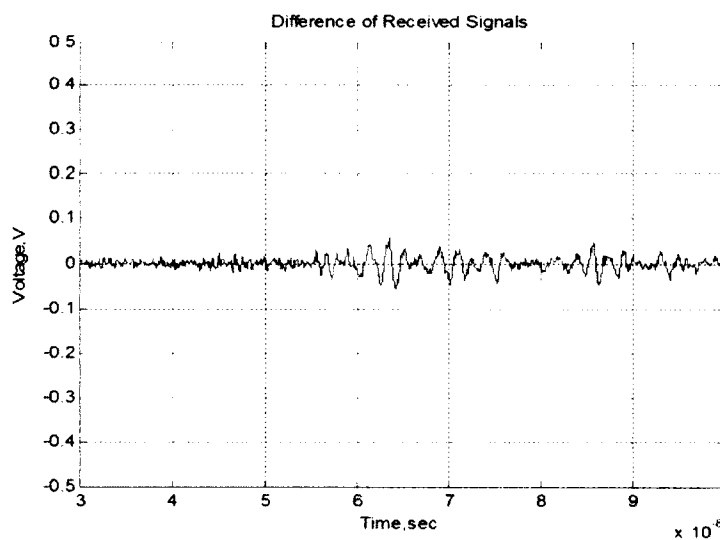
(b)

Fig. 5.9 Received waveforms: (a) a regular unprocessed waveform where the target signature is masked by the presence of heavy clutters, and (b) a waveform after background compensation shows observable target signature.

The radar system can track the trace of the moving target behind the wall by calculating the real-time changes of the backscattering through subtracting the consecutive signals as shown in Fig. 5.9b. Each subtracted signal forms an A-scan data, and can be arranged into a matrix

format. The data can then converted to 2-D images by assigning pixel values according to the amplitude of the processed signal so that the moving target can be traced in real time. Fig. 5.10a shows the resulting image when a human walks straight to the wall 10m away. The black line indicates the position of the wall. Fig. 5.10b shows the image when a human walks in parallel to the wall for a distance of 7m.

(a)

(b)
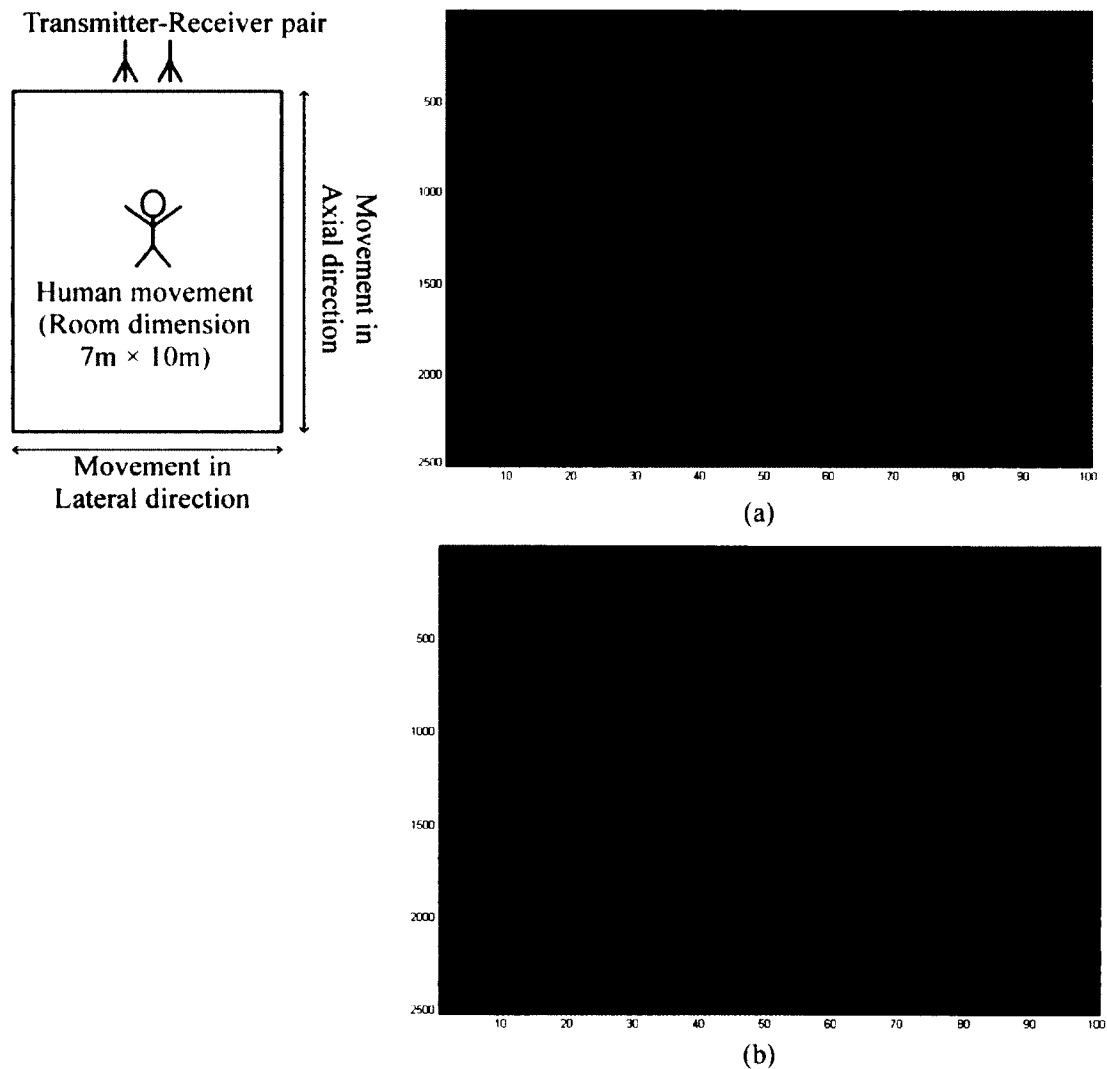
Fig. 5.10 Room setup and resulting 2-D image for (a) axial movement and (b) lateral movement.

The results show the radar system is sensitive to the human movements in an area of 10m × 7m behind the wall. The radar has the advantage of large-area coverage even when the antennas

remain stationary, owing to the large antenna aperture. Whereas the antennas are kept still and the focal points of the transmitter and receiver are inside the wall, the target detection range appears not to be dependent on the focal spot. Rather, the antenna polarization is kept in the vertical direction to maximize the return signal from the standing human. The aperture diameter (0.5m) of the receiving antenna is also instrumental to the wide-angle detection. It is noted that the moving target trace (Fig. 5.10) can be improved and mapped to the exact target position by migration techniques [101]. For stationary targets which have significant contrast in dielectric properties to the surroundings, the antennas need to be mechanically shifted to scan the whole region of interest.

CHAPTER VI

SIMULATION STUDY OF FOCUSING ELECTROMAGNETIC FIELDS IN A BIOLOGICAL TISSUE

After the characterization of the antenna and its study in target detection and imaging in the previous chapters, the single fixed-focus prolate-spheroidal antenna is further investigated for delivering sub-nanosecond electrical pulses at desired locations in biological tissues. The interaction of biological models and electromagnetic fields is of great importance for medical safety, diagnostics, therapeutic applications, and instrumentation. Specifically, studies are still being conducted in implanted medical devices, cell phone safety, and medical applications like hyperthermia and thermal ablation of cancer tissues, as well as medical imaging. For all of these scenarios, it is important to be able to simulate the effects of electromagnetic fields on biological targets.

The antenna and the biological tissues are modeled using 3-D electromagnetic simulation software, CST Microwave Studio®, and the simulation results are presented in this chapter. With these simulation studies, answers to several questions are expected, like can a focal spot be formed in the tissue? If so, how deep is the focal spot formed at and how large is the focal spot size?

VI.I 3D SIMULATION SETUP

VI.I.I Model Configuration

The basic configuration model in this case consists of a reflector antenna and a target at the focus shown in Fig. 6.1. The geometry of the simulated antenna is based on the existing reflector antenna of Fig. 3.1, where the antenna has a prolate spheroidal reflector fed by a transverse electromagnetic conical transmission line starting from the first focus as a wave launcher.
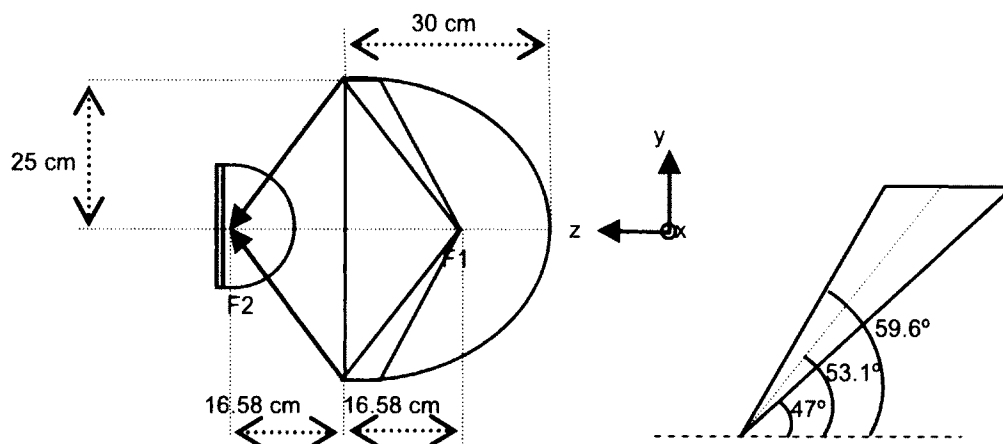
Fig. 6.1 Detailed geometry of modeled impulse antenna sending sub-nanosecond pulses to a hemispherical target.

The tissue target is modeled as a hemisphere of radius 6cm with dielectric constant (ε_r) in the order of 45 (for muscle tissue) and 5 (for fat tissue). Such shape is chosen because the spherically incoming waves from the reflector antenna have the same phase along the circumference of the tissue, which results in a maximum field at the second focus for the same optical path. To prevent the wave diffracted at the edge of the tissue from reaching the focus as creeping wave, a very lossy cylindrical base is added to the hemispherical tissue. Such treatment allows only the incident wave on the hemisphere to enter.
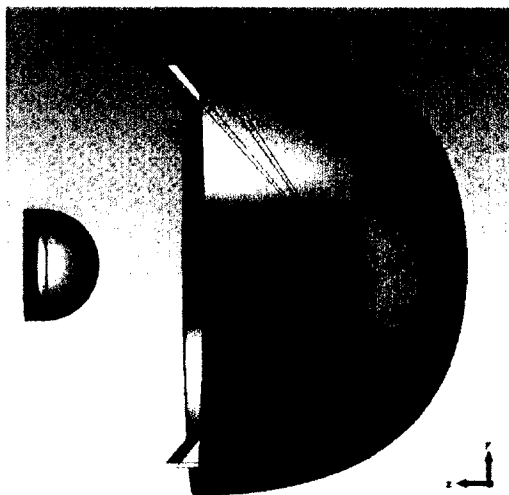
Fig. 6.2 Modeled impulse antenna and hemispherical target in CST Microwave Studio.

VI.I.II Feed Signal

Once the geometry is generated, a signal can be fed to the first focal point where a voltage port is placed. In the experimental studies of the antenna, the pulses have a rise time of 200ps and the impulse is determined by the time derivative of the pulse. In order to model closely to real scenario, a Gaussian pulse signal with a pulse width of 200ps as shown in Fig. 3.6 is used as an input. The frequency range is set to 0-5GHz.

VI.II SIMULATION RESULTS

VI.II.I Field Measurements

The electromagnetic waves emitted from the elliptical reflector are spherical waves, converging at the second geometric focus of the reflector. The phases of the incoming spherical waves on the circumference of the target are identical. Because the electric fields of the converging spherical waves are parallel to the surface of the hemispherical tissue, the transmittance into the tissue is optimum [25]. For a relative permittivity of $\varepsilon_r = 9$ and a conductivity of the target of $\sigma = 0$, the electric field along the z-axis from the tissue surface to the geometric focus of the reflector is measured by inserting probes at every 1cm distance. The electric pulse at the focal point is shown in Fig. 6.3. The pulse consists of a prepulse and an impulse. The prepulse reaches the second focal point at an approximate time, $t = 27.16/30 + 6*\sqrt{9}/30 = 1.505$ns. The pulse reflected from the prolate-spheroidal reflector surface converges at the second focal point. This constitutes the impulse part of the wave at the focal point and occurs at approximately $t = 54/30 + 6*\sqrt{9}/30 = 2.4$ns. The shape of the impulse is close to the time derivative of the Gaussian wave form [1]. The electric field component that contributes mostly to the electric field at the focal point is the y-component. The amplitudes in x and z direction are negligible.
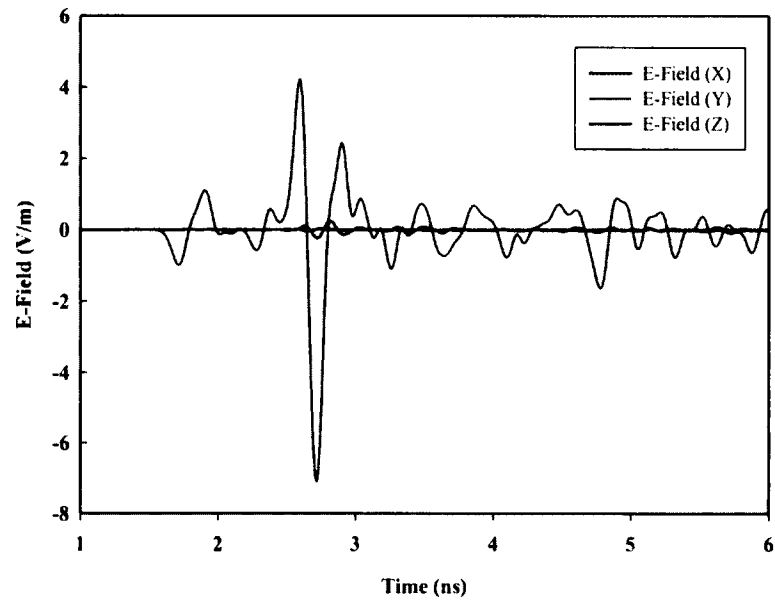
Fig. 6.3. Electric field at focus: the y-component of field is dominant among the electric fields in all directions.

The electric field distribution in absolute value is shown in Fig. 6.4 at different time instants. The electric field guided by the conical wave guide is inhomogeneous (t = 0.4ns). The prepulse can be easily identified at t = 1ns, as it is diverging from the launching point. At t = 2.3ns, the impulse enters the tissue resulting in reflection near the surface. The field reaches a maximum value at t = 2.9ns inside the hemispherical tissue at the focal point.
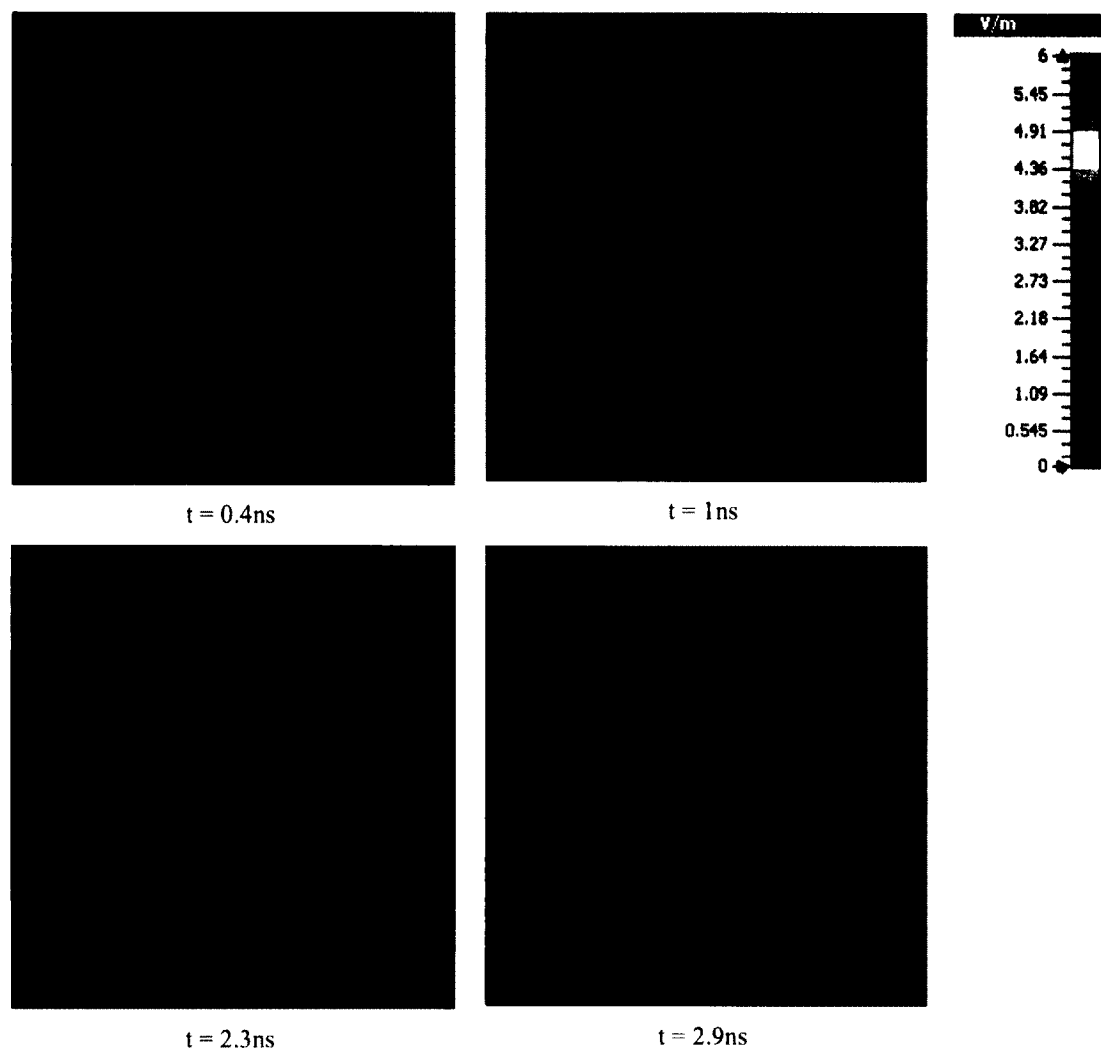
Fig. 6.4. Propagation of electromagnetic waves from the antenna to a biological target at different instants of time; the biological target has a relative permittivity of 9 and a conductivity of 0, using a clamp to range 0 to 6V/m.

At t = 2.9ns inside the hemispherical tissue, different cut plane views can be obtained and are shown in Fig. 6.5. The cut plane of x = 0 gives a side view, the plane y = 0 gives the top view and the cut plane of z = 46.1cm gives the back view at the focal point.

| Cutting plane, x = 0 | Cutting plane, y = 0 | Cutting plane, z = 46.1cm |
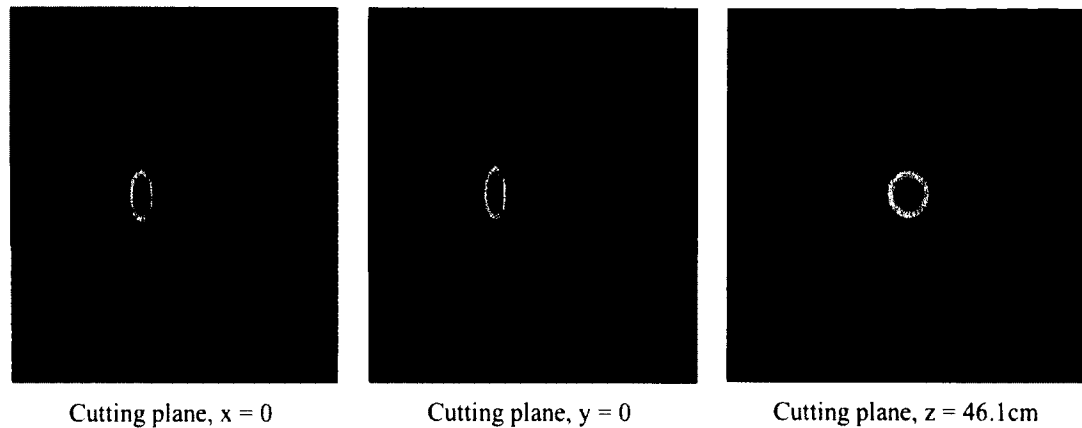
Fig. 6.5 Focusing of EM waves inside biological target of relative permittivity 9 and conductivity 0, at t = 2.9ns, three different cut-plane views that show the focusing of electromagnetic energy in the x-plane, y-plane and the focal plane along z-axis. The plot uses a clamp of 0 to 6V/m.

VI.II.II Effect of Material Properties

In order to study the effect of varying material medium on the electric field distribution, the simulation is carried out for varying conductivities from 0 to 0.5 S/m while the relative permittivity of the tissue is fixed to 9. Zero conductivity corresponds to a lossless tissue. The tissue conductivity near 0.5 S/m is close to that of breast tissue [102]. The probes placed on the z-axis from air-tissue interface to focal point of reflector antenna measure the E-fields and the results are shown in Fig. 6.6. The electric field for lossless tissue increases from tissue surface towards the focal point, but increasing tissue attenuation significantly decreases the E-field as the wave makes its way to the focal point. In the case of conductivity 0.5S/m, the electric field at focal point becomes even less than that at the air-tissue interface.
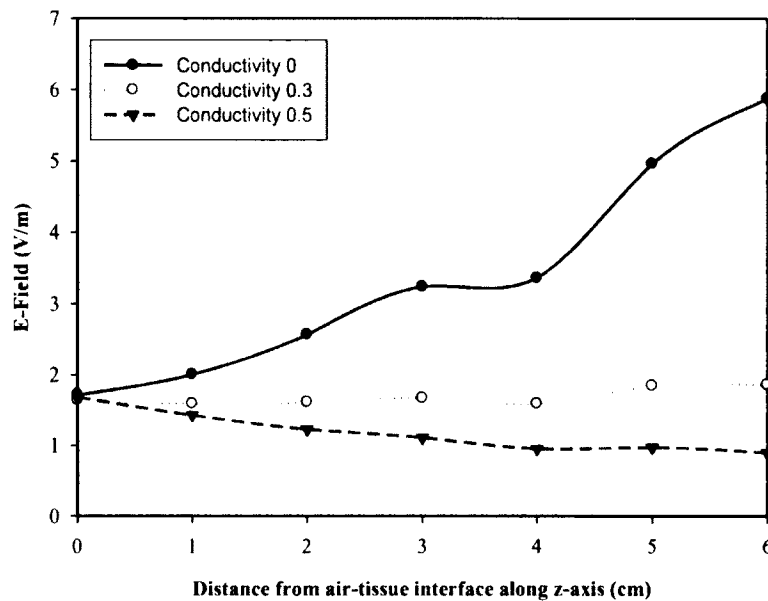
Fig. 6.6. Electric field distribution along z-axis for different tissue conductivities. Relative permittivity of the tissue is fixed at 9. z = 0 indicates the air-tissue interface whereas z = 6cm indicates geometrical focus.

Tissue conductivity usually affects the amplitude of the electric field, and tissue permittivity determines how large an electric pulse spreads in the space. To further study the effect of permittivity on the electric field distribution, it is varied from 9 to 70 for different conductivities. The electric fields at different points of the tissue along z-axis are shown in Fig. 6.7.
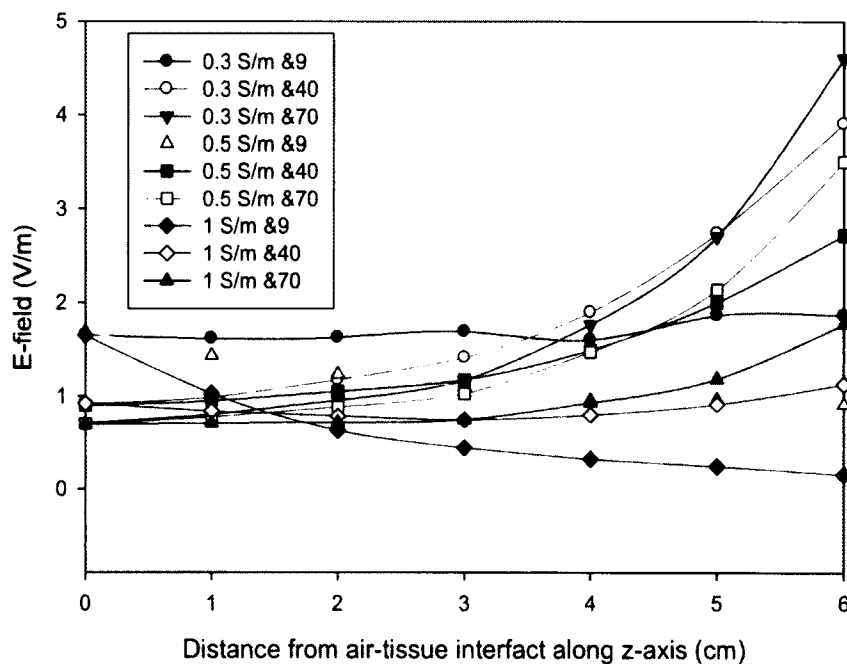
Fig. 6.7. Electric field distribution along the z-axis for different tissue conductivities and relative permittivities, z = 0 indicates the air-tissue interface, whereas z = 6cm indicates a geometrical focus.

For a relative tissue permittivity of 9, the field has its maximum at the focal point for a conductivity of 0.3S/m. But as conductivity increases, the maximum field is located at the surface and decreases as it travels into the tissue. However, the decreasing of E-field along z-axis is reversed when the relative permittivity of tissue is increased from 9 to 70. Hence, the focusing effect is achievable in tissue with higher permittivity. It is important to note that as the wave goes deeper into the tissue, tissue conductivities, and consequently strong absorption by the tissues, play an important role in the focusing characteristics of the antenna into the tissue.

Further, to characterize the field distribution along different radial directions, the field at different angles θ is measured by inserting probes at 0, ±15, ±30, ±45, ±60, ±75 and ±90 degrees at a radial distance of 1cm in step from the surface to inside of the tissue. The resulting electric

field distribution for tissue with a relative permittivity of 9 and a conductivity of 0.5S/m is shown

in Fig. 6.8.
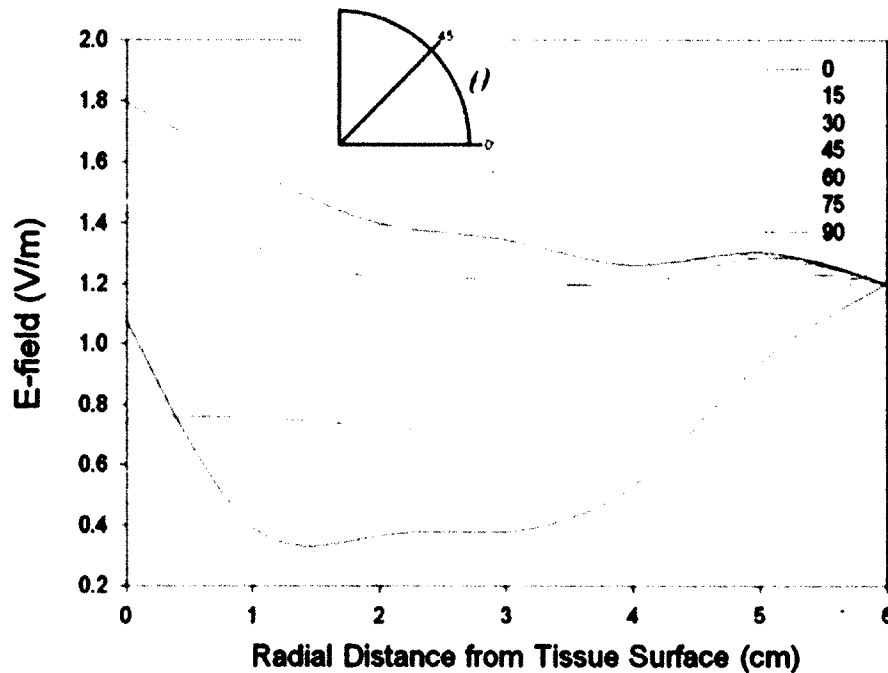
Fig. 6.8. Electric field distribution along radial direction for different azimuthal angles, θ. The tissue has a relative permittivity of 9 and conductivity of 0.5S/m.

As seen in Fig. 6.8, for larger azimuthal angles ($\theta \geq 30°$), the waves in the tissue experience a decrease in amplitude in the first few centimeters, but increase eventually towards the focal point. This difference in losses along different radial path suggests that if the fields near or on the z-axis could be attenuated, and only the fields at higher azimuthal angles are allowed to pass through the tissue without loss, a narrower focal spot might be obtained inside the tissue.

VI.II.III Effect of Adding a Dielectric Lens

In the previous chapter, it has been shown that the electrical energy density at the focal spot can be increased by reducing the reflections due to an abrupt change of tissue permittivity at the air-tissue interface. This can be done by employing a multilayer dielectric lens that matches the impedance from air to the biological tissue. Hence, a dielectric lens consisting of five layers is

used in conjunction with the reflector antenna for delivering pulses to the hemispherical tissue (Fig. 6.9). The last layer of the lens is the biological tissue with radius of 6cm. The dielectric constants of these five layers from the outermost to the innermost are 1.6, 2.4, 3.7, 5.8, and 9.0, respectively. The biological tissue (i.e. the innermost layer) has the same dielectric constant as the fifth layer.
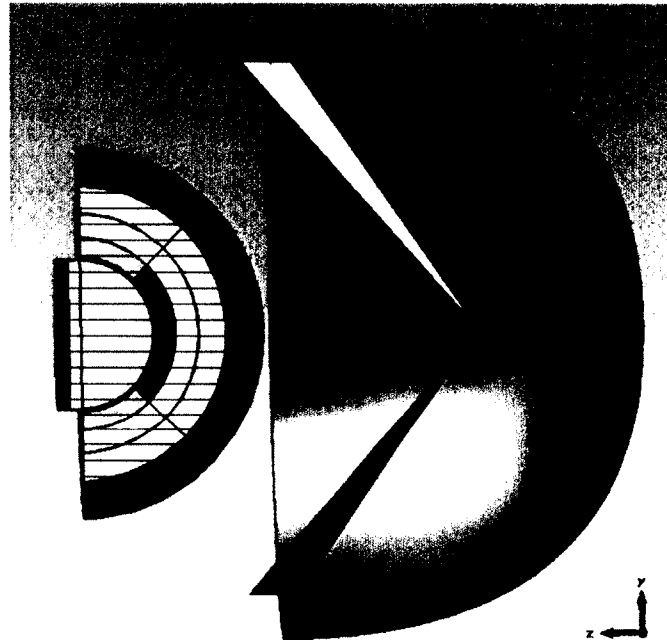
Fig. 6.9. The impulse radiating antenna and a hemispherical target embedded in a dielectric lens in the CST Microwave Studio. The cut-plane view shows the layers of the dielectric lens.

The reflector antenna with lens is simulated for a tissue with a relative permittivity of 9 and a conductivity of 0. The focusing of electromagnetic fields into the biological target is observed at t = 3.1ns, as shown in Fig. 6.10. Hence, the addition of the lens creates a delay compared with when the reflector is without a lens. Compared to the results without lens in section VI.II.I, the electric field value at the focal point is also found to be increased by a factor of 1.2.
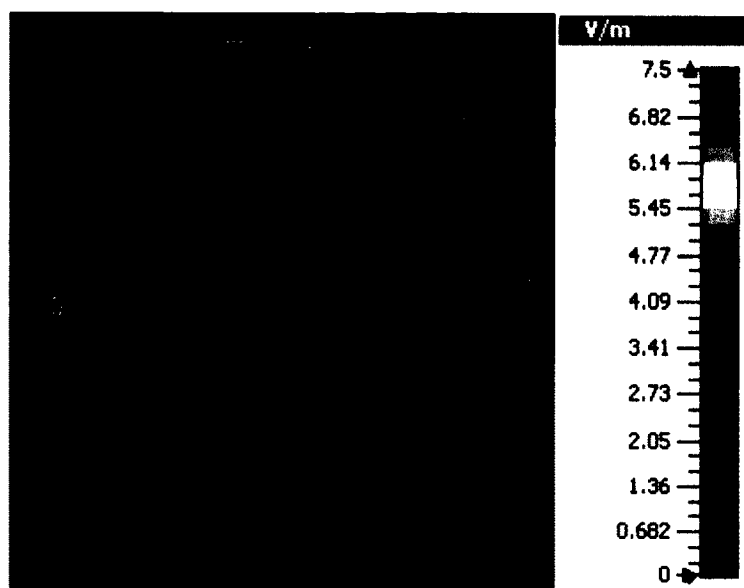
Fig. 6.10 Focusing of EM waves inside a biological target having a relative permittivity of 9 and a conductivity of 0, at t = 3.1ns. The plot uses a clamp of 0 to 7.5V/m.

In the next step, the biological tissue is made lossy by assigning a conductivity of 0.5S/m while its relative permittivity is unchanged (9). Fig. 6.11 shows the field distribution of impulse along different azimuth angles and radial distances. Compared to Fig. 6.8, it can be concluded that the addition of a lens does not help much for high conductivity material, as the magnitude of the electric field at the focal point remains about the same. The electric field decreases steadily as the distance increases from the surface. For paths of larger angles, there is an increase as the distance increases. The electric field distribution in the hemispherical tissue in this case can be schematically depicted by a pie shape.
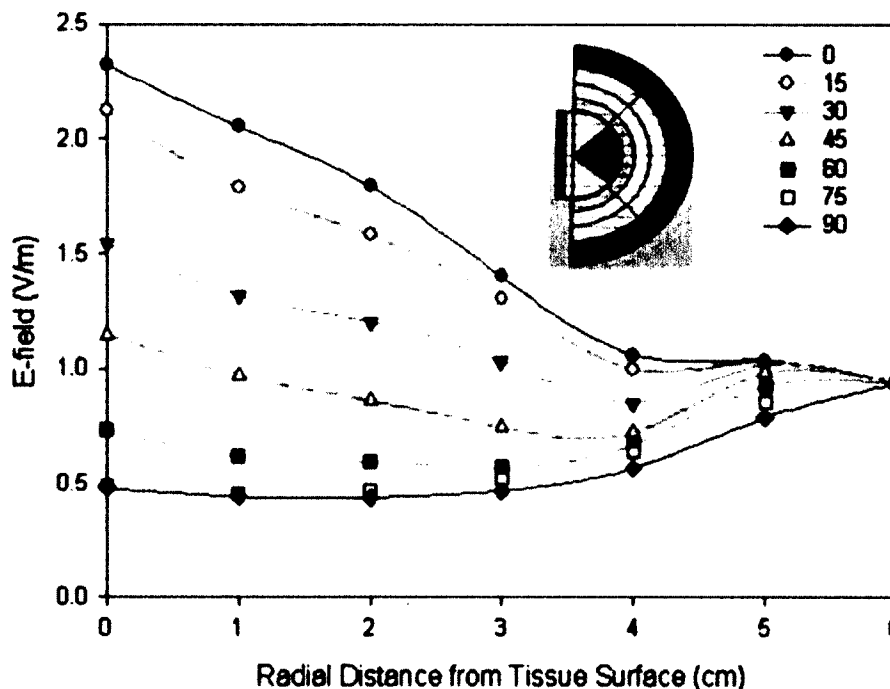
Fig. 6.11. Electric field distribution along radial direction for different azimuthal angles, θ when a dielectric lens is added to the reflector antenna. The tissue has a relative permittivity of 9 and a conductivity of 0.5S/m.

VI.II.IV Effect of Adding Losses to a Dielectric Lens

In the previous section, as depicted in Fig. 6.8, it was noted that the waves traveling in the radial direction with larger angles decrease in the tissue for the first few centimeters and eventually increase as they approach the focal point. This suggests that if the electromagnetic waves travelling at lower angles could be suppressed, the electrical field distribution may be modified and a local maximum can be formed. In order to achieve such selective attenuation, the lens properties are modified in such a way that it would allow the waves travelling at wider angles to penetrate easily. The innermost layer and the second to last layer of the lens are made lossy for angles below 45°, which means, for azimuth angles between +45° and -45°, it has a finite conductivity (1 or 2S/m). The dielectric constants of the materials are kept the same as in the previous lens design.

With this design, the field distribution throughout the tissue changes. Due to the strong attenuation of the lossy layer, the electric field intensity on the z-axis becomes smaller on the surface, but increases at a depth of 6cm. Meanwhile, the radial distributions along other radial paths near the z-axis also show a slight increase in the deeper area, except on the surface of the tissue at angles >60°. The field distribution is schematically shown in Fig. 6.12. A comparison of Fig. 6.11 and 6.12 shows a localized focus may be formed in the deep region of the tissue. This change in distribution is made at the cost of the reduction of the absolute field intensity at the targeted region and two extra "hot spots" near the surface.
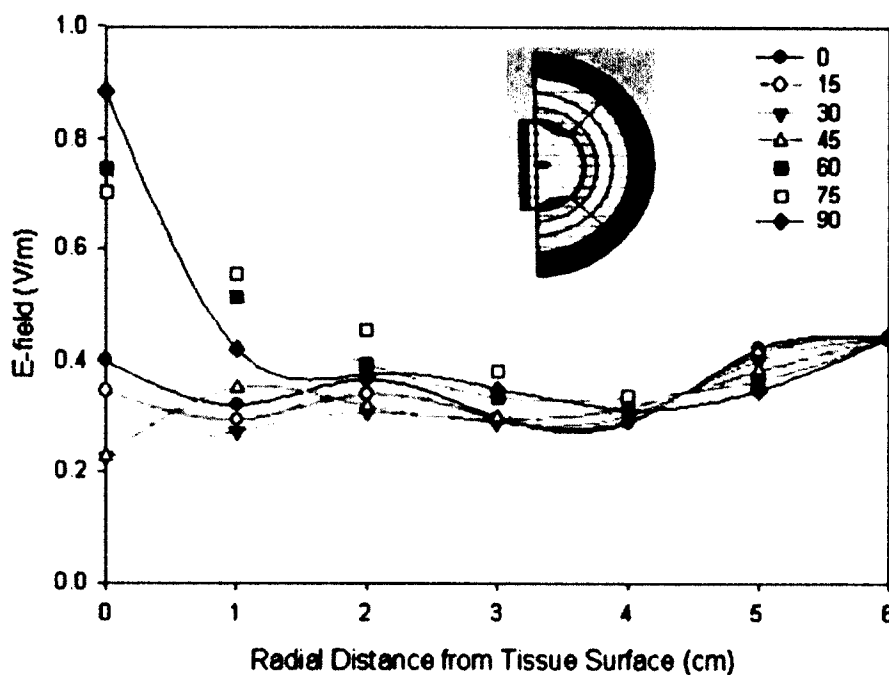
Fig. 6.12. Electric field distribution along radial direction for different azimuthal angles when a lossy lens is added to the reflector antenna. The tissue has a relative permittivity of 9 and a conductivity of 0.5S/m.

VI.II.V Increasing the Antenna Reflector Area

So far, the analysis of the reflector antenna adapted the minor axis plane as the aperture. A different approach was discussed [103] where a prolate spheroidal reflector used the major axis plane as the aperture. This antenna reflector reflects not only the impulse, but also the prepulse, so the target at the second focal point experiences a higher field. The study shows that better power focusing characteristics are obtained when the feed structure becomes less directive or the size of the aperture becomes large. Moreover, the discussion in Chapter 2 also shows that a large focal distance to minor axis ratio (z_0/a) and correspondingly, a small b/a ratio is preferable for better focusing. So, a fat, shallow antenna and a large reflection area should produce a high impulse amplitude at the focus.

In an effort to increase the field at the focal point, a new antenna is simulated with the biological target. The simulated antenna geometry is shown in Fig. 6.13, where the reflector is designed so that the aperture contains the major axis, giving a larger reflector area. A conical plate and a ground plane are used at the first focal point, which is fed by the Gaussian pulse of rise time 200ps (Fig. 3.6). The biological tissue target is placed at the second focal point. The simulation is set for the frequency range of 0-5GHz.
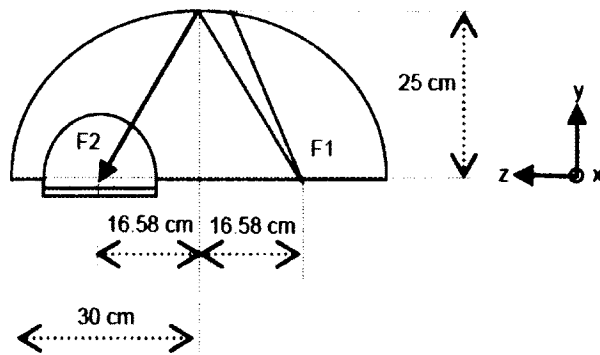
(a)

(b)

Fig. 6.13. (a) Antenna geometry with aperture along the line joining foci, and (b) the corresponding simulation model in CST MW Studio.

The probes placed inside the biological target allow the measurement of electric field distribution. The electric field components at the focal point is shown in Fig. 6.14. In the previous case, where the aperture contains the minor axis, the inherent symmetry in the structure results in cancellation of E-field components (x- and z-), and it is seen that the y-component of the field is dominant, and x and z components are negligible. However, in this case, only the x-component of the electric field is negligible at the focal point, while both the y- and z-components contribute to the field at focus, and a higher overall field is expected.
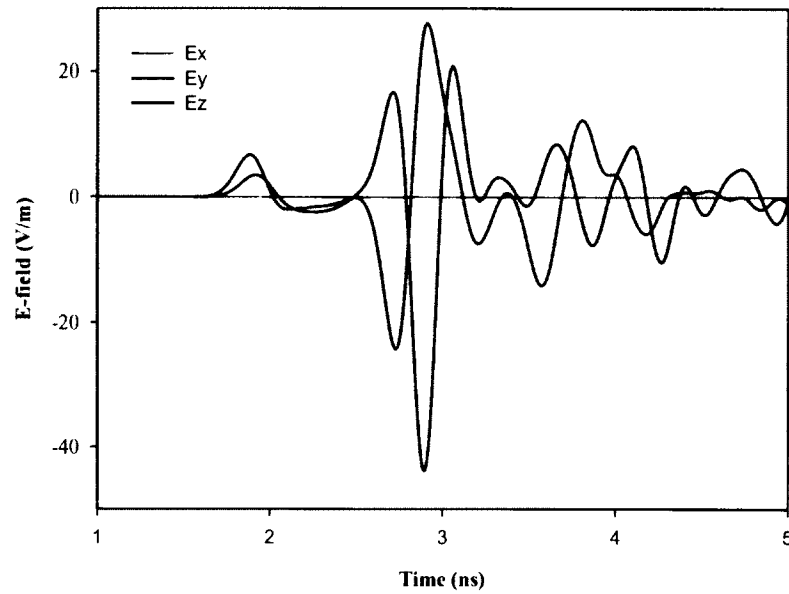
Fig. 6.14. The x-, y- and z- components of the electric field at focal point inside the biological tissue target.

Fig. 6.15 shows the electric field distribution when the first focal point is excited with a Gaussian pulse input. The figure shows field distribution at different instants of time.
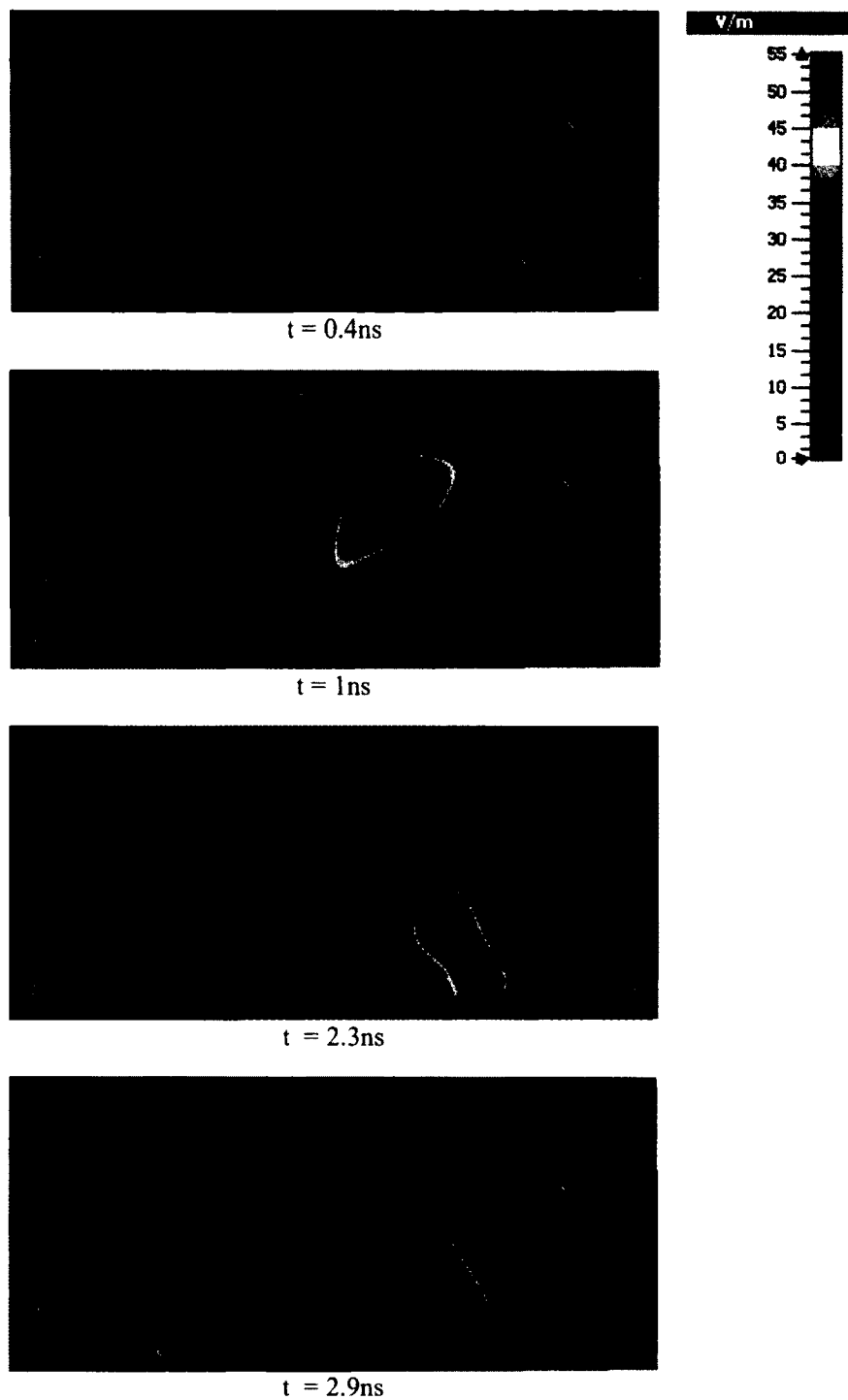
Fig. 6.15. The propagation of electromagnetic waves from the antenna to a biological target at different instants of time, with cut-plane of x = 0. The biological target has a relative permittivity of 9 and a conductivity of 0, and the plot uses a clamp to range 0 to 55V/m.

At the instant when the field reaches a maximum value at t = 2.9ns inside the hemispherical tissue, different cut plane views can be obtained (Fig. 6.16). Cut plane of x = 0 gives a side view, that of y = 0 gives a top view and the cut plane of z = 46.1cm gives a back view at the focal point.
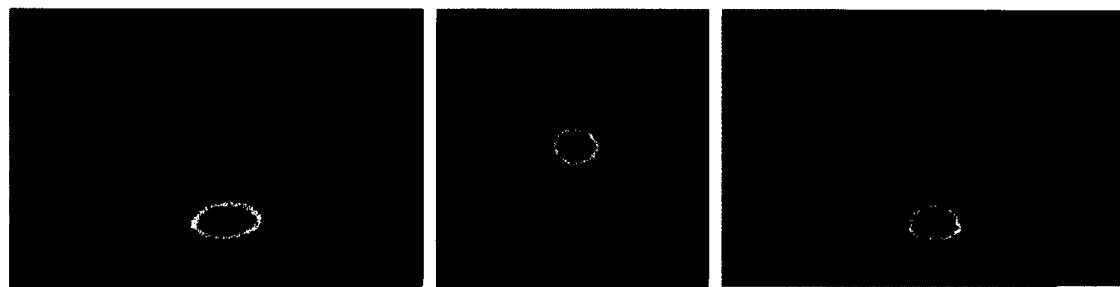
Cutting plane, x = 0 Cutting plane, y = 0 Cutting plane, z = 46.1cm

Fig. 6.16. Focusing of EM waves inside a biological target of relative permittivity 9 and conductivity 0, at t = 2.9ns, three different cut-plane views that show the focusing of electromagnetic energy in x-plane, y-plane and the focal plane along z-axis. The plot uses a clamp of 0 to 55V/m.

Fig. 6.17 shows a comparison of two antennas in terms of field distribution. Fig. 6.17a shows the electric field distribution along the z-axis for the antenna with a small aperture. Fig. 6.17b shows the electric field distribution along the z-axis for the antenna with a large aperture. The field values are normalized to the electric field at the air-tissue interface. While the absolute field is greater, the focal width becomes sharper, suggesting an improvement of the focusing characteristic.
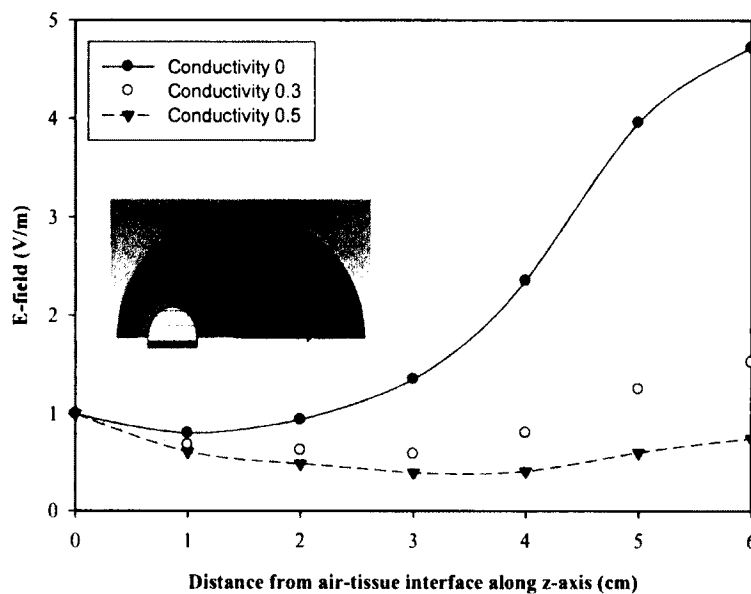
(a)
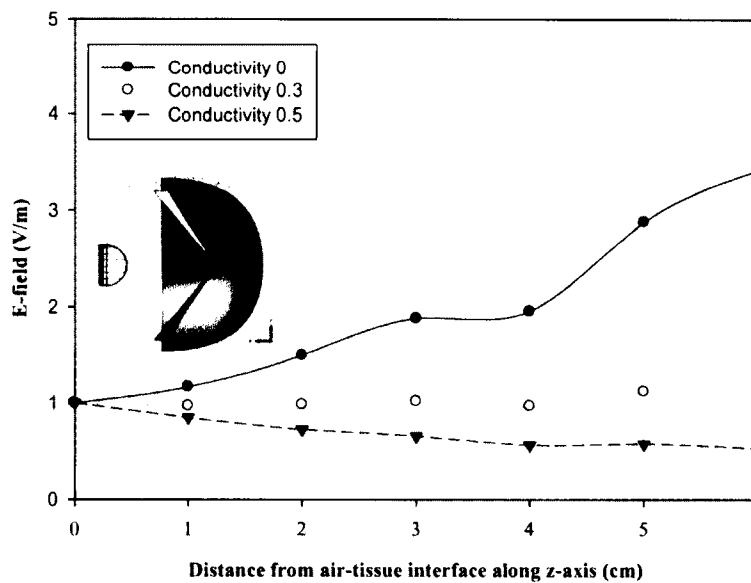
(b)

Fig. 6.17. The electric field distribution along the z-axis for (a) the antenna with aperture parallel to the line joining the two focal points, and for (b) the antenna with aperture perpendicular to the line joining the two focal points. z = 0 gives the air-tissue interface, and the field is normalized to the value at the air-tissue interface.

CHAPTER VII

SIMULATION STUDY OF FOCUSING ELECTROMAGNETIC FIELDS IN A HUMAN

HEAD MODEL

The previous chapter studied the delivery of sub-nanosecond pulses to a homogeneous hemispherical biological tissue target. This chapter extends to a realistic human head model. These cases will be looked at, using antenna alone, using the combination of the antenna and the dielectric lens, as well as the combination of the antenna and the lossy lens.

VII.I SIMULATION SETUP

VII.I.I HUGO Human Body Model

The CST STUDIO SUITE allows the use of more complex heterogeneous biological models by importing arbitrary Voxel data sets. These data sets define the body as a collection of small bricks each of which can be a different material. The anatomical data set of the HUGO model is provided by the Visible Human Project of the U.S. National Institutes of Health.

The HUGO model of the human body is a hypothetical adult human male who is 187.4cm tall, 37.4cm wide and 34.1cm deep. The HUGO data set has 32 tissue types, each with different material properties. The dielectric properties of the 32 distinct tissues are provided at seven different frequencies, ranging from 100MHz to 2,450MHz. The frequency-dependent dielectric properties for the tissues are available in the data sheet of the Federal Communication Commission [104].

The import is performed via an interface that allows different resolutions (1mm to 8mm) and gives the option of arbitrarily choosing whether to include or exclude any type of tissue in the simulation. For example, Fig. 7.1 shows the material "SkeletonMuscle" from the HUGO model of the adult male body with a 1mm resolution. In addition to the electromagnetic properties, such

as ε, μ and σ, there are thermal properties for the materials so that local heating may be modeled if desired. Thermal properties will not be considered here in this dissertation, but such a study could be conducted using Microwave Studio and the additional Thermal Solver in CST Studio Suites.
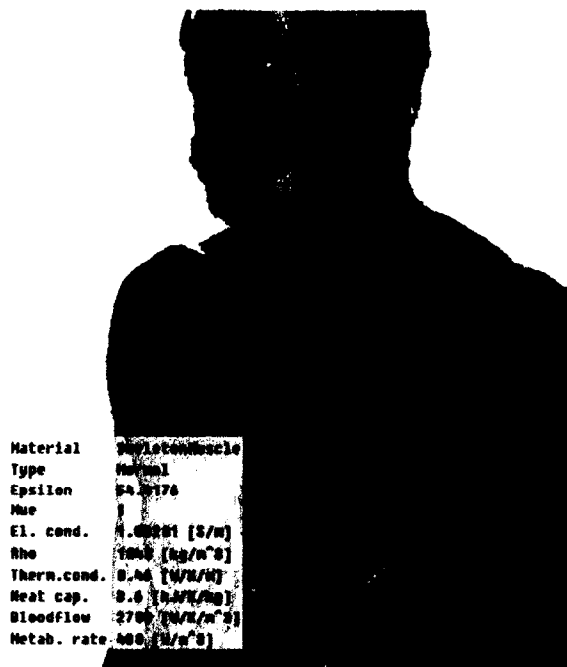
Fig. 7.1. Example of HUGO model.

VII.I.II Simulation Model

The dielectric constants and conductivities of the tissues used in this simulation study are given in Table 7.1. The data is valid for 1.8GHz. For lower frequency, the permittivity becomes larger and the conductivity is smaller. The opposite works for higher frequencies. In general, a Debye model for each tissue can be specified. Since CST Microwave Studio does not allow for the specification of the Debye model, a medium frequency 1.8GHz is therefore chosen.

Material Type	Relative permittivity (ε_r)	Conductivity (σ) S/m
Bone	11.78	0.28
Grey Matter	50	1.39
Fat Tissue	5.35	0.08
Nervous Opticus	30.87	0.84
White Matter	37	0.91
Skeleton Muscle	55.33	1.44

Table 7.1. The dielectric constants and conductivities of the tissues used in HUGO model [104].

The human head model is placed such that the human brain lies at the focal point of the antenna, and the top of the head coincides with the z-axis as shown in Fig. 7.2. The model has a grid size of 1mm × 1mm × 1mm.

Fig. 7.2. Cut-plane view of reflector antenna with human head model.

VII.II SIMULATION RESULTS

VII.II.I Field Measurements

The Gaussian pulse of 200ps rise time is fed to the first focal point of the impulse radiating antenna, and consequently delivered to the human brain model. The electric field along the z-axis from the air-head interface to the second focus of the reflector is measured by inserting

probes at every 1cm. The electric pulse at the focal point in the brain (6cm deep from the top of the head) is shown in Fig. 7.3. Again, the y-component dominates the overall field and the x and z components are negligible.
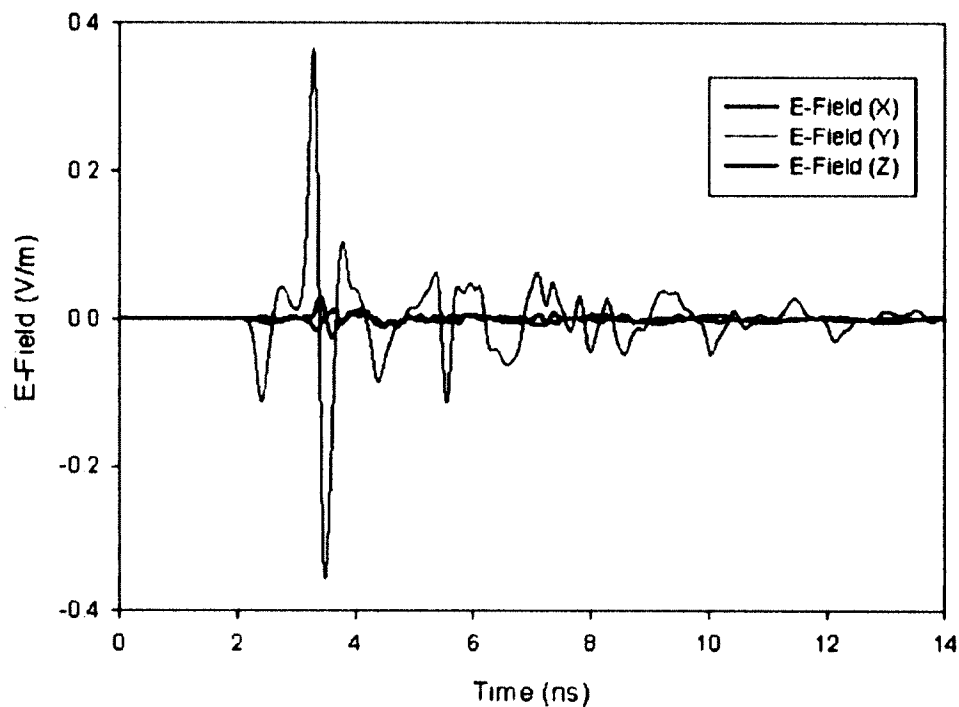
Fig. 7.3. Electric field at focus: the y-component of field is dominant among the electric fields in all directions.

Fig. 7.4 further shows the propagation of waves into the human head at different instants of time. The plot indicates that despite a slight asymmetry of the human head, the wave converges inside the brain tissue at 3.7ns at a distance 7-8cm from air-head interface. However, the overall intensity decreases from the surface as the wave penetrates, due to a strong loss of the tissue.
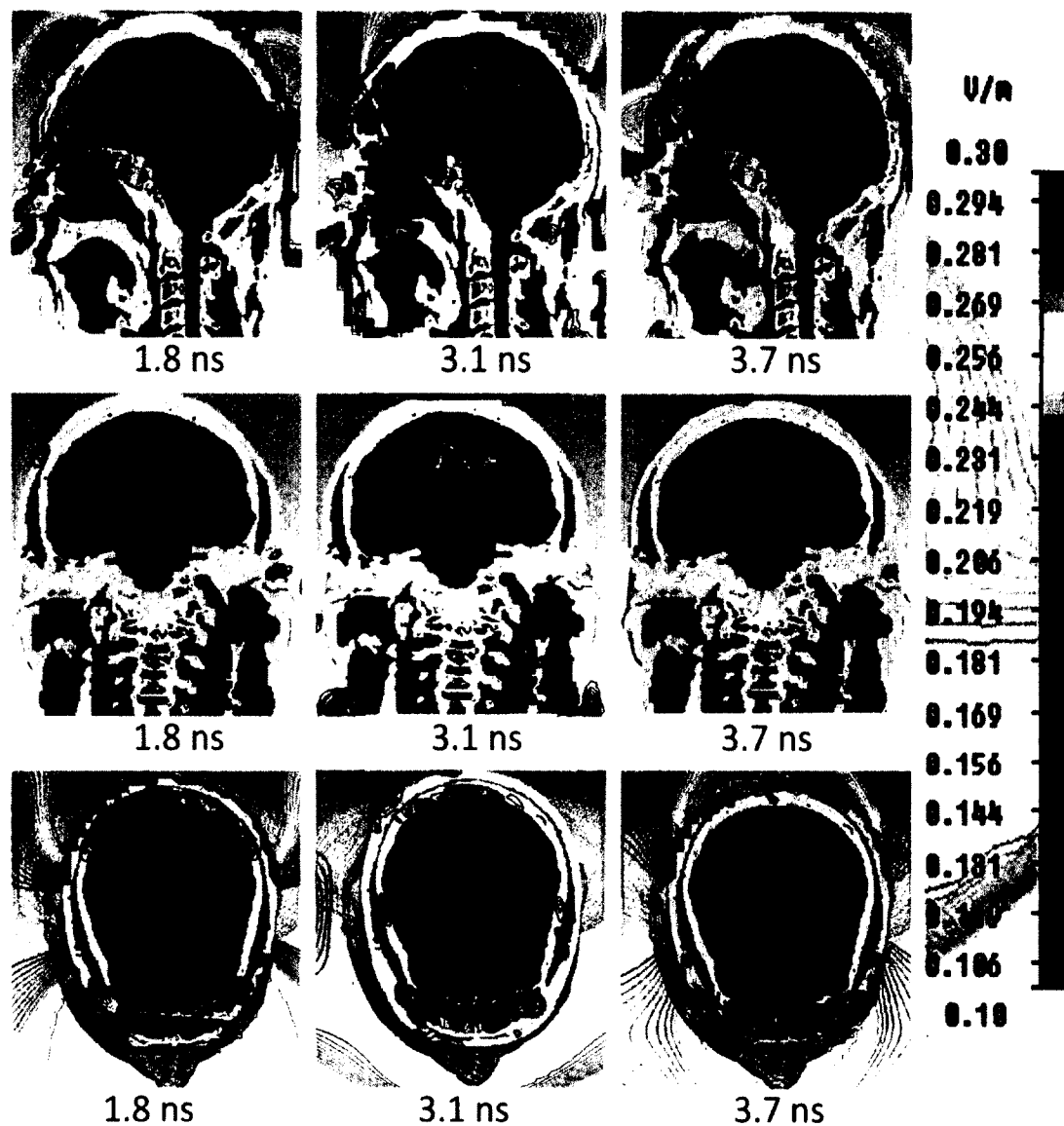
Fig. 7.4. The isoline plots of electric field distribution in the human brain exposed to a reflector antenna at various times, a clamp is used to range of 0.1 to 0.3V/m. The figure shows cross sections along the x-axis (side view), y-axis (back view) and z-axis (top view).

The probes placed inside the brain tissue measure the actual peak amplitudes of the field at different locations inside the human head model. Fig. 7.5 shows the electric field distribution along various radii from the air-head interface. Fields along all radial distances decrease significantly as the penetration depth increases.
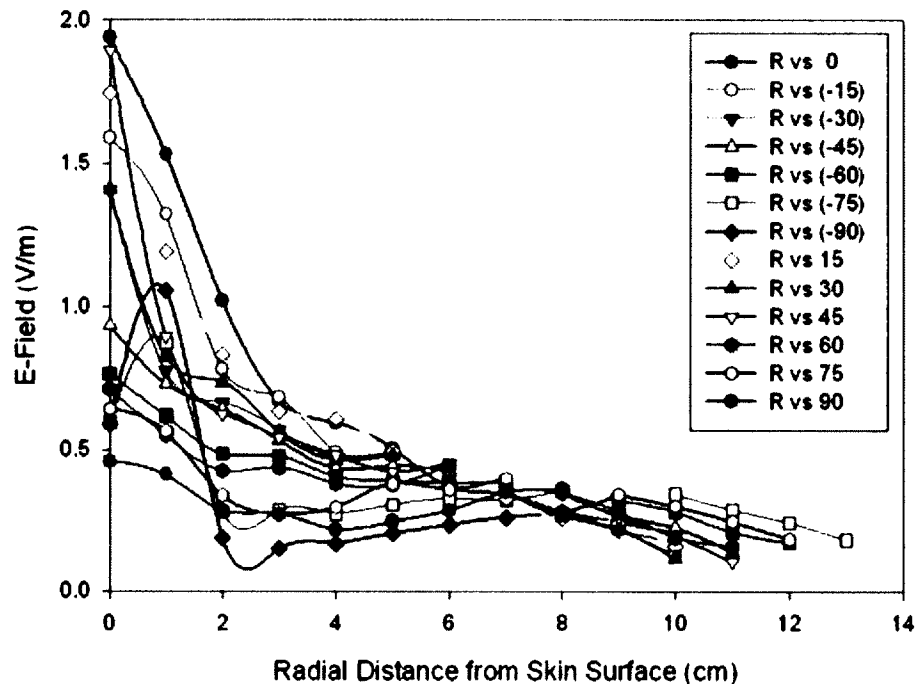
Fig. 7.5 Electric field distribution in the brain model along different radial distances.

VII.II.II Measurement of Focal Spot Size

In order to evaluate the focal spot size, at the time focusing occurs, that is at t = 3.7ns, different cross-sections of the x-, y- and z-planes are examined from the antenna focal plane. The resulting plots are shown in Fig. 7.6, from which the focal volume can be estimated as 1cm × 2cm × 1cm. The volume is narrow in x- and z-directions but wider in x-direction.
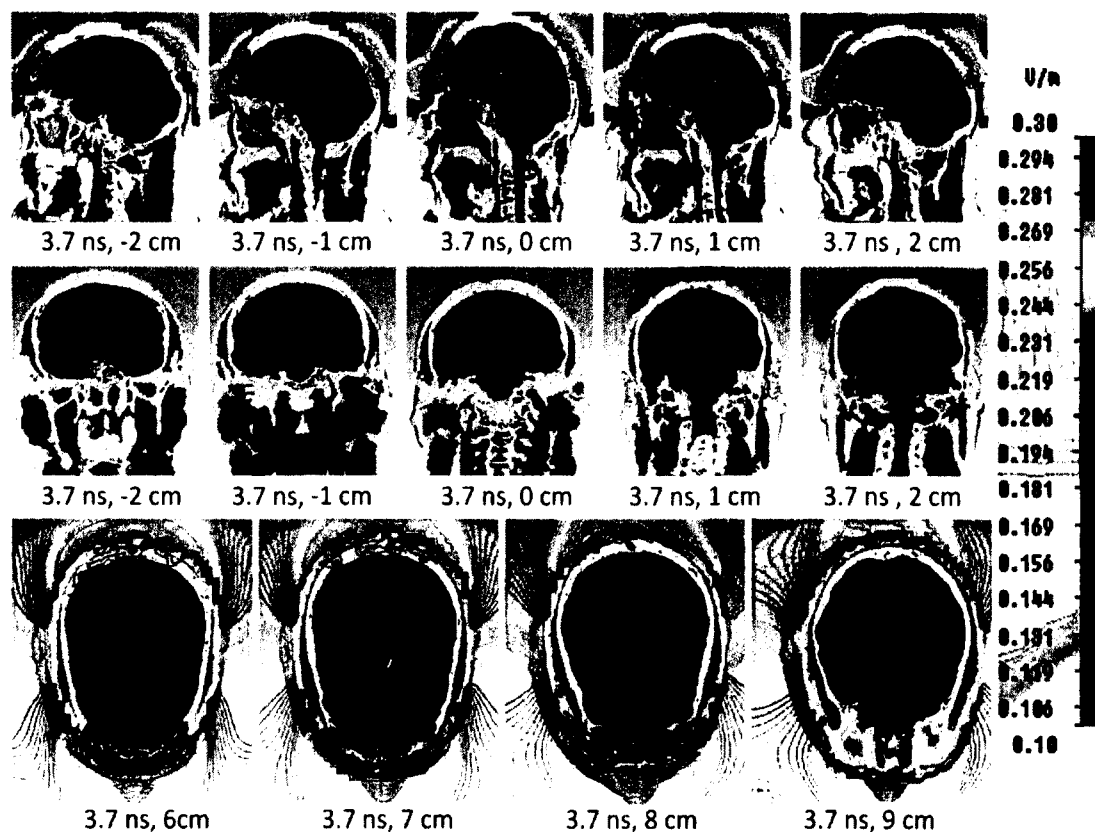
Fig. 7.6 Cross sections showing electric field distribution in the human brain at 3.7 ns along the x-axis (side view), y-axis (back view) and z-axis (top view). The sliced views were taken from x = -2 to 2cm, y = -2 to 2cm and z = 6 to 9cm at a step of 1cm.

VII.II.III Effect of Adding a Dielectric Lens

A non-lossy lens is used in conjunction with the antenna in order to increase the coupling from the antenna to the human head target. The resulting field distribution in isoline plot is as shown in Fig. 7.7. At 3.7ns, the impulse becomes constricted in size, but it reaches 8cm deep at 3.9ns where it is focused. Hence, the addition of the lens creates a delay compared with the case without a lens. The electric field at the focal point is increased with the use of the lens by a factor of about 1.6.
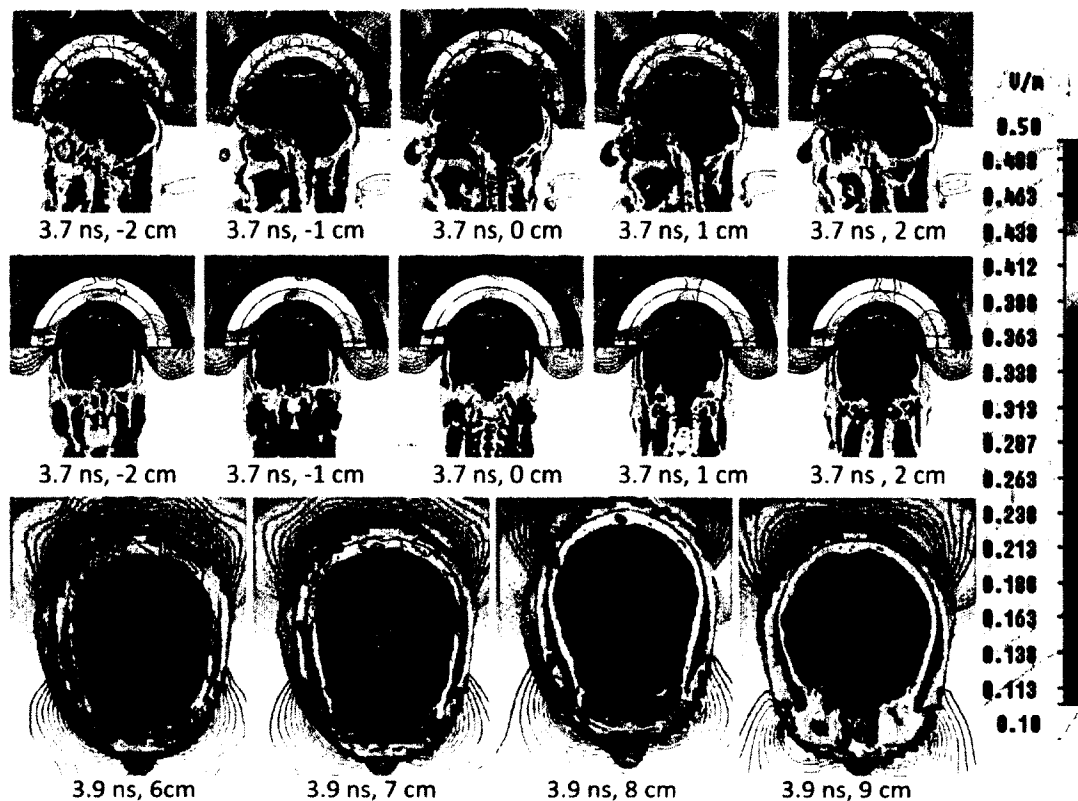
Fig. 7.7. The electric field distribution in the human brain with a dielectric lens at 3.7ns along the x-axis (side view), y-axis (back view) and at 3.9ns along the z-axis (top view). The sliced views were taken from x = -2 to 2cm, y = -2 to 2cm and z = 6 to 9cm at a step of 1cm. The plot uses a clamp to range of 0.1 to 0.5V/m.

The amplitudes of the field measured along different radial distances from the lens-skin interface are shown in Fig. 7.8. The field distribution is similar to the case where there is no lens added, except the amplitude at the skin is slightly higher due to the higher transmission of the lens. The field values converge to 0.5V/m at the depth of 8cm, also higher than the case without lens. Still, the highest field is on the axis and the fields on both sides are lower. So, the overall trend is decreasing as the impulse penetrates.
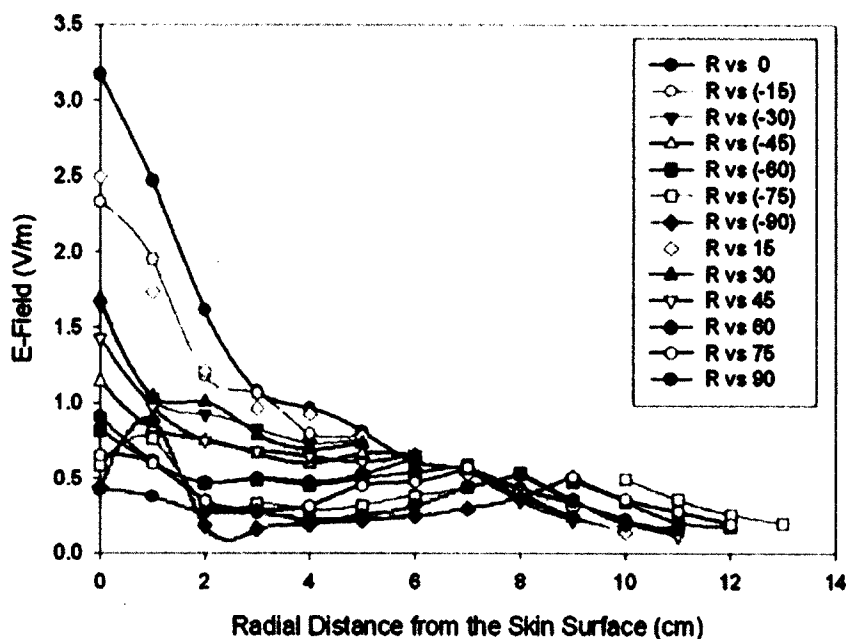
Fig. 7.8. The electric field distribution in the brain model with the non-lossy lens, along different radial distances.

Further the effect of adding the lens on the focal spot size was explored by examining the sliced views in the x-, y-, and z-directions. Fig. 7.7 shows that the region contains the maximum clamped value (0.5V/m) is approximately 1cm in the x-direction, -1 to 1cm in the y-direction and 1cm in the z-direction. The volume of the region is close to the case where no lens is used. Hence, the addition of the lens increases the coupling of the EM radiations to the tissue, but the reduction in the focal spot size is found not be significant.

VII.II.IV Effect of Adding a Lossy Dielectric Lens

In Chapter VI, the idea of a lossy lens coupling to the hemispherical tissue model was introduced and it was pointed out that with the use of the lossy lens, field distribution in the target tissue can be modified. The same concept is used for the human head model, where the reflector antenna is used with the lens where the field on the axis is attenuated by assigning conductivities to the 4th and 5th layer of the lens at angles ±45°. The resulting field distribution in an isoline plot is as shown in Fig. 7.9. The field distribution with a lossy lens is obviously different than the

non-lossy lens case, as the fields in the z-axis are largely damped and the off-axis fields become

higher. As shown in Fig. 7.9, the impulse is confined at 8cm from the top of the skull at t = 3.9ns.

Moreover, the shape of the electric field distribution is also different in case of lossy antenna.
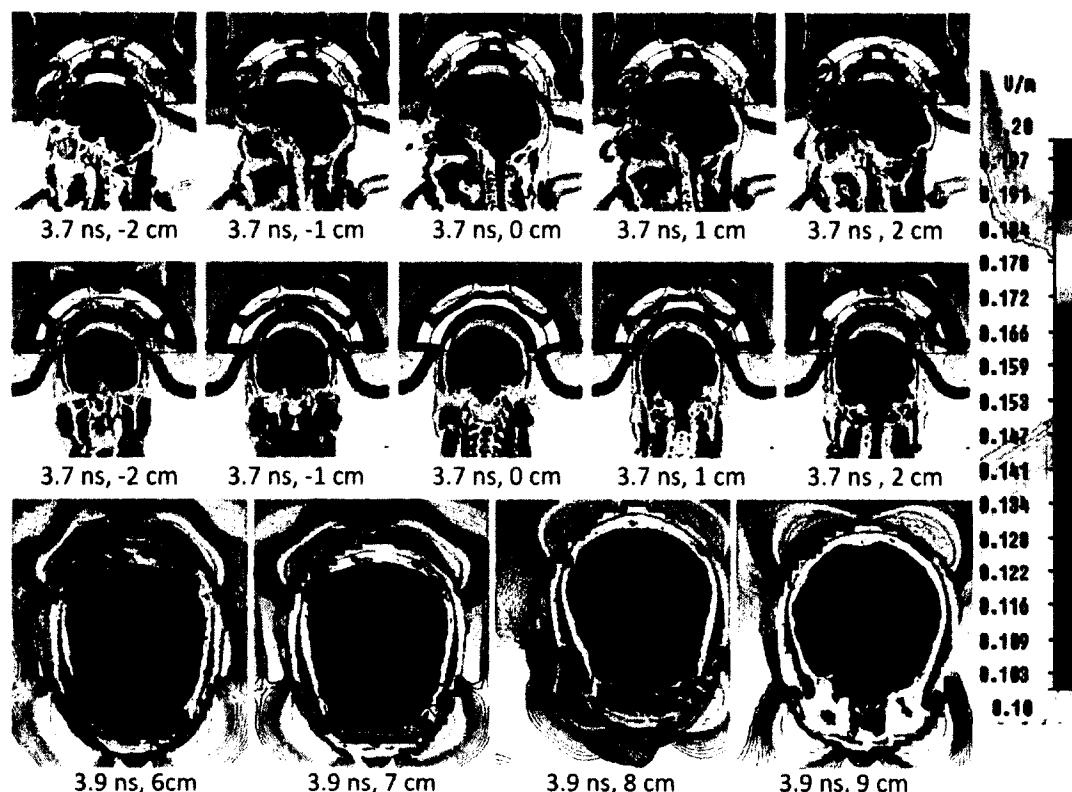
Fig 7.9. The electric field distribution in the human brain with the reflector antenna and lossy dielectric lens at 3.7ns along the x-axis (side view), y-axis (back view), and at 3.9ns along the z-axis (top view).The sliced views were taken from x = -2 to 2cm, y = -2 to 2cm, and z = 6 to 9cm in a step of 1cm. The plot uses a clamp to range of 0.1 to 0.2V/m.

The focal spot volume in this case can be again estimated from different sliced views. From Fig. 7.9, it is apparent that the focal spot size becomes smaller. The side view indicates the focal dimension is less than 1cm in the x-direction, as it is in the z-direction. The y-direction focal dimension is not as obvious as in the other two directions, but can still be seen becoming smaller. Such reduction in the focal spot size suggests that its location is more sensitive to the relative position between the antenna and the human head.

The amplitudes of the field measured along different radial distances from the lens-skin interface are shown in Fig. 7.10. Field measurement along the z-axis (0°) shows that the field becomes the lowest among all the radial directions and is slightly increased at z = 8cm. Hence, the lens provides strong attenuation along small angles and allows the fields entering at larger angles to pass. Thus, the field distribution in the brain is modified. Despite the strong attenuation, the field intensity near the focal point (8cm in depth) is 0.2V/m, which is reduced from that in the case of the non-lossy lens.
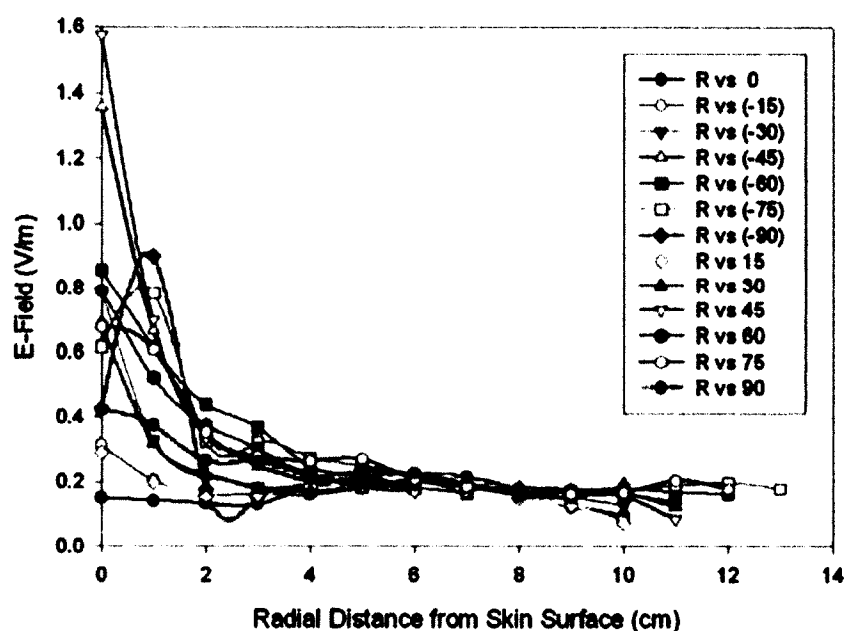
Fig. 7.10. The electric field distribution in the brain model with the lossy lens, along different radial distances.

On one hand, the lossy lens allows shrinking of the focal spot size, but on the other hand, with a lossy lens, the focal spot location becomes sensitive to the relative position of the antenna to human head. Meanwhile, the overall field intensity is decreased due to the extra attenuation introduced in the lens.

CHAPTER VIII

DISCUSSIONS

VIII.I. ANTENNA CHARACTERISTICS IN FREE SPACE

The electric field at the second focal point comprises three components: the prepulse, the impulse, and the postpulse. The prepulse is radiated directly from the conical transmission line and is proportional to the amplitude of the feed pulse. The impulse is the electromagnetic pulse reflected from the prolate-spheroidal reflector. Only the impulse will be focused at the second focal point coherently as the reflected wave on the surface will arrive at the second focal point in the same phase. The impulse part is proportional to the time derivative of the feed pulse: A faster rise-time pulse produces a higher amplitude. It is clear that in order to produce a large field at the focal point, a large voltage-time derivative and a low launching impedance of the conical transmission line are required. The pulse rise time should be short in order to increase the amplitude of the impulse. The impulse and the prepulse have opposite signs, with the impulse being much larger than the prepulse (Fig. 3.7). The ratio of the impulse to the prepulse is given by T/a, in which T satisfies $T = 2[a-z_0]/ct_\delta$. This ratio needs to be large for a large impulse. A "fat" and shallow antenna should produce a larger impulse amplitude at the focus.

From the perspective of electric field distribution, the prepulse decreases in the z-direction, with a $1/z$ dependence. For an observation point at 16cm, the geometric focus, the prepulse stays approximately constant along the y-axis (to 12cm), indicating again that it scales as $1/z$. The power density of the impulse, which is proportional to the square of the electric field, is focused in both lateral and axial directions. The distribution of power density has a full-width at half-maximum (FWHM) width of 32cm in the axial direction and a FWHM width of 10cm in the lateral direction (at 16cm).

The modeled distributions of the impulse in the axial direction and the lateral direction agree very well with the experimental results. This is true especially near the focal point in both the axial and the lateral electric field distributions. At an observing distance closer to the reflector edge, a slight discrepancy between the modeled field and measured field is observed, which can be due to the fact that the sensor may pick up other electric field components besides the x-directed field while the model only gives the x-directed field.

The maximum of the impulse electric field on the axis is also shifted slightly from the geometric focus (16cm) toward the reflector, which is observed in both the measured result and the modeled result. This is because the impulse decreases inversely with the distance while it is focused in space. Even though there is a coherent combination of waves at the focal point, the impulse electric field is still smaller than the nearby locations toward the reflector due to a large impulse width ct_δ (in spatial units). For the maximum impulse amplitude to occur at the geometric focus, the impulse width needs to be small compared to both $2z_0$ and $2b$. A similar discussion in the frequency domain has been presented in [105]. A pulse with faster rise time should allow the shift of the focal spot towards the geometric focus.

VIII.II. ANTENNA IN CONJUNCTION WITH LENS

When the focusing antenna is used for the delivery of short pulses into targets in the near field, a focusing dielectric lens near the second focal point allows minimization of the spot size and increase of the impulse amplitude. The antenna-lens combination is also used as an imaging system, which is designed to work in the case when a target is embedded in a medium that has the same dielectric constant as the innermost layer [91]. Therefore, this imaging system requires knowledge of the medium dielectric property when designing such a lens. A simpler case where a metallic target is placed in free space and in front of the lens allows the demonstration of the reduction of the focal spot size and improvement of the imaging resolution. It has been observed that the lens significantly increases the difference of the scattered signal (Fig.4.4). The maximum

difference (peak to peak) for the case with the lens is 0.95, approximately three times greater than without the lens (0.3). The target is moved along the lateral axis and the region is scanned laterally. The maximum differences for the cases with and without the lens are plotted in Fig. 4.5. For the case without the lens, the maximum differences beyond the lateral distances of 6cm are in actuality the same as the noise level, which makes it hard to detect the target. For the case with the lens, the detectable range is approximately the same. When the baseline is chosen as 0.15, the full width at half-maximum (FWHM) for the case with the lens is approximately 4cm, whereas the FWHM is approximately 6cm without the lens. Since the FWHM of the scattering difference determines the image resolution, the resolution is therefore increased by a factor of 1.5. It is noticed that although the focal spot size is reduced by a factor of 3, the resolution, i.e., the FWHM of maximum difference, is not increased accordingly by the same factor. This result suggests that the focal spot size is not the only factor that determines the imaging resolution, as the receiving characteristics of the antenna with or without the lens also contributes to the difference in the received signals.

To further verify the imaging resolution of the lens-antenna system, two targets of equal dimensions are imaged with different spacing between them. Again, the two objects are shifted from one edge of the lens to the other, which is equivalent to laterally scanning the two objects with the antenna-with-lens system. The background signals are subtracted from the signals obtained at each target location. The value of the difference is used to construct a 2-D image by assigning pixel values according to the magnitude of the signals received. Fig. 5.7 shows the image constructed with two objects with a spacing of 3.5cm and 5.5cm respectively. The two targets are irresolvable in the lateral direction when the spacing is shorter than 3.5cm. However, the imaging system is able to distinguish targets for a spacing of 5.5cm, so the resolution can be estimated as about 4cm. Although a confocal scanning in the lateral direction has been successfully demonstrated, longitudinal scanning is beneficial to probe a more deeply buried

target. A confocal detection of a target when the target is placed along the longitudinal axis of the lens is therefore, demonstrated. Fig. 4.6 shows the maximum differences of the signals in the cases with and without the lens. At the focal point longitudinal distance, the difference is greatest and is about three times higher than without the lens. Until the target is moved 2cm away from the focus, still, a higher difference is obtained than without the lens. Beyond 2cm, the difference decreases faster with the lens than without, as the field exponentially decays in space. Because the focus is fixed along the longitudinal axis in the current system, the confocal configuration can only detect targets near the focus, which means close to the lens. For deeper targets, different lenses with different foci will have to be employed.

The design of the prolate spheroidal antenna with the focusing lens presented above is conceptually complete and good for delivery of a target on the surface, e.g., skin tumor. The system can deliver 200ps pulses with a spot area of approximately 2cm, which is adequate for biological applications. However, there remain two major technological challenges before a prototype device can be field-tested [106]. The first concerns the dielectric materials used in the focusing lens. The dispersion loss involved in the lens, i.e., the amplitude of the impulse is reduced and the beam-width increased after the wave passage, poses a challenge to the lens material selection. It is also observed that the lens filters frequencies above 5GHz [106]. Therefore, materials with less losses and a better frequency response, from 0 to 10GHz, must be explored. The second challenge is to provide high voltage and ultrafast impulse. Previous design by Baum et al. [107] has included a switching unit at the first focal point. Megavolt switching voltage was tested using transformer oil as switching medium. For the switch designs considered, current technology limits the repetition rate to a few hundred hertz. Higher frequencies, of the order of a few kilohertz, are required to induce apoptosis in cells. Hence, techniques to increase the frequency of switch discharges must be investigated.

VIII.III. DELIVERY OF SUBNANOSECOND PULSES TO TISSUES

The transmission of sub-nanosecond pulses to a homogeneous tissue is studied using an impulse antenna. A spherical wave with a propagation vector perpendicular to a hemispherical target converges on the geometric center of the spherical wave. This offers a rather simple prediction of the field distribution in the target. The conductivity of the tissue, however, changes the geometric-optics picture. It creates a decreasing electric field with increasing penetration distance. But increasing the tissue dielectric constant, meaning applying the method to a different tissue, can reverse the trend and allows for a deep focusing (e.g., 6cm in depth). For the generation of large field intensities in the shallow region of the tissue, a single antenna is sufficient. As the antenna radiation is an inhomogeneous spherical wave, the highest field is along the axis, which means the highest field distribution in the target also coincides with the axis. For deeper focusing, the loss due to the conductivity of the dielectric can be alleviated by applying this method to tissue with high dielectric constants, such as muscle tissue.

A second approach that could possibly create deep focusing is to use a dielectric lens in conjunction with the antenna. The lens can modify the electric field distribution in the tissue. In one case, the lens is loss-free and the electric fields along the axis are the highest. In the other case, the lens is assigned with lossy material to attenuate the axial incident electric fields, but allowing the incident fields from the sides to pass. This case results in the opposite distribution as the first case: the largest fields on the side, and the small fields along the axis. A local maximum near the geometric focus exists in this case.

In a target which contains composite tissues, such as the brain, the multiple layers in the propagation path (skin and skull) do not pose a significant change to the waveforms of the converging waves: the field along the axis is still strongest and the spherical wave still converges near the geometric focus. In Figure 7.3, both prepulse and impulse can be clearly identified for the case when a human head is directly exposed to the reflector antenna. However, the overall

intensity decreases from the surface as the wave penetrates, due to a strong resistive loss of the tissue. In addition, the converging point in the brain can be clearly identified to be 8cm deep from the top of the human head, which is 2cm deeper than the geometric focus of the reflector antenna (Fig. 7.4). The volume is 1cm × 2cm × 1cm in the xyz-directions and is situated in the white-matter region. As white matter has a dielectric constant of 37, the spatial width of such pulse is 1cm, which is consistent with the simulation result for an input pulse of 200ps.

It is therefore reasonable to predict the focal spot size simply by estimating the pulse spatial width in the dielectric where the focal point is to be created. On the other hand, the amplitude of the electric field decreases from the human head surface to the converging point along the radial paths of small azimuthal angles, with the field on the z-axis being the strongest among all the radial paths.

Adding a dielectric lens in addition to the reflector antenna does not change the converging point and still allows the radiation to converge at 8cm in depth. It increases the coupling of radiation to the tissue and the electric field intensity at the converging point. Similar to the case without the lens, the electric field also decreases along the paths of small azimuthal angles and it is still the strongest on the z-axis.

Using a dielectric lens with the two innermost layers being partially lossy does not change the location of the converging point and still allows the radiation to converge at 8cm in depth. The field on the z-axis in this case, however, becomes the lowest because of the attenuation in the lens, leaving the fields higher along other radial paths with wider angles.

The electric field distributions obtained in a hemispherical tissue (Fig. 6.11 and 6.12) and a brain model (Figs. 7.8 and 7.10) show two extreme cases of electric field distribution. One has the highest field on the z-axis while the fields on the side are smaller. The other case is that high fields penetrate from the two sides about the z-axis, while leaving the axial field small, but in the

deep region, a local maximum can be formed. The first case can be used for delivering sub-nanosecond pulses to the shallow regions along the axis, and the second case can be used for delivering sub-nanosecond pulses to the shallow region on the sides. The targeted region can be selected by placing lossy materials in the corresponding incident angles of the lens, which offers one way of varying the focal zone by utilizing different lenses. On the other hand, the two entirely opposite cases suggest that it may be possible to find a specific lens case where the pulse amplitude in deep region has a local maxima even though the fields on the sides are higher, but the side regions may be controlled to be as shallow as skin or bone area, and they are not physiologically as sensitive as brain tissue. The lens design need be optimized and could consist of a number of lossy elements in the same layer of the lens with each layer having different values of conductivities. A typical multi-variable optimization method, such as a Genetic Algorithm [108], can be used to find the optimum values of the lens segments.

It is noticed that in Figures 7.4, 7.7, and 7.9 that the electric field scattering on the head surface remains large. To reduce the impact of such scattering to the clinical environment, the reflector can be increased in the reflection area and extended to an elliptical cavity with the opening aperture at the patient's neck. Microwave absorbers can be placed in the cavity to absorb the scattering. In addition, the face of the patient can be protected by wearing a resistive mask to damp the surface waves. In terms of the choice of delivery, the reflector antenna has the ability of steering the converging point just by shifting the antenna position. Adding a dielectric lens can improve the coupling of the radiation (for non-lossy lens) or modify the electric field distribution in the tissue (for lossy lens), but is only useful for a fixed converging point. Furthermore, the lens design and construction is patient-specific and cannot be used for other patients.

What is the implication of this study? As shown in Fig. 7.5, for a voltage of 1V fed to the antenna, an electric field is in the range of 1.5V/m at a depth of 2cm, which is the motor cortex region in the brain. This means an input voltage of 33.3kV may be sufficient for an effective

stimulation to meet the stimulation threshold of 50kV/m as mentioned in [109]. For deep stimulation, Fig. 7.9 indicates that there is a locally confined region at a depth of 8cm. For a 1V pulse input, the field intensity is found to be 0.2–0.5V/m for the three cases, which suggests that pulses of 250kV–2.5MV need to be fed into the antenna in order to meet the estimated stimulation threshold of 50kV/m. Such a high-amplitude pulse generator becomes technically challenging (if not impossible) even though a 1MV pulse generator has been built [110].

CHAPTER IX

SUMMARY

The prolate spheroidal antenna with a reflector diameter of 0.5m focuses the sub-nanosecond electric pulse radiation near the second focal point (16cm from the aperture plane). The focus spot has an ellipsoidal shape, and the distribution of power density has a small diameter in the lateral direction and a wide dimension in the axial direction (10cm and 32cm in FWHM). The measured electric field distribution agrees with the modeled results to a large extent. Near the focal point, the measured electric field is exactly as the model predicts.

Near-field target detection has been explored with a focusing prolate spheroidal antenna using a confocal technique. As the antenna is designed to focus in free space, the use of such a system is limited to the detection of targets in free space or otherwise embedded in a weakly scattering medium. When linear targets are placed at the focal position, the antenna is sensitive to their orientation. A focusing antenna in conjunction with a dielectric lens has been shown to have a resolution of approximately 4cm. The resolution can be further improved by increasing the dielectric constant of the material in the innermost layer of the lens. The present confocal system prevents a scanning of depth as the target needs to be placed close to the lens (within 2cm of the focus) in order to show a stronger signal return compared to without the lens. Scanning of depth may be possible if the probed object is detected with a lens of a different design.

A numerical study of the delivery of sub-nanosecond pulsed radiation to biological tissues has been performed for bioelectric applications. The antenna fed by 200ps pulses uses an elliptical reflector in conjunction with a dielectric lens. Two numerical targets are studied: one is a hemispherical tissue with a resistivity of 0.3–1S/m and a relative permittivity of 9–70 and the other is a realistic human head model (HUGO). The electromagnetic simulation shows that despite the tissue heterogeneity of the human head, the electric field converges to a spot 8cm in

depth, and the spot volume is approximately 1cm × 2cm × 1cm in both cases when using only the reflector and a lens as an addition. Rather than increasing as it approaches the converging point, the electric field decreases strongly with distance from the skin to the converging point due to tissue resistive loss. The electric field distribution, however, can be reversed by making the dielectric lens lossy with the two innermost layers being partially resistive. The lossy lens causes an attenuation of the electric field near the axis, but the electric field generated by the waves, which pass the lens at wider angles, compensate for this loss. A local maximum electric field in a deeper region of the tissue may form with the lossy lens. The study shows that it is possible to generate the desired electric field distribution in the complex biological target by modifying the dielectric properties of the lens used in conjunction with the reflector antenna.

REFERENCES

1. C. E. Baum. "Focal Waveform of a Prolate-Spheroidal IRA", Note 509, *Sensor and Simulation Notes*, Feb. 2006.

2. J. C. Lin. "Frequency Optimization for Microwave Imaging of Biological Tissues", *in Proceedings of the IEEE*, vol. 73, no. 2, pp.374-375, Feb. 1985.

3. A. W. Guy, J. F. Lehmann, J. B. Stonebridge, C. C. Sorensen. "Development of a 915-MHz Direct-Contact Applicator for Therapeutic Heating of Tissues," *Microwave Theory and Techniques, IEEE Transactions on*, vol. 26, no. 8, pp. 550-556, Aug. 1978.

4. M. A. Stuchly, S. S. Stuchly, G. Kantor. "Diathermy Applicators with Circular Aperture and Corrugated Flange," *Microwave Theory and Techniques, IEEE Transactions on*, vol. 28, no. 3, pp. 267-271, Mar. 1980.

5. F. Sterzer. "Ridge-Waveguide Applicator for Treatment with Electromagnetic Energy." US Patent number: 4282887, 1981.

6. K. S. Nikita and N. K. Uzunoglu. "Analysis of the Power Coupling from a Waveguide Hyperthermia Applicator into a Three-Layered Tissue Model," *Microwave Theory and Techniques, IEEE Transactions on*, vol. 37, no. 11, pp. 1794-1801, Nov. 1989.

7. Y. Nikawa and F. Okada. "Dielectric-Loaded Lens Applicator for Microwave Hyperthermia," *Microwave Theory and Techniques, IEEE Transactions on*, vol. 39, no. 7, pp. 1178-1178, Jul. 1991.

8. T. Samaras, P. J. M. Rietveld, G. C. van Rhoon. "Effectiveness of FDTD in Predicting SAR Distributions from the Lucite Cone Applicator," *Microwave Theory and Techniques, IEEE Transactions on*, vol. 48, no. 11, pp. 2059-2063, Nov. 2000.

9. R. C. Gupta and S. P. Singh. "Analysis of the SAR Distributions in Three-Layered Bio-Media in Direct Contact with a Water-loaded Modified Box-horn Applicator," *Microwave Theory and Techniques, IEEE Transactions on*, vol. 53, no. 9, pp. 2665-2671, Sept. 2005.

10. L. Beyne and D. De Zutter. "Power Deposition of a Microstrip Applicator Radiating into a Layered Biological Structure," *Microwave Theory and Techniques, IEEE Transactions on*, vol. 36, no. 1, pp. 126-131, Jan. 1988.

11. F. Montecchia. "Microstrip-Antenna Design for Hyperthermia Treatment of Superficial Tumors," *Biomedical Engineering, IEEE Transactions on*, vol. 39, no. 6, pp. 580-588, June 1992.

12. S. Curto, P. McEvoy, X. Bao, M. J. Ammann. "Compact Patch Antenna for Electromagnetic Interaction with Human Tissue at 434MHz," *Antennas and Propagation, IEEE Transactions on*, vol. 57, no. 9, pp. 2564-2571, Sept. 2009.

13. S. Curto et al. "Interaction of RF-Hyperthermia Applicator with High Fidelity Human Body Model," *IEEE Antennas and Propagation Society International Symposium*, San Diego, California, 5-11 July 2008.

14. J. J. W. Lagendijk. "A New Coaxial TEM Radiofrequency/Microwave Applicator for Non-Invasive Deep-Body Hyperthermia," *Journal of Microwave Power*, vol. 18, no. 4, pp. 367-375, 1983.

15. P. Raskmark and J. B. Andersen. "Focused Electromagnetic Heating of Muscle Tissue (Short Papers)," *Microwave Theory and Techniques, IEEE Transactions on*, vol. 32, no. 8, pp. 887-888, Aug. 1984.

16. W. H. Harrison and F. K. Storm. "Loosely Coupled Coaxial TEM Applicators for Deep Heating," *Intl. J. Hyperthermia*, vol. 5, no. 3, pp. 297-306, 1989.

17. H. P. Schwan and G. M. Piersol. "The Absorption of Electromagnetic Energy in Body Tissues," *American Journal of Phys. Med.*, vol. 33, pp. 370-404, Dec. 1954.

18. J. F. Lehman et al. "Comparison of Relative Heating Patterns Produced in Tissues by Exposure to Microwave Energy at Frequencies of 2450 and 900 Megacycles," *Arch. Phys. Med. Rehab.*, vol. 43, pp. 69-76, Feb. 1962.

19. A. W. Guy. "Electromagnetic Fields and Relative Heating Patterns Due to a Rectangular Aperture Source in Direct Contact with Bilayered Biological Tissue," *Microwave Theory and Techniques, IEEE Transactions on*, vol. 16, no. 2, pp. 214-223, Feb. 1971.

20. K. Hirasawa, K. Fujimoto, T. Uchikura, S. Hirafuku, H. Naito. "Power Focusing Characteristics of Ellipsoidal Reflector," *Antennas and Propagation, IEEE Transactions on*, vol. 32, no. 10, pp. 1033-1039, Oct. 1984.

21. G. C. Trichopoulos, I. S. Karanasiou, N. K. Uzunoglu. "Enhancing the Focusing Properties of an Ellipsoidal Beamformer based Imaging System: A Simulation Study", *Proceedings of the 28th IEEE EMBS Annual International Conference*, New York City, USA, Aug 30-Sept 3, 2006.

22. I. S. Karanasiou, K. T. Karathanasis, A. Garetsos, N. K. Uzunoglu. "Development and Laboratory Testing of a Noninvasive Intracranial Focused Hyperthermia System," *Microwave Theory and Techniques, IEEE Transactions on*, vol. 56, no. 9, pp. 2160-2171, Sept. 2008.

23. I. A. Gouzouasis, K. T. Karathanasis, I. S. Karanasiou, N. K. Uzunoglu. "Contactless Passive Diagnosis for Brain Intracranial Applications: A Study using Dielectric Matching Materials," *Bioelectromagnetics*, vol. 31, no. 5, pp. 335–349, July 2010.

24. C. C. Johnson and A. W. Guy. "Nonionizing Electromagnetic Wave Effects in Biological Materials and Systems," *Proceedings of the IEEE*, vol. 60, no. 6, pp. 692-718, June 1972.

25. J. C. Lin and P. Bernadi. "Computational Methods for Predicting Field Intensity and Temperature Change" in *Handbook of Biological Effects of Electromagnetic Fields*, 3rd Edition, CRC Press, New York, 2007.

26. D. A. Sanchez-Hernandez. *High Frequency Electromagnetic Dosimetry*. Artech House, Norwood, MA, 2009.

27. M. V. Prior, M. L. D. Lumori, J. W. Hand, G. Lamaitre, C. J. Schneider, J. D. P. van Dijk. "The Use of a Current Sheet Applicator Array for Superficial Hyperthermia: Incoherent

versus Coherent Operation," *Biomedical Engineering, IEEE Transactions on*, vol. 42, no. 7, pp. 694-698, July 1995.

28. E. R. Lee, T. R. Wilsey, P. Tarczy-Hornoch, D. S. Kapp, P. Fessenden, A. W. Lohrbach, S. D. Prinoas. "Body Conformable 915 MHz Microstrip Array Applicators for Large Surface Area Hyperthermia," *IEEE Trans. Biomed. Eng.*, vol. 39, no. 5, pp. 470-483, 1992.

29. P. R. Stauffer et al. "Conformal Microwave Array (CMA) Applicators for Hyperthermia of Diffuse Chest Wall Recurrence," *Intl. J. Hyperthermia*, vol. 26, no. 7, pp. 686-698, October 2010.

30. P. F. Turner. "Regional Hyperthermia with an Annular Phased Array," *IEEE Trans. on Biomedical Engg.*, vol. BME-31, no. 1, pp. 106-114, Jan. 1984.

31. F. A. Gibbs, M. D. Sapozink, K. S. Gates, J. R. Stewart. "Regional Hyperthermia with an Annular Phased Array in the Experimental Treatment of Cancer: Report of Work in Progress with Technical Emphasis", *IEEE Trans. on Biomedical Engg.*, vol. BME-31, no. 1, pp. 115-119, Jan. 1984.

32. F. Jouvie, J. C. Bolomey, G. Gaboriaud. "Discussion of Capabilities of Microwave Phased Arrays for Hyperthermia Treatment of Neck Tumors," *Microwave Theory and Techniques, IEEE Transactions on*, vol. 34, no. 5, pp. 495-501, May 1986.

33. A. J. Fenn, V. Sathiaseelan, G. A. King, P. R. Stauffer. "Improved Localization of Energy Deposition in Adaptive Phase-Array Hyperthermia Treatment of Cancer," *Lincoln Lab. J.*, vol. 9, no. 2, pp. 187–195, 1996.

34. R. A. Gardner, H. I. Vargas, J. B. Block, C. L. Vogel, A. J. Fenn, G. V. Kuehl, and M. Doval. "Focused Microwave Phased Array Thermotherapy for Primary Breast Cancer," *Annals of Surgical Oncology*, vol. 9, no. 4, pp. 326-332, 2002.

35. D. Fatehi, J. Van Der Zee and G. C. Van Rhoon. "Intra-Patient Comparison between Two Annular Phased Array Applicators, Sigma-60 and Sigma-Eye: Applied RF Powers and

Intraluminally Measured Temperatures," *Int. J. Hyperthermia*, vol. 27, no. 3, pp. 214-223, May 2011.

36. P. Wust, B. Hildebrandt, G. Sreenivasa, B. Rau, J. Gellermann, H. Riess, R. Felix and P. M. Schlag. "Hyperthermia in Combined Treatment of Cancer," *THE LANCET Oncology*, vol. 3, pp. 487-497, August 2002.

37. X. Yong, L. Yinghua, Z. Hongxin, W. Yeqiu. "An Overview of Ultra-Wideband Technique Application for Medial Engineering," *Complex Medical Engineering, IEEE/ICME International Conference on*, pp. 408-411, 23-27 May 2007.

38. M. Converse, E. J. Bond, B. D. Van Veen, S. C. Hagness. "A Computational Study of Ultra-Wideband versus Narrowband Microwave Hyperthermia for Breast Cancer Treatment," *Microwave Theory and Techniques, IEEE Transactions on*, vol. 54, no. 5, pp. 2169-2180, May 2006.

39. S. C. Hagness, A. Taflove, J. E. Bridges. "Two-Dimensional FDTD Analysis of a Pulsed Microwave Confocal System for Breast Cancer Detection: Fixed-Focus and Antenna-Array Sensors," *Biomedical Engineering, IEEE Transactions on*, vol. 45, no. 12, pp. 1470-1479, Dec. 1998.

40. X. Li, S. C. Hagness. "A Confocal Microwave Imaging Algorithm for Breast Cancer Detection," *Microwave and Wireless Components Letters, IEEE*, vol. 11, no. 3, pp. 130-132, March 2001.

41. E. J. Bond, X. Li, S. C. Hagness, B. D. Van Veen. "Microwave Imaging via Space-Time Beamforming for Early Detection of Breast Cancer," *Antennas and Propagation, IEEE Transactions on*, vol. 51, no. 8, pp. 1690-1705, Aug. 2003.

42. S. K. Davis et al. "Microwave Imaging via Space-Time Beamforming for Early Detection of Breast Cancer: Beamformer Design in the Frequency Domain," *Journal of Electromagnetic Waves and Applications*, vol. 17, no. 2, pp. 357-381, 2003.

43. X. Li, S. K. Davis, S. C. Hagness, D. W. van der Weide, B. D. Van Veen. "Microwave Imaging via Space-Time Beamforming: Experimental Investigation of Tumor Detection in Multilayer Breast Phantoms," *Microwave Theory and Techniques, IEEE Transactions on*, vol. 52, no. 8, pp. 1856-1865, Aug. 2004.

44. M. Converse et al. "Ultrawide-Band Microwave Space-Time Beamforming for Hyperthermia Treatment of Breast Cancer: A Computational Feasibility Study," *Microwave Theory and Techniques, IEEE Transactions on*, vol. 52, no. 8, pp. 1876-1889, Aug. 2004.

45. X. Li, S. C. Hagness, M. K. Choi, D. W. van der Weide. "Numerical and Experimental Investigation of an Ultrawideband Ridged Pyramidal Horn Antenna with Curved Launching Plane for Pulse Radiation," *Antennas and Wireless Propagation Letters, IEEE*, vol. 2, no. 1, pp. 259-262, 2003.

46. H. B. Lim, N. T. T. Nhung, E. P. Li, N. D. Thang. "Confocal Microwave Imaging for Breast Cancer Detection: Delay-Multiply-and-Sum Image Reconstruction Algorithm," *Biomedical Engineering, IEEE Transactions on*, vol. 55, no. 6, pp. 1697-1704, June 2008.

47. M. Klemm, I. J. Craddock, J. A. Leendertz, A. Preece, and R. Benjamin. "Improved Delay-and-Sum Beamforming Algorithm for Breast Cancer Detection," *Int. J. Antennas Propag.*, vol. 2008, pp. 1–9, 2008.

48. A. Shahzad, M. O'Halloran, E. Jones, M. Glavin. "Prefiltered Beamforming for Early-Stage Breast Cancer Detection," *Antennas and Wireless Propagation Letters, IEEE*, vol. 12, pp. 500-503, 2013.

49. M. Fink. "Time Reversal of Ultrasonic Fields I: Basic Principles," *Ultrasonics, Ferroelectrics and Frequency Control, IEEE Transactions on*, vol. 39, no. 5, pp. 555-566, Sept. 1992.

50. P. Kosmas, C. M. Rappaport. "Time Reversal with the FDTD Method for Microwave Breast Cancer Detection," *Microwave Theory and Techniques, IEEE Transactions on*, vol. 53, no. 7, pp. 2317-2323, July 2005.

51. B. Guo, L. Xu, J. Li. "Time Reversal Based Microwave Hyperthermia Treatment of Breast Cancer," *Signals, Systems and Computers, Conference Record of the Thirty-Ninth Asilomar Conference on*, pp. 290-293, Oct. 28 2005-Nov. 1 2005.

52. H. D. Trefna, J. Vrba, and M. Persson. "Evaluation of a Patch Antenna Applicator for Time Reversal Hyperthemia," *Int. J. Hyperthermia*, vol. 26, no. 2, pp. 185–197, March 2010.

53. H. D. Trefna, P. Togni, R. Shiee, J. Vrba, and M. Persson. "Design of a Wideband Multi-Channel System for Time Reversal Hyperthermia," *Int. J. Hyperthermia*, vol. 28, no. 2, pp. 175–183, March 2012.

54. H. Schantz. *The Art and Science of Ultrawideband Antennas*, Artech House, London, 2005.

55. S. Silver. *Microwave Antenna Theory and Design*, IEE Electromagnetic Waves Series 19, London, 1984.

56. R. K. Amineh, A. Trehan, and N. K. Nikolova. "TEM Horn Antenna for Ultra-Wide Band Microwave Breast Imaging," *Progress in Electromagnetics Research B*, vol. 13, pp. 59-74, 2009.

57. D. Abed and H. Kimouche. "Design and Characterization of Microstrip UWB Antennas," in *Ultra Wideband*, Boris Lembrikov (Ed.), InTech, 2010.

58. X. Chen, J. Liang, S. Wang, Z. Wang, C. Parini. "Small Ultra-Wideband Antennas for Medical Imaging," *Antennas and Propagation Conference*, Loughborough, pp. 28-31, 17-18 March 2008.

59. R. Nilavalan, I. J. Craddock, A. Preece, J. Leendertz, R. Benjamin. "Wideband Microstrip Patch Antenna Design for Breast Cancer Tumour Detection," *Microwaves, Antennas & Propagation, IET*, vol. 1, no. 2, pp. 277-281, April 2007.

60. C. E. Baum. "Radiation of Impulse-like Transient Fields," Note 321, *Sensor and Simulation Notes*, 1989.

61. C. E. Baum and E. G. Farr. "Impulse Radiating Antennas" in *Ultra-wideband/short pulse electromagnetics*, H. L. Bertoni et al (Eds.), Plenum Press, NY, 1993.

62. E. G. Far. "Analysis of the Impulse Radiating Antenna," Note 329, *Sensor and Simulation Notes*, 1991.

63. E. G. Farr and C. E. Baum. "The Radiation Pattern of Reflector Impulse Radiating Antennas: Early-Time Response," Note 358, *Sensor and Simulation Notes*, June 1993.

64. E. G. Farr and C. E. Baum. "Radiation from Self-Reciprocal Apertures," Note 357, *Sensor and Simulation Notes*, 1993.

65. A. Teggatz, A. Jostingmeier, T. Meyer, A. S. Omar. "Detection of Buried Objects such as Landmines using a Forward Impulse Radiating Antenna (IRA)," *Antennas and Propagation Society International Symposium, 2005 IEEE*, vol. 2A, pp. 627-630, 3-8 July 2005.

66. D.V. Giri. *High-Power Electromagnetic Radiators: Nonlethal Weapons and Other Applications*, Cambridge, MA: Harvard University Press, 2004.

67. C. E. Baum. "From the Electromagnetic Pulse to High-Power Electromagnetics," *Proceedings of the IEEE*, vol. 80, no. 6, pp. 789-817, 1992.

68. Y. Manteghi and Y. Rahmat-Samii. "On the Characterization of a Reflector Impulse Radiating Antenna (IRA): Full-Wave Analysis and Measured Results," *IEEE Trans. Ant. Propag.*, vol. 54, pp. 812-822, Mar. 2006.

69. C. Polk. "Biological Applications of Large Electric Fields: Some History and Fundamentals," *IEEE Transactions on Plasma Science*, vol. 28, no. 1, pp. 6-14, Feb. 2000.

70. R. P. Joshi and K. H. Schoenbach. "Bioelectric Effects of Intense Ultrashort Pulses," *Critical Reviews in Biomedical Engineering*, vol. 38, no. 3, pp. 255-304, 2010.

71. K. H. Schoenbach, S. Xiao, R. P. Joshi, J. T. Camp, T. Heeren, J. F. Kolb, S. J. Beebe. "The Effect of Intense Subnanosecond Electrical Pulses on Biological Cells," *Plasma Science, IEEE Transactions on*, vol. 36, no. 2, pp. 414-422, April 2008.

72. C. E. Baum, E. G. Farr, and D. V. Giri. "Review of impulse-radiating antennas" in *Review of Radio Science 1996–1999*, W. R. Stone, Ed. Oxford, U.K.: Oxford Univ. Press, 1999, Ch. 16, pp. 403–439.

73. R. C. Hansen. "Focal Region Characteristics of Focused Array Antenna," *IEEE Trans. Antennas Propag.*, vol. AP-33, no. 12, pp. 1328–1337, Dec. 1985.

74. M. G. M. Hussain. "Ultra-Wideband Impulse Radar - An Overview of the Principles," *Aerospace and Electronic Systems Magazine, IEEE*, vol. 13, no. 9, pp. 9-14, Sep. 1998.

75. J. D. Kraus. *Antennas*, 2nd Edition, McGraw-Hill, 1988.

76. C. A. Balanis. *Antenna Theory Analysis and Design*, 3rd Edition, John Wiley & Sons, 2005.

77. C. E. Baum. "Focused Aperture Antennas," Note 306, *Sensor and Simulation Notes*, 1987.

78. W. R. Smythe. *Static and Dynamic Electricity*, 2nd edition, McGraw-Hill, 1950.

79. C. E. Baum. "Prolate Spheroidal Scatterer for Spherical TEM Waves," Note 508, *Sensor and Simulation Notes*, January 2006.

80. S. Altunc and C. E. Baum. "Extension of the Analytic Results for the Focal Waveform of a Two-arm Prolate-Spheroidal Impulse Radiating Antenna," Note 518, *Sensor and Simulation Notes*, Nov. 2006.

81. S. Xiao, S. Altunc, P. Kumar, C. E. Baum and K. H. Schoenbach. "A Reflector Antenna for Focusing Subnanosecond Pulses in the Near Field," *IEEE Antennas and Propagation Letters*, vol. 9, pp. 12-15, 2010.

82. J. E. Thompson and L. H. Luessen. "Fast Electrical and Optical Measurements", Leiden, The Netherlands: Martinus Nijhoff, vol. I, p. 73, 1986.

83. Internet: http://www.cst.com

84. M. Clemens and T. Weiland. "Discrete Electromagnetism with the Finite Integration Technique," *Progress in Electromagnetics Research*, vol. 32, pp. 65–87, 2001.

85. B. Krietenstein, P. Thoma, R. Schuhmann, T. Weiland. "The Perfect Boundary Approximation Technique Facing the Big Challenge of High Precision Computation," *Proceedings of the 19th LINAC Conference*, Chicago, August 1998.

86. C. C. Chang and S. K. Jeng. "A Multilevel Subgridding Scheme for Two-Dimensional Finite-Difference Time-Domain Method," *Antennas and Propagation Society International Symposium, 2001. IEEE*, vol. 1, pp. 36-39, 8-13 July 2001.

87. C. E. Baum. "Addition of Lens before the Second Focus of a Prolate-Spheroidal IRA," Note 512, *Sensor and Simulation Notes*, April 2006.

88. C. E. Baum, J. J. Sadler and A. P. Stone. "A Uniform Dielectric Lens for Launching a Spherical Wave into a Paraboidal Reflector," Note 360, *Sensor and Simulation Notes*, July 1993.

89. S. Altunc, C. E. Baum, C. G. Christodoulou, and E. Schamiloglu. "Analytical Calculations of a Lens for Better Focusing the Fields from a Prolate-Spheroidal Reflector," *Antennas and Propagation Society International Symposium, 2008. IEEE*, pp.1-4, 5-11 July 2008.

90. C. E. Baum and J. M. Lehr. "Tapered Transmission-Line Transformers for Fast High-Voltage Transients," *IEEE Trans. Plasma Sci.*, vol. 30, pp. 1712-1721, 2002.

91. S. Altunc, C. E. Baum, C. J. Buchenauer, C. G. Christodoulou, and E. Schamiloglu. "Design of a Special Dielectric Lens for Concentrating a Subnanosecond Electromagnetic Pulse on a Biological Target," *IEEE Transactions on Dielectrics and Electrical Insulation*, vol. 16, no. 5, pp.1364-1375, October 2009.

92. S. Altunc, C. E. Baum, C. G. Christodoulou, and E. Schamiloglu. "Lens Design for a Prolate-Spheroidal Impulse radiating Antenna (IRA)," Note 525, *Sensor and Simulation Notes*, November 2007.

93. L. Peters Jr., J. J. Daniels, and J. D. Young. "Ground Penetrating Radar as a Subsurface Environmental Sensing Tool," *Proceedings of the IEEE*, vol. 82, no. 12, pp.1802-1822, 1994.

94. S. C. Hagness, A. Taflove, and J. E. Bridges. "Two-Dimensional FDTD Analysis of a Pulsed Microwave Confocal System for Breast Cancer Detection: Fixed-Focus and Antenna-Array Sensors," *IEEE Trans. Biomed. Eng.*, vol. 45, no. 2, pp.1470-1479, 1998.

95. A. O. Boryssenko, E. Boryssenko, V. Ivashchuk, A. Lishchenko, and V. Prokhorenko. "UWB Subsurface Radar with Antenna Array for Imaging of Internal Structure of Concrete Structural Elements," in *Ultra-Wideband Short pulse Electromagnetics 5*, Kluwer Academic/Plenum Publisher, pp. 199-206, 2002.

96. M. Dehmollaian, M. Thiel, and K. Sarabandi. "Through-the-Wall Imaging using Differential SAR," *IEEE Transactions on Geoscience and Remote Sensing*, vol. 47, no. 5, pp. 1289-1296, 2009.

97. X. Li, E. J. Bond, B. D. Van Veen, and S. C. Hagness. "An Overview of Ultrawideband Microwave Imaging via Space-Time Beamforming for Early-Stage Breast Cancer Detection," *IEEE Antennas Propagat. Mag.*, vol. 47, no. 2, pp. 19-34, 2005.

98. S. Xiao, C. Bajracharya, C. E. Baum, K. H. Schoenbach. "Imaging with Focused Pulsed Electromagnetic Radiation," *Pulsed Power Conference, 2009. IEEE*, pp. 872-875, June 28 2009-July 2 2009.

99. C. Bajracharya, S. Xiao, C. E. Baum, and K. H. Schoenbach, "Target Detection with Impulse Radiating Antenna," *IEEE Antennas and Wireless Propagation Letters*, vol. 10, pp. 496-499, 2011.

100. S. Nag and M. Barnes. "A Moving Target Detection Filter for an Ultra-Wideband Radar," *IEEE Radar Conference*, pp. 147-153, 2003.

101. D. J. Daniels. *Ground Penetrating Radar*, 2nd Edition, IEE, 2004.

102. M. Lazebnik, D. Popovic, L. McCartney, C. B. Watkins, M. J. Lindstrom, J. Harter, S. Sewall, T. Ogilvie, A. Magliocco, A. T. M. Breslin, W. Temple, D. Mew, J. H. Booske, M. Okoniewski, S. C. Hagness. "A Large-Scale Study of Ultrawideband Microwave Dielectric Properties of Normal, Benign and Malignant Breast Tissues Obtained from Cancer Surgeries," *Phys Med Biol*, vol. 52, pp. 6093–6115, 2007.

103. K. Hirasawa, K. Fujimoto, T. Uchikura, S. Hirafuku, H. Naito. "Power Focusing Characteristics of Ellipsoidal Reflector," *Antennas and Propagation, IEEE Transactions on*, vol. 32, no. 10, pp. 1033-1039, Oct. 1984.

104. Internet: www.fcc.gov/fcc-bin/dielec.sh-09/2002

105. J. W. Sherman, III, "Properties of Focused Apertures in the Fresnel Region," *IRE Trans. Antennas Propag.*, vol. AP-10, no. 4, pp. 399–408, Jul. 1962.

106. P. Kumar, C. E. Baum, S. Altunc, J. Buchenauer, S. Xiao, C. G. Christodoulou, E. Schamiloglu, K. H. Schoenbach. "A Hyperband Antenna to Launch and Focus Fast High-Voltage Pulses onto Biological Targets," *Microwave Theory and Techniques, IEEE Transactions on*, vol. 59, no. 4, pp. 1090-1101, April 2011.

107. C. E. Baum, W. L. Baker, W. D. Prather, J. M. Lehr, J. P. O'Loughlin, D. V. Giri, I. D. Smith, R. Altes, J. Fockler, D. M. McLemore, M. D. Abdalla, M. C. Skipper. "JOLT: A Highly Directive, Very Intensive, Impulse-Like Radiator," *Proceedings of the IEEE*, vol. 92, no. 7, pp. 1096-1109, July 2004.

108. D. T. Pham and D. Karaboga. *Intelligent Optimization Techniques: Genetic Algorithms, Tabu Search, Simulated Annealing and Neural Networks*, London: Springer, 2000.

109. F. Guo, C. Yao, C. Bajracharya, S. Polisetty, K. H. Schoenbach, S. Xiao. "Simulation Study of Delivery of Subnanosecond Pulses to Biological Tissues with an Impulse Radiating Antenna," *Bioelectromagnetics*, vol. 35, no. 2, pp. 145-159, Feb. 2014.

110. W. D. Prather, C. E. Baum, R. J. Torres, F. Sabath, D. Nitsch. "Survey of Worldwide High-Power Wideband Capabilities," *Electromagnetic Compatibility, IEEE Transactions on*, vol. 46, no. 3, pp. 335-344, Aug. 2004.

PUBLICATIONS

- S. Xiao, C. Bajracharya, C. E. Baum, K. H. Schoenbach. "Imaging with Focused Pulsed Electromagnetic Radiation," *Pulsed Power Conference, 2009. IEEE,* pp. 872-875, June 28 2009-July 2 2009.

- J. F. Kolb, S. Xiao, J. T. Camp, M. Migliaccio, C. Bajracharya, K. H. Schoenbach. "Sub-Nanosecond Electrical Pulses for Medical Therapies and Imaging," *Proceedings of the Fourth European Conference on Antennas and Propagation (EuCAP),* Spain, April 2010.

- C. Bajracharya, S. Xiao, J. Li, K. H. Schoenbach. "Target Detection in the Near Field with Focused Pulsed Electromagnetic Radiation," *Power Modulator and High Voltage Conference (IPMHVC), 2010 IEEE International,* pp. 666-669, 23-27 May 2010.

- C. Bajracharya, S. Xiao, C. E. Baum, and K. H. Schoenbach, "Target Detection with Impulse Radiating Antenna," *IEEE Antennas and Wireless Propagation Letters,* vol. 10, pp. 496-499, 2011.

- F. Guo, C. Yao, C. Bajracharya, S. Polisetty, K. H. Schoenbach, S. Xiao. "Simulation Study of Delivery of Subnanosecond Pulses to Biological Tissues with an Impulse Radiating Antenna," *Bioelectromagnetics,* vol. 35, no. 2, pp. 145-159, Feb. 2014.

VITA

Chandra Bajracharya received her B.S. degree in Electrical Engineering from Tribhuvan University, Institute of Engineering, Nepal, in 2002, and her M.S. degree in Electrical Power Engineering from the Norwegian University of Science and Technology, Trondheim, Norway, in 2008. She also received her M.S. degree in Applied Computing from the Eastern Kentucky University, Richmond, Kentucky, in 2013.